Dynamics of High Redshift Disk Galaxies

Dynamics of High Redshift Disk Galaxies

Proefschrift

ter verkrijging van
de graad van Doctor aan de Universiteit Leiden,
op gezag van de Rector Magnificus prof. mr. P.F. van der Heijden,
volgens besluit van het College voor Promoties
te verdedigen op donderdag 4 december 2008
klokke 13:45 uur

door

Lottie van Starkenburg

geboren te Leiden
in 1978

Promotiecommissie

Promotores:	Prof. dr. M. Franx	
Co-promotor:	Dr. P. P. van der Werf	
Referent:	Dr. M. A. W. Verheijen	(Kapteijn Instituut, Groningen)
Overige leden:	Dr. N. M. Förster Schreiber	(Max-Planck-Institut für extraterrestrische Physik - Garching, Germany)
	Prof. dr. F. I. Israel	
	Prof. dr. G. Miley	
	Prof. dr. K. H. Kuijken	

Weet je wat ik zo raar vind? Gek hè?!
Ik heb zulke kleine ogen, maar ik kan zó véél zien!

Table of contents

Chapter 1

Introduction

1.1   Galaxy scaling relations

The rotation velocity of disk galaxies depends on the distance to the center of the galaxy. In the inner parts, the rotation velocity rises steeply with increasing radius, until a maximum rotation velocity is reached. At larger radii, the rotation velocity may show a decrease or remain constant. In the outskirts of disk galaxies, the rotation velocities remains constant until the farthest observed radii.

The rotation velocity of disk galaxies is determined by their total mass:

$$V(r)^2 = \alpha GM(r)/r \qquad (1.1)$$

where V is the rotation velocity at radius r, α is a constant of order unity, G is the gravitational constant and M is the mass within radius r. As V is constant in the outer parts, the total masses of disk galaxies should be proportional to r.

Disk galaxies obey fundamental scaling relations between size, rotation velocity and luminosity. The relation between the luminosity and rotation velocity of spiral galaxies is one of the tightest correlations in astronomy:

$$L \propto V^a \qquad (1.2)$$

where L is the luminosity, V is the maximum or flat rotation velocity and a is a number between 3 and 4, depending on observed wavelength and velocity measurement. It is better known as the Tully-Fisher relation (TFR) (Tully & Fisher 1977) and is the subject of this thesis. The TFR has been used to measure distances and the Hubble constant, but it is also an interesting relation to constrain galaxy formation and evolution scenarios (e.g. Courteau et al. 2007).

Similar scaling relations exist for elliptical galaxies. The Faber-Jackson relation relates luminosity and velocity dispersion. This relation has larger scatter than the TFR, but this can be improved using surface brightness as third parameter. The so-called Fundamental Plane of elliptical galaxies relates velocity dispersion, size and surface brightness.

The origin of the TFR is, more than 30 years after its discovery, still subject of debate. Some authors explain the TFR as a consequence of self-regulated star formation in disks with different masses (e.g. Silk 1997). In other models, the TFR is a direct consequence of the cosmological equivalence between mass and circular velocity resulting from the finite age of the universe which imposes a maximum radius from with matter can accrete to form a disk (e.g. Mo et al. 1998, Steinmetz & Navarro 1999). Recently,

Courteau et al. (2007) showed that two long-known, different theoretical predictions for two different slopes of the TFR are in fact related. The zero-point of the TFR constrains the starformation history and many authors struggle to reproduce it (e.g. Portinari & Sommer-Larsen 2007, Steinmetz & Navarro 1999). The slope of the TFR and the steepening of the slope towards longer wavelengths have several explanations. Some explain it by supernova feedback (van den Bosch 2000), others claim that it is a natural result of the hierarchical models (Steinmetz & Navarro 1999). The small scatter in the TFR is explained by scatter in halo spin parameters and formation redshifts (e.g. van den Bosch 2000). Today, no model for galaxy formation and evolution can simultaneously explain the zero-point, slope and scatter of the TFR and simultaneously the zero-point and shape of the luminosity function (Courteau et al. 2007 and references therein).

An alternative explanation for the TFR comes from Modified Newtonian Dynamics (MOND) (Milgrom 1983a, 1983b). According to MOND, the exact relation between total dynamical mass M and rotation velocity is

$$GMa_0 = V_\infty^4 \tag{1.3}$$

where G is the gravitational constant and a_0 is the critical acceleration of MOND, which only becomes relevant at low accelerations in the outskirts of galaxies. The slope of the TFR can be modified to values slightly different from 4 by variations in (total) mass-to-light-ratio. Scatter is introduced into the TFR only by observational errors and uncertainties in converting observed light into mass.

1.2 Properties of the Tully-Fisher relation at $z = 0$

Tully & Fisher (1977) used H I linewidths and photographic magnitudes to derive their famous relation between rotation velocity and luminosity. The TFR has subsequently been studied at optical and near-infrared wavelengths, and with different parameters on the velocity axis. The scatter in the TFR decreases and the slope of the TFR increases going from blue to near-infrared wavelengths (e.g. Verheijen 2001). This is explained by small differences in star formation rate (SFR) and/or extinction which are negligible at longer wavelengths. Offsets from the B and R band TFR correlate with SFR indicators such as $B - R$ or $B - I$ color, galaxy type, gas content and EW(Hα) (Verheijen 2001, Kannappan et al. 2002). Such correlations are absent using near-infrared luminosities (Verheijen 2001).

Rotation velocities can be measured more accurately using rotation curves (RCs) derived from slit or integral field spectroscopy in stead of integrated linewidths. Spiral galaxies have characteristic RCs, rising steeply in the center towards their maximum velocity, and then remain flat. The RCs of early type spirals may show a slight decrease in rotation velocity after they have reached their maximum velocity. For some (irregular, dwarf, low surface brightness) galaxies, the RC rises until the last observed point. Different measures of rotation velocity from the RCs of spiral galaxies have been used for TFR studies. Examples are the rotation velocity at a certain number of scale lengths, (e.g. Courteau 1997), the maximum rotation velocity observed and the rotation of the

flat part of the RC, V_{flat} (e.g Verheijen 2001). Verheijen (2001) finds the tightest correlation between the flat RC velocity and absolute K band magnitude. The observed scatter of this relation is consistent with zero intrinsic scatter.

The TFR of many different samples of spiral galaxies have been studied: cluster spirals, field spirals, starburst galaxies, S0 galaxies, LSB galaxies, spiral galaxies with AGN, polar ring galaxies, dwarf galaxies, interacting galaxies, late type spiral galaxies, barred galaxies, ... (e.g. Mendes de Oliviera et al. 2003; Barton et al. 2001; Van Driel, Van den Broek & Baan 1995; Brungardt 1998; Davoust & Contini 2004; Stil & Israel 1998; Courteau et al. 2003; Arnaboldi et al. 2003; Neistein et al. 1999; Matthews et al. 1998; Sprayberry et al. 1995; Verheijen 2001; Noordermeer & Verheijen 2007). All these samples find correlations between rotation velocity (or linewidth) and luminosity. The scatter and slope of these relation may differ (depending on sample, choice of parameters and procedures for correcting observed quantities such as extinction and turbulent motions), but there is little variation in the zero-point of the high mass end.

The optical and near-infrared emission from galaxies is produced by stars. The differences in slope and scatter of the optical and near-infrared TFRs originate thus in the wavelength dependent properties of the stellar population and dust of galaxies. A pass-band independent TFR can be obtained by modeling of the spectral energy distribution (SED) to obtain the stellar masses. Indeed, the tight correlation is preserved and this relation is refered to as the stellar mass TFR (McGauch et al. 2000, Bell & de Jong 2001). The stellar mass TFR relates stellar mass to total dynamical mass.

If the gas mass is added to the stellar mass, one obtains the baryonic mass TFR. Some authors claim that this resolves the apparent turnover towards smaller stellar masses in the stellar mass TFR for galaxies with $V \lesssim 90 \text{ km s}^{-1}$ (e.g. McGauch et al. 2000). Also, Noordermeer & Verheijen show that this may also resolve the curvature at the high mass end of the TFR introduced by galaxies with low gas fractions and a large discrepancy between the maximum and flat rotation curve velocity. This suggest that the TFR relates the baryonic and dark matter of disk galaxies.

1.3 The Tully-Fisher relation at high redshift

The zero-point, slope and scatter of the optical, near-infrared and stellar mass TFR are expected to evolve with redshift. The evolution of the TFR with redshift constrains the evolution of stellar populations and the build-up of stellar mass within galaxies of a certain total dynamical mass.

A number of TFR studies at different redshift have been published over the last decade, with contradicting results. While the first studies of the rest frame B band TFR in the redshift range $0.1 - 1.0$ showed no evolution (Vogt et al. 1996, 1997), most follow-up studies found $\sim 1 - 1.5$ mag brightening in rest frame B band from $z = 0$ to $z = 1$ (e.g. Barden et al. (2003) found ~ 1.1 mag brightening at $<z> \sim 0.9$, Nakamura et al. (2005) found 1.3 mag per unit redshift for galaxies with median redshift 0.39, Chiu et al. (2007) found 1.5 mag for [O II]λ3727 emitters at $z \sim 0.85$, Milvang-Jensen et al. (2003) found 1.6 mag per unit redshift).

However, Metevier et al. (2006) find that $z = 0.4$ cluster galaxies are *under*luminous with respect to the local B band TFR by 0.50 ± 0.23 mag. This result is even more puz-

zling as their galaxies have very bright emission lines, and local galaxies with similar $H\alpha$ EW are on average brighter than expected from the TFR (Kannappan et al. 2002). This result is also contradicted by other studies of cluster galaxies. Milvang-Jensen et al. (2003) find some evidence that cluster spirals are $0.5 - 1.0$ mag brighter than field galaxies. Bamford et al. (2005a, 2005b) also find that cluster spirals are brighter than field spirals for given rotation velocity (redshift range $0.25 - 1$, offset is 0.7 ± 0.2 mag). For field galaxies, they find an upper limit of 1.0 ± 0.5 mag brightening by $z \sim 1$.

While most studies focus on zero-point evolution, some authors also take into account evolution of the slope of the TFR. Böhm & Ziegler (2007) find differential luminosity evolution for a sample of 124 galaxies between $z = 0.1$ and $z = 1.0$. Massive galaxies are consistent with the local B band TFR, while on average the galaxies are 1.22 ± 0.40 mag per unit redshift brighter than expected from the local TFR. Although this is consistent with the luminosity of low mass galaxies being more sensitive to small amount of additional star formation, Kannappan & Barton (2004) discussed several pitfalls for measuring luminosity offsets from high redshift TFRs. They find that strong outliers are virtually always kinematically anomalous galaxies.

The number of studies of the rest-frame near-infrared TFR at high redshift is very limited. Conselice et al. (2005) analyzed 101 disk galaxies in the redshift range $0.2 < z < 1.2$ and find no evolution in the rest frame K band TFR and in the stellar mass TFR. Weiner et al. (2006) studied the rest frame B and J band TFR for a large (~ 100 and ~ 670 galaxies for B and J respectively) sample of galaxies with redshifts between 0.01 and 1.2. They find $\sim 1.0 - 1.5$ mag evolution in B band between $z = 0.4$ and $z = 1.2$, so avoiding calibration with respect to a local TFR. For J band, they find evolution in the slope of the TFR but not in the overall luminosity. The slope of the TFR changes so that massive galaxies have evolved more strongly than less massive galaxies.

All these studies were done with slit spectroscopy. Recently, some TFRs at high z derived from integral field observations have been published. Swinbank et al. (2006) presented integral field observations of six $z \sim 1$ galaxies targeting the [O II]$\lambda 3727$ line. They found no evolution in I band and 0.5 ± 0.3 mag brightening in rest frame B band. Puech et al. (2008) observed a representative sample of [O II]$\lambda 3727$ emitting galaxies at $z \sim 0.6$. When they restrict their sample to relaxed rotating disks, they find that $z \sim 0.6$ galaxies are 0.66 ± 0.14 mag fainter in rest frame K band than their local counterparts for a given rotation velocity. They find no evidence for evolution in slope. When they include galaxies with perturbed rotation or complex kinematics, they find many outliers from the TFR of the relaxed rotators, especially on the low mass end. For the stellar mass TFR of the relaxed rotators, they found that they have 0.36 dex less stellar mass at given rotation velocity.

As galaxy formation and evolution models are not able to simultaneously reproduce the zero-point, slope and scatter of the TFR in different bands and the luminosity functions, model predictions for evolution of the TFR are very rare. Steinmetz & Navarro (1999) predict 0.7 mag brightening in B band by $z = 1$. Portinari & Sommer-Larsen 2007 present a cosmological N-body / hydrodynamical simulations of disk galaxy formation and predict 0.85 mag brightening in rest frame B band and a non-evolving slope from z=0 to z=1. They find that the stellar mass TFR does not evolve as individual galaxies move along the TFR. Ferreras & Silk (2001) take a backward spec-

trophotometric approach for the prediction of the TFR at $z \sim 1$. They use the observed TFR in different bands and find that the slope of the B and K band TFRs increases from $z = 0$ to $z \sim 1$. Depending on the formation redshift, the offsets from the local TFR for $\log(V) = 2.0$ galaxies are ~ 2 mag for the rest frame B band TFR and slightly more for the rest frame K band TFR. For galaxies with $\log(V) = 2.6$, these number are ~ 0.5 mag and ~ 1.5 mag for rest frame B and K band respectively.

Evolution in the TFR may be interpreted as luminosity evolution or velocity evolution (due to mass accretion or a change in the mass distribution) or a combination of both. The stellar mass TFR may be interpreted as the build-up of the stellar mass of galaxies or structural evolution.

1.4   Observing the TFR at low and high redshift

In the local universe, the velocity fields (VFs) of spiral galaxies are usually measured using the 21 cm line of hydrogen. The H I gas disk may extend much further than the measurable stellar disk. However, H I measurements are limited to the very nearby universe ($z < 0.2$) until the Square Kilometre Array will become available. For high redshift TFR studies, we have to use another tracer of the VF.

Another gas tracer would be CO. TFRs derived from CO measurements are identical to the TFRs derived from H I (Lavezzi & Dickey 1998, Schöniger & Sofue 1997). CO measurements are potentially a good way to observe gas VFs at high redshift. However, observations of CO at high redshift are currently limited to very CO bright and hence dusty galaxies, like submillimeter galaxies, quasi stellar objects (QSO) and radio galaxies (Hainline et al. 2004 and references therein). One gravitationally lensed Lyman Break Galaxy (LBG) has been detected in CO (Baker et al. 2004a). A second attempt to detect a LBG in CO failed, although the attempt was on the dustiest LBG known (Baker et al. 2004b).

Bright optical emission lines, such as Hα, [O III]$\lambda 5007/4959$ and [O II]$\lambda 3727$ can be observed with near infrared spectrographs until redshift 2.4 (for Hα) and higher (for [O III]$\lambda 5007/4959$ and [O II]$\lambda 3727$). Their extent is limited to the star forming disk. In the local universe, the agreement between rotation velocities derived from H I and H II measurements is excellent and the extent of Hα is often sufficiently large to detect the flat part of the RC (Courteau 1997).

Using Hα (or [O III]$\lambda 5007/4959$ or [O II]$\lambda 3727$) also has disadvantages. Only the VFs of galaxies with sufficiently large SFRs can be observed using this technique. However, galaxies with large SFRs may not be suited for TFR studies, as SFR indicators such as EW(Hα) correlate with offsets from the local B band TFR (Kannappan et al. 2002).

The first measurements of RCs at higher redshifts were done with optical long slit spectrographs (Vogt et al. 1996). RCs derived from VFs have some major advantages over long slit spectroscopy. For example, non-circular motions and mergers, of which the frequencies are expected to rise with redshift, are more easily identified. For TFR studies, it is important to exclude galaxies with irregular VFs. Another example of the different results of long slit and integral field spectroscopy is presented by Smith et al. (2004). They present integral field observations of a galaxy previously observed with long slit spectroscopy, targeting the same emission line (Hα). They find a lower limit

to the rotation velocity of 180 ± 20 km s^{-1} while the rotation velocity derived from the long slit spectrum was 120 ± 10 km s^{-1} (Barden et al. 2003). In this case, the emission is dominated by two Hα emitting regions. In recent years, several near-infrared integral field spectrographs have become available (e.g. SINFONI at the VLT in April 2005). Albeit with long integration times (2-8 hours), it is now possible to measure the full VFs of galaxies up to $z \sim 2$ and larger.

With typical galaxy sizes of a few arcseconds, the observed spectra are significantly smeared by seeing. The number of independent data points for high redshift long slit spectra and VFs are therefore much smaller than for local galaxies and the resolution is rarely better than ~ 4 kpc. This may lead to underestimates of the rotation velocity up to 50% and false detections of flattening RCs (Erb et al. 2004). Seeing effects should be carefully modelled when deriving the intrinsic RCs from the observed spectra.

1.5 This thesis

In this thesis, we explore the possibilities of measuring TFRs at high redshift. We start in **Chapter 2** with VLT-ISAAC long slit observations of a subsample of the HST/NIC-MOS grism sample of Hα emitting galaxies at $z \sim 0.8 - 1.6$ (McCarthy et al. 1999). We find a ~ 2 mag offset from the local rest frame B and R band TFR based on a very small number of sources (3). Selection effects and sample properties contribute to this offset, but we cannot quantify the amount because we have very limited photometry for this sample and because we lack a good local comparison sample. The measured offsets are also uncertain because we cannot confirm that the galaxies are dynamically similar to local spiral galaxies. Several improvements can be made in future studies. Studying galaxies with photometry over a large wavelength range enables the study of the rest frame K band TFR and the stellar mass TFR which are less sensitive to starburst and extinction effects. Integral field spectra observed with good seeing will enable us to classify the dynamics of the targeted galaxies. Also, massive galaxies are prefered since selection effects play a smaller role for massive galaxies and reference TFRs show less variation at the high mass end of the TFR.

To gain more insight to the dynamics of individual galaxies, we observed our subsequent targets with SINFONI, the new (April 2005) near-infrared integral field spectrograph of the VLT. We tried to preselect massive disk-like galaxies with available photometry over a large wavelength range for the reasons discussed in Chapter 2.

Our first attempt was on ISO $15\mu m$ selected galaxies. Previous studies by Rigopoulou et al. (2002) and Franceschini et al. (2003) showed that ISO $15\mu m$ detected galaxies at $z = 0.2 - 1.5$ are massive galaxies. Their stellar masses are of order $\sim 10^{11}$ M$_\odot$ (Franceschini et al. 2003). RCs derived from long slit spectra revealed flat RC velocities of > 200 km s^{-1}. Photometric data over a large wavelength range (UB-VRIJHK) is available from the EIS survey (da Costa et al. 1998). Many of these galaxies are also located in the HDF-S FIRES field, for which deep optical and near-infrared photometry and Spitzer/IRAC photometry is available (Labbé et al. 2003a, 2005) so that these galaxies are also suited for rest frame K band and stellar mass TFR analysis.

We present in **chapter 4** observations of three ISO $15\mu m$ detected galaxies from the Franceschini et al. (2003) sample. We detected VFs for two of them, which are con-

sistent with them being massive galaxies. Kinematic data for other galaxies of the Franceschini et al. (2003) sample was obtained by Rigopoulou et al. (2002) and Puech et al. (2008 and references therein). We combine these data to obtain the rest frame B and K band TFR and the stellar mass TFR. The rest frame B band TFR is (as expected) dominated by noise from SFR and extinction differences. The rest frame K band TFR shows much less scatter and we find that the galaxies are on average slightly less luminous (~ 0.5 mag) than expected from the local K band TFR, but the difference is not significant. We study the stellar mass TFR using two different estimates for the stellar mass. Both show a TFR with lower zero-point than the local stellar mass TFR, but the zero-point difference between the $z \sim 0.7$ stellar mass TFRs is almost 0.5 dex. The most important difference between the two methods for estimating the stellar mass is the range of star formation histories allowed. The method that naturally allows for a population of old stars with large M/L finds substantially larger stellar masses. The inferred stellar mass TFR is consistent with that derived from a larger sample with different selection criteria by Puech et al. (2008). The agreement shows that our infrared-based selection criterion selects galaxies suitable for TFR studies.

We then turned to MIPS $24\mu m$ selected galaxies in the HDF-S and MS1054 FIRES fields (Labbé et al. 2003a, Förster-Schreiber et al. 2006a). For these fields, UV+optical+nearIR+IRAC+MIPS photometry is available (Labbé private communication, Labbé et al. 2005, Egami et al. 2006, Gordon et al. 2005). By selecting MIPS $24\mu m$ detected galaxies at $z \sim 2$, we are applying the same selection criterion as for $15\mu m$ at $z \sim 1$. So we can select massive galaxies at $z \sim 2$ and we can make a good comparison to similarly selected and observed galaxies at $z \sim 1$. One of the MIPS selected galaxies is also detected at $850\mu m$ with SCUBA (Knudsen et al. 2005, van Dokkum et al. 2004). The results of this study are presented in **Chapter 5**.

We detect VFs with velocity gradients for three MIPS sources. A fourth VF does not show a velocity gradient. The VF of the fifth source shows a velocity gradient but the S/N is too small to derive a VF. All galaxies are consistent with $V_{flat} > 200$ km s^{-1}. However, the VF of the SCUBA detected galaxy shows deviations from ordered rotation. We detect only half the VF of a second source, which causes additional uncertainties in the interpretation. The VF of the third source is very regular, with $V_{max} > 400$ km s^{-1}. We combine these results with the $z \sim 2$ galaxy described in Chapter 3 (see below) and two galaxies from Förster-Schreiber et al. (2006b). We do not find a consistent relation between rotation velocity and rest frame B and K luminosity or stellar mass.

Labbé et al. (2003b) found 6 morphologically selected candidate large disk galaxies at $z \sim 2$ in the HDF-S FIRES field. These galaxies are characterized by their exponential profiles with scale lengths comparable to those of local disk galaxies. They have redder colors in their centers and are bluer in the outer parts, reminiscent of the red bulges and starformation in the disk of local spiral galaxies. Their (observed) K band profiles are very smooth while the (observed) F814W images show large clumps symmetrically distributed around the center. If truly disks, these galaxies are of course ideal targets for TFR studies. We observed several of these morphologically and photometrically selected disk galaxies. There is significant overlap with the MIPS selected sources at $z \sim 2$.

Our best case from this sample is presented in **Chapter 3**. Although it is part of our $z \sim 2$ sample and is discussed in Chapter 5, we also discuss in in a separate chapter as demonstration of our methods. The gas mass of this galaxy is ~ 3 times larger than its stellar mass, consistent with the best fit age from SED fitting of $\sim 160\,\mathrm{Myr}$. Nevertheless, its VF is very regular and consistent with a rotating disk. The best fit RC rises to $V_{flat} \sim 220\,\mathrm{km\,s^{-1}}$ and then remains flat. This galaxy is consistent with the local rest frame K band TFR and slightly less massive than the local stellar mass TFR (2σ difference). But when a maximally old population is added to the stellar mass, this galaxy is consistent with the local stellar mass TFR.

1.6   Conclusions and future work

We have showed that there exist galaxies up to $z \sim 2$ that are dynamically very similar to local disk galaxies. We had especially much success on morphologically selected disk galaxies. The extent and flux of the Hα emission is a limiting factor in the analysis of about half our $z \sim 2$ sample.

We find that the rest frame K and stellar mass TFR exist at $z \sim 0.7$, consistent with the findings of earlier studies, in particular Puech et al. (2008). Quantifying the amount of evolution in the stellar mass TFR is limited by the SFH of the models used in the SED fitting (and also the stellar evolution models and IMF). Our results are consistent with the results of Puech et al. (2008).

We do not find evidence for the existence of a rest frame K and stellar mass TFRs at $z \sim 2$. However, this conclusion is based on a very small number of sources, some of which are not suited for TFR analysis as their VFs shows significant deviations from circular motions. The extent of the VF of other galaxies is a limiting factor in the VF analysis of other galaxies. A larger sample of dynamically relaxed disk galaxies may reveal a TFR at $z \sim 2$.

References

Arnaboldi, M., Iodice, E., Bournaud, F. et al. 2003 ApJ 585 730
Baker, A.J., Tacconi, L.J., Genzel, R., Lutz, D. & Lehnert, M.D. 2004a ApJ 604 125 140
Baker, A.J., Tacconi, L.J., Genzel, R., Lutz, D. & Lehnert, M.D. 2004b ApJ 613 L113
Bamford, S.P, Aragón-Salamanca & A. & Milvang-Jensen, B 2005 MNRAS 366 308
Bamford, S.P, Aragón-Salamanca & A., Milvang-Jensen, B. & Simard, L. 2005 MNRAS 361 109
Barden, M. et al. 2003 astro-ph 0308272
Barton, E.J., Geller, M.J., Bromley, B.C., van Zee, L., & Kenyon, S.J. 2001 AJ 121 625
Bell, E.F. & de Jong, R.S., 2001, ApJ 550 212
Böhm, A. & Ziegler, B.L. 2007 ApJ 668 846
Brungardt, C.L. 1988 ApJ 327 L51
Chiu, K., Bamford, S.P. & Bunker, A. 2007 MNRAS 0702583
Conselice, C.J., Bundy, K., Ellis, R.S. et al. 2005 ApJ 628 160
Courteau, S. 1997, AJ 114 2402
Courteau, S., Andersen, D.R., Bershady, M.A, MacArthur, L.A. & Rix, H.-W. 2003 ApJ 594 208
Courteau, S., Dutton, A.A., van den Bosch, F.C. et al. 2007, ApJ 671 203
da Costa, L., Nonino, M., Rengelink, R. et al. 1998 astro-ph 9812105
Davoust, E. & Contini, T., 2004 A&A 416 515
Egami, E., Rieke, G.H., Rigby, J.R. et al. 2006 in ASP Conf. Ser., The Spitzer Space Telescope, ed. L. Armus

Erb, D.K. Steidel, C.C., Shapley, A.E., Pettini, M. & Adelberger, K.L. 2004 ApJ 612 122

Ferreras, I. & Silk, J.H. 2001 ApJ 557 165

Förster-Schreiber, N. M., Franx, M., Labbé, I. et al. 2006a AJ 131 1891

Förster-Schreiber, N. M., Genzel, R., Lehnert, M.D. et al. 2006b ApJ 645 1062

Franceschini, A., Berta. S, Rigopoulou, D. et al. 2003 A&A 403 501

Gordon, K.D., Rieke, G.H., Engelbracht, C.W. et al. 2005 PASP117 503

Hainline, L.J. Scoville, N.Z., Yun, M.S. et al. 2004 ApJ 609 61

Kannappan, S.J. & Barton, E.J., 2004 AJ 127 2694

Kannappan, S.J., Fabricant, D.G. & M. Franx 2002 AJ 123 2358

Knudsen, K.K., van der Werf, P., Franx, M. et al. 2005 ApJ 632 L9

Labbé, I., Franx, M., Rudnick, G. et al. 2003a AJ 125 1107

Labbé, I., Rudnick, G., Franx, M. et al. 2003b ApJ 591 L95

Labbé, I., Huang, J., Franx, M. et al. 2005 ApJ 624 81

Lavezzi, T.E. & Dickey, J.M. 1998 AJ 116 2672

Neistein, E., Maox, D., Rix, H.-W. & Tonry, J.L. 1999 AJ 117 2666

Matthews, L.D., van Driel, W. & Gallagher, J.S. AJ 116 2196

McCarthy, P.J., Yan, L., Freudling, W. et al. 1999, ApJ 520 548

McGaugh, S.S., Schombert, J. M., Bothun, G. D. & de Blok, W. J. G. 2000, ApJ 533 99

Mendes de Oliveira, C., Amram, P., Plana, H., & Balkowski, C. 2003 AJ 126 2635

Metevier, A.J., Koo, D.C, Simard, L. & Philips, A.C. 2006 ApJ 060167

Milgrom, M. 1983a ApJ 270 365

Milgrom, M. 1983b ApJ 270 371

Milvang-Jensen. B., Aragón-Salamance, A., Hau, G.K.T., Jorgensen, I. & Hjorth, J. 2003 MNRAS 339 L1

Mo, H. J., Mao, S. & White, S.D.M. 1998 MNRAS 295 319

Nakamura, O., Aragón-Salamanca, A., Milvang-Jensen, B. et al. 2005 MNRAS 366 144

Noordermeer, E. & Verheijen, M.A.W. 2007 MNRAS 381 1463

Portinari, L. & Sommer-Larsen, J. 2007, MNRAS 375 913

Puech, M., Flores, H, Hammer, F. et al. 2008 A&A arXiv:0803.3002

Rigopoulou, D., Franceschini, A., Aussel, H. et al. 2002, ApJ 580 789

Smith, J.K. Bunker, A.J.Vogt NP et a. 2005 MNRAS 0408465

Schöniger, F. & Sofue, Y. 1997, A&A 323 14

Silk, J. 1997 ApJ481 703

Sprayberry, D, Bernstein, G.M., Impey, C.D. & Bothun, G.D. 1995, 438 72

Steinmetz, M. & Navarro, J.F. 1999 ApJ 513 555

Stil, J.M. & Israel, F.P. 1998, astro-ph 9810151

Swinbank, A.M., Bower, R.G., Smith, G.P. et al. 2006 MNRAS 368 1631

Tully, R. B. & Fisher, J. R. 1997 A&A54 661

van den Bosch, F.C. 2000 ApJ 530 177

van Dokkum, P.G., Franx. M., Förster-Schreiber, N.M. et al. 2004 ApJ 611 703

Van Driel, W., van den Broek, A.C., & van Baan, W.A., 1995, ApJ 444 80

Verheijen, M. A. W., 2001, ApJ 563 694

Vogt, N.P. Forbes, D.A., Philips, A.C. et al. 1996 ApJ 465 L15

Vogt, N.P., Philips, A.C., Faber, S.M. et al. 1997 ApJ 479 L121

Weiner, B.J., Willmer, C.N.A., Faber, S.M. et al. 2006 ApJ 653 1049

Chapter 2

On measuring the Tully-Fisher relation at $z > 1$

A case study using strong Hα emitting galaxies at $z \sim 1.5$

The evolution of the line width - luminosity relation for spiral galaxies, the Tully-Fisher relation, strongly constrains galaxy formation and evolution models. At this moment, the kinematics of $z > 1$ spiral galaxies can only be measured using rest frame optical emission lines associated with star formation, such as Hα and [O III]5007/4959 and [O II]3727. This method has intrinsic difficulties and uncertainties. Moreover, observations of these lines are challenging for present day telescopes and techniques. Here, we present an overview of the intrinsic and observational challenges and some ways way to circumvent them. We illustrate our results with the HST/NICMOS grism sample data of $z \sim 1.5$ starburst galaxies. The number of galaxies we can use in the final Tully-Fisher analysis is only three. We find a ~ 2 mag offset from the local rest frame B and R band Tully-Fisher relation for this sample. This offset is partially explained by sample selection effects and sample specifics. Uncertainties in inclination and extinction and the effects of star formation on the luminosity can be accounted for. The largest remaining uncertainty is the line width / rotation curve velocity measurement. We show that high resolution, excellent seeing integral field spectroscopy will improve the situation. However, we note that no flat rotation curves have been observed for galaxies with $z > 1$. This could be due to the described instrumental and observational limitations, but it might also mean that galaxies at $z > 1$ have not reached the organised motions of the present day.

2.1   Introduction

The Tully-Fisher relation (hereafter TFR) is a tight empirical relation between the flat rotation curve (RC) velocity and the luminosity of spiral galaxies (Tully & Fisher 1977). The TFR has been used as a distance estimator and for measurements of the Hubble constant H_0 (e.g. Tully & Pierce 1998).

In addition to its empirical applications, the TFR is interesting in itself because it defines a tight relation between the total (dark matter dominated) mass of spiral galaxies and their luminosity produced by baryons. Furthermore, assuming a stellar mass-to-light ratio M_*/L, the stellar masses of galaxies can be calculated from their luminosities and a stellar mass TFR can be derived (Bell & De Jong 2001). After addition of the gas mass, one obtains the baryonic mass TFR (Verheijen 2001; Bell & De Jong 2001; Mc-Gaugh et al. 2000). The variations in the dark-to-baryonic mass ratio of galaxies are small and deviations from the baryonic TFR are absent down to very low mass galaxies (McGaugh et al. 2000) although others claim a slight deviation for dwarf spirals (Stil & Israel 19998). Semi-analytical models of galaxy formation struggle to explain simultaneously the slope, zero point and tightness of the TFR in all optical and near infrared bands (Van den Bosch 2002).

The tight fundamental relation between mass and luminosity is interesting to study in the context of galaxy evolution. The study of the evolving TFR with redshift can provide valuable information on the luminosity evolution of galaxies and the buildup of stellar mass as a function of galaxy mass. As we will show in this paper, the analysis of high redshift TFRs needs careful treatment of observational limits, selection effects, sample definitions and starburst influences, and high resolution high quality spectra.

In the local universe, HI is used to measure the velocity profiles of spiral galaxies. The gas disk in spiral galaxies extends 2-3 times further out than the stellar disk. HI measurements are currently limited to low redshift, beyond redshift ~ 0.2 HI emission has not been observed (Zwaan et al. 2001) and one has to rely on other kinematic tracers. Another gas tracer could be CO, but CO detections in the high redshift universe are currently limited to very CO bright galaxies, like submillimeter galaxies, quasi stellar objects (QSO) and radio galaxies (Hainline et al. 2004 and references therein). One gravitationally lensed Lyman Break Galaxy (LBG) has been detected in CO (Baker et al. 2004a). A second attempt to detect a LBG in CO failed, although the attempt was on the dustiest LBG known (Baker et al. 2004b).

Bright optical narrow emission lines like Hα, Hβ, [O III]5007/4959 and [O II]3727 can also be used to trace the rotation curve of galaxies. Their presence is limited to the stellar disk (or more precisely: the star forming disk). In the local universe, the agreement between HI and HII measurements of RCs is excellent (Courteau 1997). However, these lines shift out of the optical regime at redshifts 0.4 - 1.4. In recent years, high resolution near infrared spectrographs like the Infrared Spectrometer And Array Camera (ISAAC) at the Very Large Telescope (VLT) of the European Southern Observatory (ESO) have become available, opening the window out to redshift 2.4 (for Hα) TFR studies. Examples are Rigopoulou et al. (2002), who studied massive $z \sim 0.6$ galaxies, Barden et al. (2003) who found an offset from the local B band TFR of $\sim$ 1mag at $z \sim 0.9$, Lemoine-Busserolle et al. (2003) who used gravitational lenses to study two

galaxies at $z \sim 1.9$ and Pettini et al. (2001), who studied Lyman Break Galaxies at $z \sim 3$. We used ISAAC to study the kinematics of a sample of $z \sim 1.5$ Hα emitting galaxies and we present the results in this paper as a case study for $z > 1$ TFR studies.

Our sample is a subsample of the McCarthy et al. (1999) HST/NICMOS grism survey sample. McCarthy et al. (1999) surveyed 64 square arc minutes with the slitless NICMOS G141 grism and detected 33 emission line objects with varying 3σ limiting line fluxes down to 1×10^{-17}erg s^{-1}cm^{-2}. They argue that the detected emission lines are Hα between redshift 0.75 and 1.9. The Hα+[N II]6548/6584 complex is not resolved due to the low spectral resolution ($R \sim 150$) of the grism and therefore contamination by other emission lines (particularly [O III]5007/4959) cannot be excluded and no kinematic information is obtained. This sample is biased to galaxies with large Hα equivalent width, EW(Hα), and Hα flux, F(Hα), due to the low spectral resolution of the grism. We chose this sample because it has clear selection criteria and all sources have known Hα fluxes.

Here, we present observations of 9 objects from the McCarthy et al. sample with the ISAAC at the VLT in medium resolution mode ($R \sim 3000 - 5000$). Our aim was to resolve the Hα+[N II] complex (or the [O III]5007/4959 doublet) to confirm redshifts, measure accurate line fluxes and linewidths and if possible also rotation curves. We use this data to present our case study for $z > 1$ TFRs.

Hicks et al. (2002) also performed a follow-up of the HST/NICMOS grism sample. They observed 14 objects aiming to detect emission lines, particularly [O II]3727 in the optical (R/I band) using LRIS at the Keck telescope. They observed in low resolution mode ($R \sim 350 - 700$ depending on the grating used) and therefore did not obtain any kinematic information. They confirmed the redshift from McCarthy et al. (1999) for 9 out of 14 objects. They explained the non-confirmations by twilight observations or the presence of a nearby bright star (emission lines may very well be not bright enough to detect in these two cases). In two cases, the [O II]3727 line was outside the observed wavelength range and other emission lines like for example C II]2326, C III]1909 and Mg II2800 might have been too faint to detect. The fifth non-detection was explained by reddening or the emission line detected by McCarthy et al. was not Hα but Hβ or [O III]5007/4959. In the latter case, no bright emission lines are expected in the wavelength range observed.

Our follow-up is complementary in two ways: we observe the objects accessible from the southern hemisphere whereas Hicks et al. observed from the northern hemisphere. Only one object (J0931-0449) is in both samples. Second, we observe at higher resolution, resolving the emission lines.

This paper is organised as follows. The first part of the paper describes the case study data set: the observations of the NICMOS grism sample (Section 2), data reduction and analysis (Section 3), the sample properties (Section 4) and notes on individual galaxies (Section 5). The second part of the paper discusses high redshift TFRs using the earlier discussed dataset as an illustration with a strong focus on pitfalls (Section 6). We conclude with a summary and conclusion in the final section (Section 7).

Throughout this paper, we assume $\Omega_M = 0.3$, $\Omega_\Lambda = 0.7$ and $H_0 = 70$ km s^{-1}Mpc^{-1}. All magnitudes in this paper are Vega magnitudes.

Table 2.1 — Observations

Source ID	run ID	slit width	T_{int}(s)	*seeing*[b]
J0627–6512	68.A–0243(A)	$1''$	7200	$0\overset{''}{.}69$
J0738+0507a	68.A–0243(A)	$1''$	7200	$0\overset{''}{.}83$
J0738+0507b	70.A–0304(A)	$0\overset{''}{.}6$	15000	$0\overset{''}{.}60$
J0931–0449	68.A–0243(A)	$1''$	7200	$0\overset{''}{.}80$
J1056–0337	68.A–0243(A)	$1''$	14400	$0\overset{''}{.}67$
J1143–8036a[a]	68.A–0243(A)	$1''$	7200	$0\overset{''}{.}78$
J1143–8036b[a]	68.A–0243(A)	$1''$	7200	$0\overset{''}{.}78$
J1143–8036c	68.A–0243(A)	$1''$	7200	$0\overset{''}{.}91$
J1143–8036d	70.A–0304(A)	$0\overset{''}{.}6$	12000	$0\overset{''}{.}60$

[a] J1143-8036a and J1143-8036b were observed in the same slit.
[b] The seeing was measured on the brightest object in the slit in the reduced image. In one case, J1056-0337, there was no bright object in the slit and the seeing was measured on the standard star for flux calibration.

2.2   Sample selection and observations

The McCarthy et al. (1999) catalog contains 33 galaxies with redshifts between 0.75 and 1.9. We selected all targets from the McCarthy et al. (1999) sample accessible with the VLT and with the line falling in the J or H atmospheric window. We did not select on morphology or emission line flux.

The observations were done in two runs. In the nights of February 23, 24 & 25 2002 (ESO program ID 68.A-0243(A)) we observed 7 targets in visitor mode using the VLT ISAAC long slit spectrograph in medium resolution (MR) mode with $1''$ slit under varying atmospheric conditions. In winter 2003 (ESO program ID 70.A-0304(A)) two targets were observed in service mode under excellent seeing and sky conditions (seeing $< 0\overset{''}{.}6$, clear/photometric) with the $0\overset{''}{.}6$ slit. Integration times varied between 120 to 250 minutes, depending on the atmospheric conditions and the emission line flux. One target could not be acquired, although it was attempted several times. An overview of all observations is given in Table 2.1.

The observational set-up was as follows. The slit was aligned along the major axis of the galaxy as determined from NICMOS H band images. Where possible without deviating more than $10°$ from the major axis of the galaxy, a bright reference star was also included in the slit to make sure the slit was on target. To facilitate sky subtraction, total integration times were dived in 12 or 15 minutes exposure times, nodding in ABBA cycles along the slit. After observation of each object, a bright nearby standard B star was observed with the same instrument setup and the same air mass to allow accurate flux calibration. For the $0\overset{''}{.}6$ slit observations, the B star was also observed with the $2''$slit to calculate the (wavelength dependent) slit loss correction. Depending on wavelength and slit width, the sampling was 0.57 to 0.81 Å pix^{-1}. The full width half maxima (FWHM) of the sky lines varied between 3.3 and 4.7 Å.
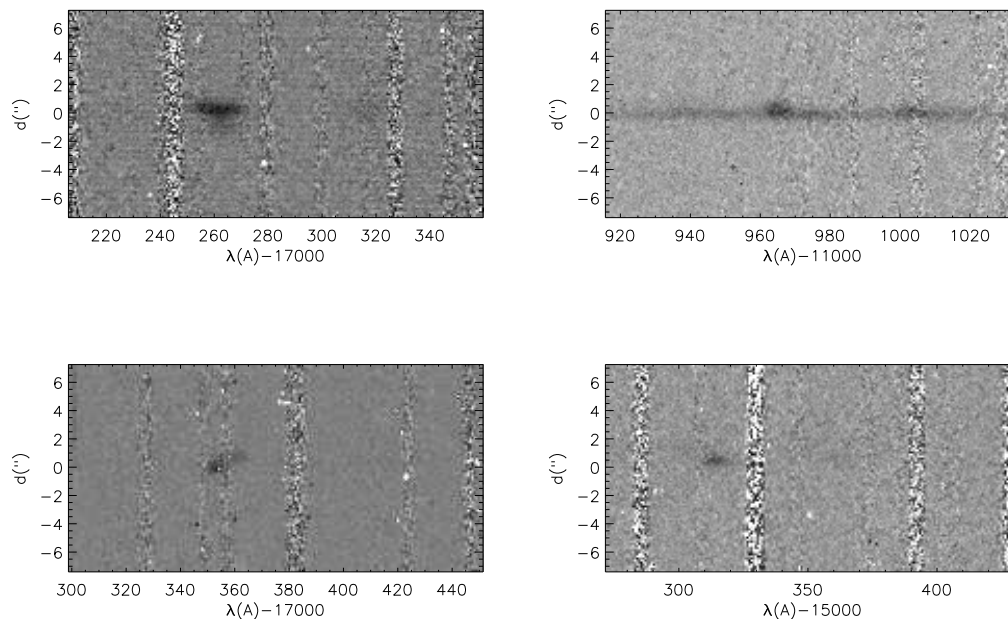
Figure 2.1 — Two dimensional spectra, from the upper left and then clockwise: J0627-6512, J0738+0507a, J1143–8036a and J0738+0507b. Note the extended emission in J0627-6512 and J0738+0507b and the positions of the OH sky lines in all spectra.

2.3 Data reduction and analysis

We used standard eclipse (Devillard 1997) and IRAF procedures for data reduction. The available twilight flats were used to create a bad pixel map. We removed bad pixels, ghosts and cosmic rays in all frames before combining them. Except for one object (J1143-8036c) we used dome flats for flat fielding. An illumination correction to these flat fields was done to remove a small residual gradient in the sky. Residual bias subtraction was only necessary for the objects with the highest quality data (J0738+0507b and J1143-8036d). The spectral tilt was removed using star traces. The OH lines were used to correct for the curvature of spectral lines. If the detected emission line was close to one of the edges of the detector, we recalculated this correction optimising it for the area around the emission line to minimise OH line residuals where they are most relevant.

Flux calibration was done using bright B stars, observed directly after the object. A (wavelength dependent) slit loss correction was applied to the 0.″6 slit spectra. The OH lines were used for wavelength calibration, < 0.5 Å residuals remained after a third order fit.

One or more emission lines are immediately visible in the two dimensional spectra in 5 out of 9 cases. In two cases, we also detect continuum emission, in one case, we detect continuum emission without an emission line (J1056-0337). One detection turns out to be a Seyfert 1 (J0931-0449). The reduced two dimensional spectra of the detected emission lines are shown in Fig. 2.1 (except the Seyfert).

Table 2.2 — Emission lines detected

source ID	$\lambda(\mu\text{m})$	line ID	z	F^a	$F_{\text{OH}}^{\text{ab}}$
J0627–6512	1.72616	Hα	1.630	4.0 ± 0.2	
J0627–6512	1.73167	[N II]6584	1.630	0.59 ± 0.05	
J0738+0507a	1.1966	Hα	0.824	2.9 ± 0.3	$\sim 4.1 - 4.7$
J0738+0507a	1.2005	[N II]6584	0.824	2.0 ± 0.2	$\sim 2.3 - 3.7$
J0738+0507a	1.19411	[N II]6548	0.824	1.6 ± 0.2	
J0738+0507b	1.7354	Hα or [O III]5007	1.644 or 2.466	0.74 ± 0.02	$\sim 0.9 - 1.0$
J0931–0449	1.2973	Hα + [N II]6548/6584	0.977	21 ± 5	
J1143–8036a	1.53137	Hα	1.333	0.73 ± 0.06	
J1143–8036a	1.53623	[N II]6584	1.333	0.16 ± 0.03	

^a Fluxes in units of 10^{-16}erg s^{-1}cm^{-2}.

^b F_{OH} is an estimate of the emission line flux F had it not been contaminated by one (or more) OH sky lines.

We extracted one dimensional spectra by cutting out a strip from the two dimensional spectrum containing all flux of the detected emission line, or, if there was no (clear) detection in the 2D spectrum, a strip was cut out at the expected position of the emission line (using the known distance between the object and the reference star). Extracting the spectrum by tracing the spectrum was not an option, because we detect weak continuum emission in only three sources. The spectra were smoothed with a Gaussian with FWHM approximately equal to the FWHM of the OH lines in the raw frames and are shown in Fig. 2.2. In the one dimensional spectra, a second or third emission line is immediately evident in two cases. The brightest emission line of every detected object was clearly visible in the two dimensional spectrum.

Line fluxes and widths were measured by fitting a Gaussian to the detected emission lines using IRAF's 'splot'. Errors were estimated by repeated fitting with different parameters. If there was severe OH line contamination, we interpolated over the OH line to correct for flux losses. Error bars are naturally larger in this case. Linewidths were corrected for instrumental broadening and converted to W_{20}, the width at 20% of maximum flux. Line fluxes and widths are given in Tables 2.2 and 2.3 respectively. Values corrected for OH line contamination are marked by the subscript 'OH'.

We calculated rest frame B or R magnitudes (depending on redshift) from the observed F110W (J hereafter) and F160W (H hereafter) magnitudes. An H band magnitude was available for all targets, J band for a subset only. When J band photometry was unavailable, we used the average J-H color (equal to the median color) of the entire NICMOS grism sample to estimate the J band magnitude. We calculated the rest frame magnitudes by interpolating between the J and H fluxes, depending on redshift this gives us a rest frame B or R absolute magnitude. Where we could not interpolate to obtain a rest frame B or R magnitude, we made a rough estimate of this magnitude by using the closest flux point available. The errors in the absolute magnitudes were

Table 2.3 — SFRs and masses.

Source ID	SFR $M_\odot yr^{-1}$	SFR_{OH} $M_\odot yr^{-1}$	W_{20} kms^{-1}	$W_{20\ OH}$ kms^{-1}	M $10^{10}M_\odot$	R^a kpc
J0627–6512	57 ± 3		344 ± 11		4.8	7
J0738+0507a	20 ± 2	$\sim 28 - 32$	398 ± 38	$\sim 479 - 677$	5.1	6
J0738+0507b[b]	10.9 ± 0.3	$\sim 13 - 15$	166 ± 3	$\sim 216 - 235$	1.3	8
J0931–0449[c]	167 ± 40		5300 ± 1800			
J1143–8036a	8.2 ± 0.7		274 ± 18		1.7	4

[a] R is half the diameter, measured as the total extent along the slit in the spectrum.
[b] SFR and mass were calculated assuming the emission line observed is $H\alpha$.
[c] J0931–0449 is a Seyfert 1 galaxy, the SFR is not meaningful.

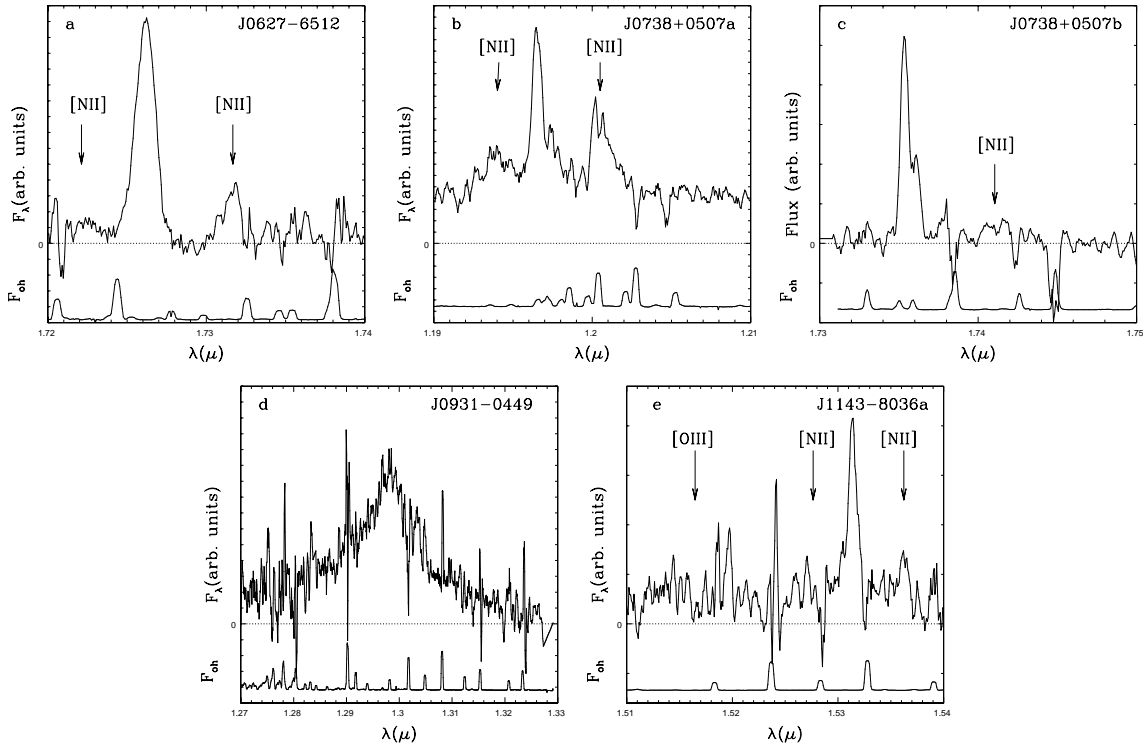**Figure 2.2** — 1D spectra for all sources. Assuming the brightest emission line detected is $H\alpha$, the expected position of the [N II]6584/6548 lines are marked. If [N II]6584/6548 is not or marginally detected, we also marked the expected position of [O III]4959 assuming the brightest emission line is [O III]5007. Note that [O III]4959 and [N II]6548 fall outside the wavelength range observed for object J0738+0507b.

Table 2.4 — Apparent magnitudes and absolute magnitudes of targets

Source ID	J	H	M_B	M_R
J0627–6512	22.2	20.4	-22.3 ± 0.1	(-23.1 ± 0.5)
J0738+0507a	$< 18.8 >$	17.9	$(-22.5 \pm 2\ )$	-23.7 ± 0.1
J0738+0507b	$< 22.9 >$	22.0	-20.7 ± 0.1	(-21.5 ± 0.5)
J0738+0507b([O III])	$< 22.9 >$	22.0	-21.7 ± 0.1	$(-22.9 \pm 2\ )$
J0931–0449	19.7	19.0	$(-22.2 \pm 2\ )$	-23.2 ± 0.1
J1143–8036a	$< 22.3 >$	21.4	(-20.6 ± 0.5)	-21.4 ± 0.1

[a] J and H band magnitudes from McCarthy et al. (1999). The J magnitudes calculated from the H band magnitude and average J-H color are marked by $< >$. The extrapolated absolute magnitudes and their errors (see text) are in parentheses.

calculated as follows: while interpolating between the J and H magnitudes, interpolating meaning that the redshifted effective wavelength of the B or R band lies in between the effective wavelengths of the J and H band, we set the error in the measured magnitudes to 0.1, and in the J magnitudes calculated from the average J-H color to 0.4 (=scatter in J-H color). We then interpolated the fluxes and uncertainties to get the rest frame magnitudes and errors. When the effective wavelength of the redshifted B or R band was not between the effective wavelengths of the J and H band but inside the wavelength range of the J or H band, we set the error to 0.5 mag. If it was outside the wavelength range of the J and H band, we set the error to 2.0 mag. These numbers are a bit arbitrary, but are intended to reflect the increased uncertainties in the magnitudes estimates. The apparent infrared magnitudes and corresponding absolute rest frame magnitudes are given in Table 2.4. When calculating the offsets from the TFR, we use only those points where the redshifted B or R filter at least overlapped with the observed J or H band.

2.4   Results

We detect one or more emission lines in 5 out of 9 spectra. One dimensional spectra (of the relevant wavelength ranges of the original ISAAC spectra) are shown in Figs. 2.2a-e. In these figures, the expected positions of the [N II]6584/6548 lines (assuming the brightest emission line detected is Hα) are marked. If the observed emission line is not Hα, the next most likely candidate is [O III]4959/5007. Also marked is the expected position of [O III]4959 (assuming the bright line detected is [O III]5007) if the detection of the [N II] doublet is uncertain. To avoid confusion between emission lines and OH line residuals, the sky spectra are also shown. Other possible identifications of the emission lines can be ruled out or are far less likely: [O II]3727 would put the sources at redshifts larger than 3 (H band detection) and would be resolved in a doublet which is not observed. The equivalent width of Hβ is in general too low to be detected in the McCarthy et al. (1999) survey. We find 4 Hα emitting galaxies and 1 (likely) [O III]5007/4959 emitting galaxy. In Sect. 5, we discuss all galaxies individually.

Table 2.5 — Comparison with the line fluxes and wavelengths of McCarthy et al.

Source ID	$\lambda_{McC}(\mu m)$	$\lambda(\mu m)$	$\Delta\lambda(\text{Å})$	F^a_{McC}	F^a	F^a_{OH}
J0627–6512	1.742	1.72616	158	1.8 ± 0.5	4.0 ± 0.2	
J0738+0507a	1.210	1.1966	134	16 ± 1.5	2.9 ± 0.3	$\sim4.1-4.7$
J0738+0507b	1.77	1.7354	346	0.9 ± 0.3	0.74 ± 0.02	$\sim0.9-1.0$
J0931–0449	1.299	1.2973	17	24 ± 1.7	21 ± 5	
J1143–8036a	1.538	1.53137	66	1.2 ± 0.4	0.73 ± 0.06	

[a] All fluxes are in units 10^{-16}erg s^{-1}cm^{-2}.

In Table 2.5, we list the wavelengths and fluxes from McCarthy et al. (1999). We note that there is a systematic offset between the wavelength as found by McCarty et al. (1999) and ours, although all our wavelengths lie within 3σ error bars of the NICMOS wavelengths. We checked some of the OH lines in the ISAAC spectra and they were correct within a few Å. We also note that the emission line fluxes are not always in agreement. This is probably due to a combination of the low resolution of the NICMOS grism and slit losses with ISAAC.

In Table 2.3 we list starformation rates (SFRs) and dynamical masses for all detected objects. SFRs were calculated using

$$\text{SFR}(\text{M}_\odot\text{yr}^{-1}) = \text{L}_{H\alpha}(\text{erg s}^{-1})/1.26\times10^{41} \tag{2.1}$$

(Kennicutt et al. (1998) for a Salpeter Initial Mass Function (IMF)).

Dynamical masses were calculated using

$$M(R) = \frac{RV^2}{G} \tag{2.2}$$

where the velocity $V = W_{20}/2$ and the diameter $R = D/2$. D is the diameter of the galaxy measured as the total extent in the spectrum. We also measured the diameters in the images with gave consistent results. The masses and radii are also listed in Table 2.3. Note that these masses are lower limits as no correction for inclination or OH lines has been applied.

The [N II]/Hα ratio can be used to get an estimate of the metallicity of galaxies. We used the calibration of Denicoló et al. (2002) and the results are reported in Table 2.6.

2.5   Notes on individual objects

We will now discuss all galaxies individually, paying attention to the identification of the emission line(s), Hα/[N II] ratios, linewidths and kinematics. Where we do not detect any emission line, we will attempt to give an explanation.

J0627-6512   A single bright emission line is visible between two bright OH lines (see Figs. 2.1a and 2.2a). Although [N II]6584 emission is not visible by eye in the two

Table 2.6 — Metallicity

Source ID	[N II]/Hα	log([N II]/Hα)	$12 + \log(O/H)$
J0627–6512	0.125 ± 0.020	-0.90 ± 0.16	8.46 ± 0.16
J0738+0507a[a]	0.69 ± 0.14	-0.16 ± 0.20	9.00 ± 0.16
	$\lesssim 1 \pm 0.1$	$\lesssim 0 \pm 0.1$	$\lesssim 9.12 \pm 0.09$
J0738+0507b	$\lesssim 0.005^{b} \pm 0.005$	$\lesssim -2.3 \pm 1$	$\lesssim 7.4 \pm 0.8$
J1143–8036a	0.22 ± 0.06	-0.66 ± 0.27	8.64 ± 0.22

[a] The OH line corrected values are on the second row. Note this galaxy is probably a narrow line AGN and the line ratio cannot be interpreted as a metallicity effect.

[b] This upper limit is based on the bright part of the emission line, measured in 2D image (to get best constraint)

dimensional spectrum, it is quite obvious in the one dimensional spectrum. Hence, we confirm the redshift to be 1.630. The [N II]6584/Hα ratio is about 0.13, confirming that we are looking at a star forming galaxy (Brinchmann et al. 2003, Gallego et. 1997). We do not detect continuum emission in the spectrum.

In the NICMOS image, this object looks like an asymmetric edge-on galaxy. Indeed, we do detect some extended emission in the spectrum on the same side of the galaxy as in the image. Remarkably, the emission line is not tilted, and there is no sign of ordered rotation. The elongated appearance of the galaxy could be intrinsic, and not due to an edge-on orientation. We might also miss a tilt in the emission line due to the observation conditions, see Sect. 2.6.3 for a discussion of this possibility. The optical seeing during these observation varied between 0.″65 and 1.″24 (median seeing 0.″75). With current data, we cannot distinguish between the two possibilities. We would need excellent seeing, better S/N (the S/N of the extended emission is poor) data with a smaller slit to determine the nature of J0627-6512.

J0738+0507a   This is a very bright source, both in emission line and in continuum flux. We detect Hα, [N II]6548 and [N II]6584 and continuum emission at redshift 0.823. Because of its brightness and its compact morphology, it has been suggested that J0738+0507a hosts an Active Galactic Nucleus (AGN) (McCarthy et al. 1999, Hicks et al. 2002). However, our detection of narrow emission lines rules out the possibility of a Seyfert 1. Star forming galaxies and AGNs can be distinguished from their emission line ratios due to their different excitation properties. The most suited line ratio diagram to separate star forming galaxies from AGNs is the line ratio diagram with log([N II6584]/Hα) on one axis and log([O III]/Hβ) on the other axis (e.g. Brinchmann et al. 2004). We do not have measurements of all these lines, but the ratio log([N II]/Hα) can identify some (but not all) AGNs. According to Brinchmann et al. (2004), all galaxies with log([N II]/Hα) > -0.2 are AGNs. The measured log([N II]/Hα) ratio for J0738+0507a is quite uncertain, because both lines are contaminated by OH line emission. The measured value (see Table 2.6) is -0.16 ± 0.20. The true value is most probably larger (less negative), because the [N II] line is more contaminated then the

Figure 2.3 — Rotation curve of J0738+0507b. The shaded areas correspond to OH lines.
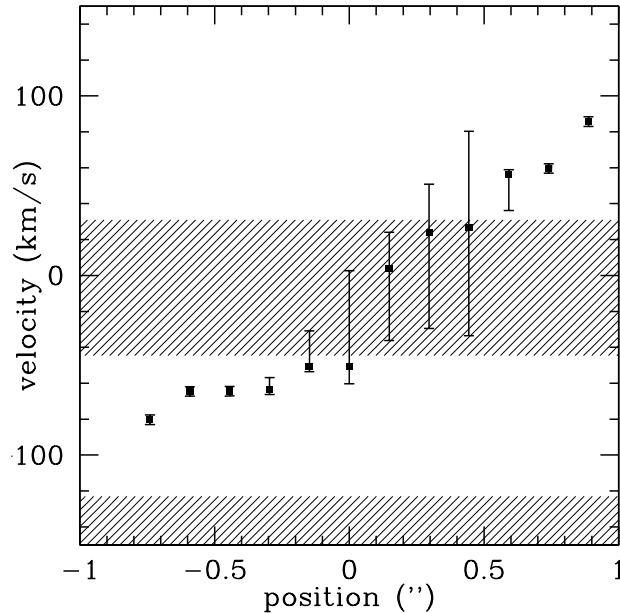
Hα line. We suggest that J0738+0507a is likely a narrow line AGN.

J0738+0507b This galaxy was observed under excellent atmospheric conditions with the 0″.6 slit and a total integration time of just over 4 hours. McCarthy et al. (1999) refer to it as a "putative emission line". We detect a beautifully tilted emission line, extending $\sim 1''.8$ (1″ corresponds to ~ 8 kpc at the source redshift, see below) and rising continuously without flattening off, see Fig. 2.1c and Fig. 2.3. The rotation curve velocity $2V$ is at least ~ 110 km s^{-1} (total visible extent of the emission line without correction for inclination or the OH line cut off (see below)).

The wavelengths of the OH sky lines turn out to be very unfortunate: one bright OH line cuts off the detection on the short wavelength side, another falls on the middle of the emission line, making it hard to put strong limits on emission line flux, extent and velocity. Strictly speaking we can only measure lower limits.

What is clear however, is that we do not observe a double horned profile. What we observe is a bright part and a much fainter part on the long wavelength side. It is possible that a similar fainter outer part is also present on the short wavelength side, but this is impossible to detect due the the presence of the bright OH line at that side of the emission line. Comparing the flux as a function of position in the spectrum to the flux in the image, and assuming that the equivalent width of the emission line does not vary with position, we checked that there is some continuum flux in the image at the undetectable position in the spectrum. We could therefore be looking at a centrally star bursting system, with lower levels of star formation in the outer parts.

As can be seen in Fig. 2.2c, there is no sign of [N II]6584 and there is no bright OH line close to the expected position of [N II]6584. We can rule out an Hα/[N II]6584 ratio smaller than 190 at the 3σ level (for the brightest part of the emission line, assuming constant Hα/[N II]6584 for the whole galaxy). The highest Hα/[N II]6584 ratios observed for local starburst galaxies are ~ 20 for Blue Compact Dwarfs with some out-

liers with ~ 100 (Gallego et al.1997, Brinchmann et al. 2003), therefore identification of the emission line as Hα seems unlikely.

Unfortunately, the detected emission line is close to the edge of the detector. Both [N II]6548 (assuming Hα) and [O III]4959 (assuming [O III]5007) fall off the detector, prohibiting confirmation of [O III]5007/4959. Although McCarthy et al. (1999) could in principle have resolved the [O III] doublet (the separation between the lines at this redshift would be about twice their resolving limit), the small line flux immediately explains why they could not in this case. We conclude that [O III]5007 is the most likely candidate, putting the redshift at 2.466 (instead of 1.644) and making this object one of the highest redshift objects with ordered rotation. We note that high redshift [O III] emitting galaxies have been misidentified as Hα before: Moorwood et al. (2003) find that most of their presumed Hα emitters are [O III]5007/4959 emitters.

J0931-0449   This galaxy is identified as an AGN: it has a very broad emission line (FWHM ~ 2500 km s^{-1}), confirmed to be Hα (and [N II]6548 and [N II]6584) by Hicks et al. (2002) who detected [O II]3727.

J1056-0337   The emission line of this galaxy was not detected, although the emission line flux reported by McCarthy et al. (1999), 4.6×10^{-16}erg s^{-1}cm^{-2}, is by far not the faintest in the sample and we do detect continuum emission. Possible explanations are sky line contamination (parts of the spectra are very crowded with OH lines), extended emission, or a spurious source in the NICMOS sample (J1056-0337 is the lowest redshift object from the NICMOS sample, the emission line is near the edge of the wavelength range covered by the NICMOS grism, the signal-to-noise of the detection is only 3). This object has also been observed as part of the FIRES survey of MS1054-03 (Förster-Schreiber et al. 2005), and has photometric redshift of 0.4 (Franx, private communication) whereas the redshift according to McCarthy et al. is 0.72.

J1143-8036a   This source has the lowest S/N detection in our sample. We see a tentative detection of [N II]6584, although we cannot rule out other possibilities. Continuum emission is not detected.

J1143-8036b   J1143-8036a and J1143-8036b were detected by McCarthy et al. (1999) as a pair with nearly identical redshifts. J1143-8036b was the fainter one of the pair, and here we barely detect J1143-8036a (the distance to the reference star of the detected emission line ruled out the other interpretation: non-detection of J1143-8036a, detection of J1143-8036b). As J1143-8036b has lower emission line flux than J1143-8036a, and J1143-8036a was barely detected, J1143-8036b is probably below the detection limit.

J1143-8036c   This galaxy was not detected. The emission line may fall below the detection limit or the line may fall on top of a bright OH line.

J1143-8036d   This galaxy was not detected in the spectrum despite excellent observing conditions and long integration times. We cannot explain this.

J1120+2323a   This galaxy was scheduled in service mode under excellent conditions, but could not be identified on the acquisition image, is spite of repeated attempts.

We confirm line emission in 5 out of 9 galaxies, including one Seyfert 1, one possible Seyfert 2 and three starburst galaxies. In one case, the emission line is most likely [O III]5007 instead of Hα. The results in this paper are therefore based on a very small number of sources (three), one of them having an uncertain redshift.

2.6   The Tully-Fisher relation at $z > 1$

We will now turn to the discussion of high redshift TFRs, using the NICMOS galaxies as a case study. We will first use this data set to present the $z \sim 1.5$ starburst TFR without any corrections whatsoever. Then, we discuss extinction and inclination corrections for high redshift galaxies. We will then explain our choices for the velocity parameter, the luminosity parameter and the local comparison sample, and how the results would change if other choices had been made. Finally selection effects in velocity, magnitude, sample specifics and star formation are discussed. The whole discussion is strongly focused on the pitfalls of high redshift TFR analysis in order to assess what can be attributed to an evolving TFR and what to peculiarities of this and other samples.

2.6.1   The $z \sim 1.5$ starburst TFR

For the case study, we study the rest frame B and R band starburst TFR using W_{20} on the velocity axis. As a local reference sample, we take the Verheijen (2001) B and R band TFR with again W_{20} on the velocity axis. This sample has been corrected for inclination and extinction (extinction correction recipe from Tully et al. 1998). The Verheijen sample consists of spiral galaxies form the Ursa Major cluster and is among the tightest TFRs in the literature. The velocities are HI measurements.

In Figs. 2.4a and b we plot the local B and R band TFR of Verheijen (2001) with our redshift ~ 1.5 objects, which were not corrected for inclination or extinction. All points lie significantly above the local TFR. Without any corrections (and excluding the possible narrow line AGN J0738+0507a), we estimate that the $z = 1.5$ TFR lies ~ 2.0 magnitudes above the local TFR in B and ~ 1.8 magnitudes in R at $\log(W_{20}[\text{km s}^{-1}]) \sim$ 2.5. For comparison, using ISAAC in a similar way, Barden et al. (2003) found an offset of around 1 magnitude at $z \sim 1$.

2.6.2   Effects of extinction and inclination

Contrary to the local reference sample used (and most local TFRs), our data has not been corrected for extinction and inclination. We did not attempt to correct our data points for extinction or inclination because both corrections are very uncertain for our data. Not correcting for extinction means that we measure a lower limit to the offset from the TFR.

Correcting velocities (line widths) for inclination would decrease the measured luminosity offset. To bring the sample on the local TFR, the required shift in $\log(W_{20})$ is
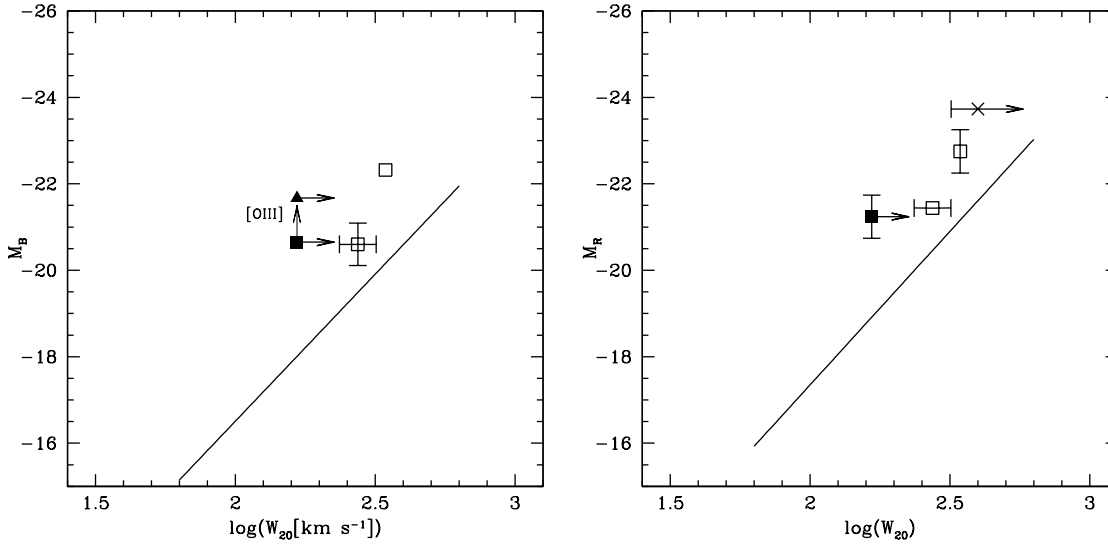
Figure 2.4 — The local B band (left figure) and R band (right figure) TFR of Verheijen (2001) with over plotted the $z \sim 1.5$ NICMOS galaxies. The two solid symbols both correspond to J0738+0507b for different redshift identifications. They are connected by an arrow to make this clear. The triangle is J0738+0507b assuming the detection emission line is [O III] instead of Hα (this point is not in the R band TF plot because its rest frame R magnitude is highly uncertain, see Table 2.4). J0738+0507a is presumably a Seyfert 2 galaxy and is marked by a cross. The arrows indicate an estimate of underestimation of the linewidth due to influence of nearby OH lines. As discussed in Sect. 2.6.3 the linewidths are subject to a large number of uncertainties. For example, if a correction for beam smearing could be made, all linewidths would shift even further to the right. If the error bars were comparable or smaller than the point sizes, they were left out for reasons of clarity.

0.29 in B and 0.25 in R. Assuming random inclinations, the average shift in $\log(W_{20})$ would be 0.3. Therefore, the lower limit to the luminosity offset is ~ 0.

However, the effects of extinction and inclination are not independent: more inclined galaxies are more heavily extincted. Depending on inclination and velocity width (if the extinction correction is velocity dependent like the Tully et al. (1998) correction), the slope of the shift in position between the location of the uncorrected and corrected point in the TF plot, is steeper or shallower than the slope of the (local) TFR, and the measured luminosity offset increases or decreases respectively. For large inclinations (edge-on galaxies), the net effect is a lower limit on the luminosity offset. In Fig. 2.5, we plot the combined effect of extinction and inclination correction using the (local) correction recipe of Tully et al. (1998). Plotted are the local TFR from Verheijen (2001) and vectors showing where points on the TFR would lie if they had not been corrected for extinction and inclination for inclinations of 80°, 70°, 60°, 50° and 40°. The figure shows that for galaxies at the relevant velocity range, we measure a lower limit to the luminosity offset if they are more inclined than $\sim 60°$. Increasing the amount of extinction (and/or a shallower local TFR, the Verheijen TFR is among the steepest known) lowers this turnover inclination. One magnitude extinction more than locally lowers the turnover inclination to $\sim 40°$. For a sample of galaxies with random inclinations, the net effect on the measured luminosity offset is then ~ 0. Although we cannot measure the inclinations accurately, we can say that J0627-6512, J0738+0507b

Figure 2.5 — The combined effect of extinction and inclination. Plotted are the local TFR of Verheijen (2001) with the vectors showing where a galaxy lying on the TFR would lie if it had not been corrected for inclination and extinction (according to Tully et al. 1998) for inclinations 80°, 70°, 60°, 50° and 40° from bottom to top.
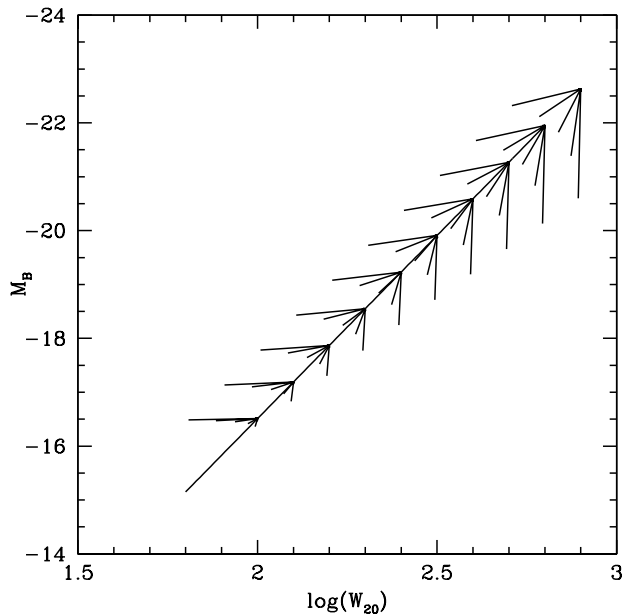
and J1143-8036a are significantly inclined, given their elongated morphology even at limited spatial resolution. Therefore, we are confident that the measured offsets are lower limits to the luminosity offset, although the precise amount remains uncertain due to the small number of sources.

Of course this result relies on the assumption that local extinction corrections apply for the galaxies in our sample, which is uncertain. Under this assumption however, the measured offset from the local TFR is robust against the combined effect of inclination and extinction.

Accurate inclinations for high redshift galaxies can be obtained with high resolution imaging. Without any extinction correction, the measured offsets from the local TFR are then lower limits by definition. If high resolution imaging is not available, the above approach minimises uncertainties. For all high redshift TFR samples, one has to assume local extinction corrections apply for high redshift galaxies unless an independent estimate of the extinction is available. The Balmer decrement or SED fitting could constrain the extinction, although the latter method suffers from degeneracy between age and dust.

2.6.3 Velocity: W_{20}

A number of different parameters may be plotted on the velocity axis of the TF-plot. Examples for rotation curves are the maximum rotation curve velocity V_{max} and the velocity of the flat outer part of the rotation curve V_{flat}. When using linewidths (double horned profiles) one usually takes the width at some percentage (50% or 20%) of the maximum flux or average flux of both horns. A number of possible corrections may be applied to those linewidths, for example for instrumental broadening and mass motions. All TFR velocity parameters correlate well with eachother. The tightest TFRs are found using V_{flat}, which traces best the total mass of the galaxy, on the velocity axis (Verheijen 2001).

We use the width at 20% of maximum flux W_{20} as an approximation for twice the flat rotation curve velocity V_{flat}. We correct the measured linewidth for instrumental broadening. We choose W_{20} as our line width definition because in local Tully-Fisher samples, the difference between $2V_{flat}$ and W_{20} is smallest (compared with other line width definitions).

Although there are some prescriptions to convert the HII W_{20} linewidth to velocity or HI linewidth (see Rix et al. 1997, Pisano et al. 2001), we did not apply any of those as they give contradicting corrections factors. Pisano et al. (2001) show for a sample of nearby blue compact galaxies that the correction factor from W_{20}(HII) to W_{20}(HI) is large ($\sim 20\%$ or more) for galaxies with small linewidths (W_{20}(HII) $\lesssim 140$ km/s) and small for galaxies with large linewidts (less then 10% for galaxies with linewidths comparable to ours). On the other hand, they also find that for galaxies with equivalent width comparable to ours, the HII linewith is up to a factor 2 smaller than the HI linewidth. Rix et al. (1997) cite different studies investigating the relation between optical linewidths and flat circular velocity. They conclude that W_{20}(HII) should be corrected upward by 14% regardless of W_{20}(HII), equivalent to reducing the luminosity offset by 0.2 mag in B band for the slope of the Verheijen (2001) TFR. We conclude that the uncertainty in the correction factor is significant although the correction in $\log(W_{20})$ (and hence luminosity offset) is probably small. Therefore, we decide not to correct the W_{20} linewidth (except for instrumental broadening).

A crucial assumption in our analysis is that the velocity widths and the rotation curve velocity (in the case of J0738+0507b) trace the mass of the galaxy in a similar way as in the nearby universe. That is, that linewidth traces the ordered rotation of the outer parts of the galaxy where the rotation velocity is constant. This assumption is highly non-trivial to prove (or disprove). Both observational effects and fundamental questions underly this assumption.

Inflows, outflows, mergers and other dynamical disturbances may bias the line width low *or* high. Slit effects may prohibit the identification of peculiar kinematics. More uncertainties arise due to slit spectroscopy: the kinematic and photometric major axes need not coincide, and the velocity profile is smeared out because the slit and the galaxy are of comparable size. Poor spatial resolution can bias the RC velocity low up to a factor two (Erb et al. 2004). Poor spectral resolution causes smearing in the spectral direction. Poor signal-to-noise, S/N, observations cause a significant uncertainty in the linewidths and RC velocity observed (Moorwood et al. 2003). The combined effect on the measured line widths is uncertain and cannot be quantified with our current data, leaving significant uncertainties in the measured offset from the TFR.

The distribution of the emission line flux over the galaxy also influences the linewidths and RC velocity measurements. Barton & Van Zee (2003) showed that a central (or more general, a local) peak in star formation may bias the linewidth measured low by a factor 2.

A more fundamental question is: do the optical emission lines extend out to the flat part of the RC like they do in the local universe? Although tilted emission lines have been observed out to redshift 3.2 (Moorwood et al. 2003; Pettini et al. 2001), no flat RCs have been observed above redshift ~ 1 (Moorwood et al. 2003; Pettini et al. 2001; Lemoine-Busserolle et al. 2003; van Dokkum & Stanford 2001; Erb et al. 2003,

2004). A large sample of $z > 1$, high S/N, high spectral resolution and excellent seeing observations may show these disks do exist at these redshifts, but it may also be the case that star forming disks have undergone significant evolution since $z \sim 1$ and do not extend to the flat part of the RC. Pérez (2004) recently reported evidence for stellar disk truncation in the redshift range $0.6 < z < 1.0$.

Kannappan et al. (2005) investigated the importance of various effects on the offset from the local TFR of two high redshift TFR studies ($z \sim 0.34$ and ~ 0.52). When all samples are converted to the same cosmology and reference sample, the largest correction factor is that of rotation curve truncation (0.71 magnitude using their cosmology and reference sample). Their samples used RCs only, the situation for linewidths might be different, nonetheless this should be a major warning that our velocity measurements cause a large uncertainty in our analysis.

2.6.4 Rest frame magnitude

TFRs can be measured in all optical and near infrared bands. The scatter in the TFR decreases with longer wavelength because of decreased sensitivity to dust and star formation (e.g. Verheijen 2001). Our choice for rest frame B and R band was forced by the available photometry. Spitzer will open the window to rest frame K band photometry.

2.6.5 Local comparison sample

One can only measure a luminosity offset with respect to a reference sample. The galaxies in the reference sample may be and probably will be different from the high redshift galaxies in many respects. They may have different SFRs and star formation histories (SFH), higher ages, different metallicities and dust properties, different emission line fluxes and EWs, more or less or other kinematic disturbances, lower gas mass fractions, and more. All these factors contribute directly or indirectly to the position of the galaxies in the TF plot and the luminosity offset measured. Careful definition of the reference sample is crucial for the interpretation for the results. In our case, we choose to take the Verheijen (2001) sample as a reference sample. This sample contains only 'very ordinary' cluster spirals. Strictly speaking, we have measured the offset of young star forming galaxies from the 'most ordinary local spirals' TFR. We will show now that our conclusions do not change if we choose an other reference sample.

A local starburst sample might be an obvious choice for a reference sample. Several local starburst samples for TFR applications are available and they follow the normal local TFR, with outliers and increased scatter mainly at the low mass end (Mendes de Oliviera et al. 2003; Barton et al. 2001; Van Driel, Van den Broek & Baan 1995; Brungardt 1998; Davoust & Contini 2004). The effects of star formation on the TFR become apparent at $\log(W_{20}) \lesssim 2.4$. When studying high mass galaxies (like we do), taking a starburst TFR does not make a difference for the measured luminosity offsets. We discuss the effects of star formation on the TFR extensively in subsection 2.6.7.

We might also choose a sample containing all local spirals, following Kannappan et al. (2005) who used a morphology blind sample of bright emission line galaxies brighter than $M_B = -18$ and inclined more than 40 degrees. This kind of TFR generally has a shallower slope than other TFRs, because of the larger effect (see subsection 2.6.7)
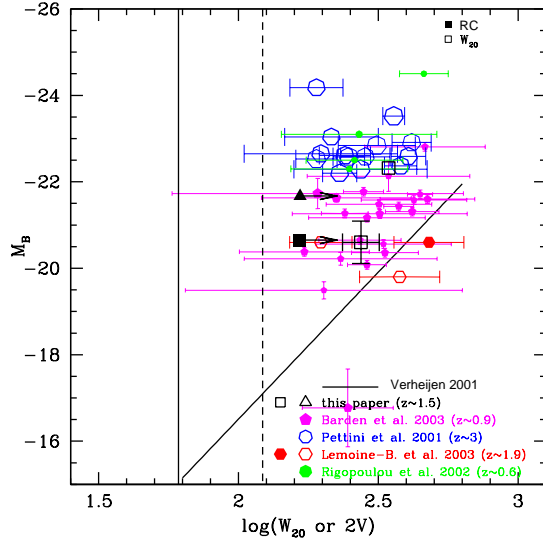
Figure 2.6 — Selection in velocity for the high redshift TFR. Plotted are the local TFR of Verheijen (2001), the data points presented here (using the same symbols as in Fig. 2.4) and data from various other authors whose data were also (partially) obtained with ISAAC. Filled symbols are RC velocities, open symbols linewidths and point size increases with redshift. The vertical lines are once (thick line) and twice (dashed line) the ISAAC velocity resolution (1 $''$slit MR mode) for Hα at redshift 1.5.

of a starburst on lower mass galaxies. The approach also has it pitfalls, as the high redshift sample does not contain 'all' high redshift galaxies, and depending on the high redshift sample, the amount of luminosity evolution may appear different. Using this TFR to measure the offset from the local TFR at $\log(W) = \log(2V) = 2.5$ reduces the measured offset by 0.2 mag (Kannappan et al. relation) plus 0.15 mag (to account for the different value used for H_0) = 0.35 mag.

Our sample is selected on EW(Hα) and F(Hα), a local sample selected on these properties could also serve a reference sample. Unfortunately, there is no such sample available.

We conclude that the differences between local TFRs for different samples of galaxies are important for the low mass end of the TFR. The differences for high mass end of the TFR are negligible compared to the other uncertainties in the analysis.

2.6.6 Selection effects

Selection effects play an important role in high redshift TFR studies. We will now discuss selection in velocity, selection in magnitude, and selection in equivalent width. The latter is specific for our sample.

In Fig. 2.6, we plot once and twice the for formal slit limits for ISAAC velocity resolution (1 $''$ slit, MR mode R $\sim$ 3000) for Hα at redshift 1.5. These limits vary very little between redshift 1 and 2.5 for Hα measurements with ISAAC. These limits are upper limits to the actual resolution because seeing is the limiting factor. It is immediately evident why measuring TF slopes is so difficult at high z: the range in velocity is small compared with local samples, where velocity resolution limits only play a role in samples of dwarfs. Therefore, we did not attempt to measure a 'relation' but only an offset from the local TFR at $W_{20} \sim 320$ km s^{-1} corresponding to $\log(W_{20}[\text{km s}^{-1}]) \sim 2.5$.

It becomes increasingly difficult to measure TFR parameters for galaxies of a certain luminosity with increasing redshift, pushing one again to larger mass (and hence brighter) galaxies. There is no clear absolute magnitude cut in the NICMOS grism sam-

ple, it is biased against low equivalent width emission lines (see below). Moreover, the redshift range is quite large and the depth of the observations varies from field to field. To give an impression of a typical luminosity limit, the magnitude limit for the lowest luminosity object in our sample (in the total NICMOS grism sample there are a few slightly fainter objects) at redshift 1.5 would be -20.4 in B. At the velocities observed, we cannot distinguish between a zero point offset or increased scatter in the TFR in magnitude limited samples.

The main selection effect in the NICMOS grism sample is a bias against emission lines with low equivalent width. A selection effect on EW cannot be translated to a simple straight line in the TF plot, like the selection effect on velocity and magnitude. However, the selection effect on EW could be very important. Kannappan et al. (2002) showed that in the local universe EW(Hα) correlates with offset from the TFR, with large EW(Hα) galaxies being up to 2 mag brighter in R than expected from the local TFR although with considerable scatter. Kannappan & Barton (2004) showed a similar result for the B band residuals. However, there are three reasons why these results should not be simply copied to our galaxies.

First, the galaxies in those samples have rest frame EW(Hα) $\lesssim$ 60 Å, and most have EW$\sim$ 20 Å. The rest frame EW(Hα) of our sample of galaxies ranges from 161 to 310 Å (detections only, and excluding the Seyfert 1) (numbers from McCarthy et al. 1999), i.e. an order of magnitude larger. A local sample of galaxies with comparable EW(Hα) and L(Hα) line strengths is unavailable due to the rarity of these galaxies in the nearby universe (James et al. 2004; Gallego et al. 1997). Based on the EW(Hα) alone, we might expect the NICMOS galaxies to be brighter than the not EW selected $z \sim 1.5$ TFR although the amount of brightening remains uncertain.

Second, Kannappan et al. (2002) and Kannappan & Barton (2004) also showed that B-R color correlates with residuals from the B and R band TFR, with the residuals being about $\sim$0.5 mag at the estimated B-R color for the NICMOS galaxies. This amount of brightening is significantly less than expected from the EW(Hα), indicating again we are looking at an 'incomparable sample'.

Third, the systematic offset from the TFR correlating with EW(Hα) and B-R color as found Kannappan & Barton (2004) mainly comes from galaxies with log(W[km s^{-1}]) $\lesssim$ 2.4 (their definition of line width W is different from ours, but the differences between different definitions of W are minor). The galaxies in Kannappan et al. (2002) cannot easily be traced through their diagrams. EW(Hα) may be important for low mass galaxies, but irrelevant for high mass galaxies, and hence the NICMOS galaxies.

We therefore conclude that although the selection of high EW galaxies most likely biases our result, the effect cannot be quantified by a comparison to local samples. We therefore take a different approach in the next section.

2.6.7 The effect of a starburst on luminosity in the TF plot

The study of the high redshift TFR is limited to galaxies with a sufficient SFR to detect and resolve emission lines like Hα, [O III]5007/4959 and [O II]3727. These galaxies may not be representative (from a TFR point of view) for galaxies with smaller SFR. Star formation may affect the position of a galaxy in the TF plot in both luminosity and velocity. The effects on velocity were discussed in Sect. 2.6.3. A starburst increases the
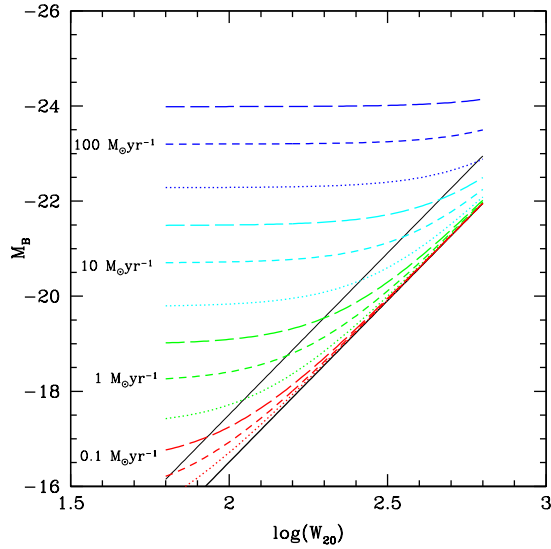
Figure 2.7 — The luminosity of starbursts of different SFRs (indicated in the plot) and different durations (10^7, 10^8 and 10^9 yr for the dotted, dashed and long dashed lines respectively) added to the local Verheijen (2001) TFR (thick line). The thin line indicates one mag brightening.

luminosity of a galaxy, and one might worry that the use of only starburst galaxies will mimic luminosity evolution in the TFR. We will now show that the increase in log(L) (the parameter in the TF plot) is negligible for massive galaxies assuming they have a significant older population, which - as we will show below - might not be the case for some of the NICMOS galaxies.

We already discussed a hint that star formation could be important in Sect. 2.6.6, namely the results of Kannappan et al. (2002, 2005) and Kannappan & Barton (2004). These papers showed that offsets from the U, B and R band TFR correlate with the star formation indicators B-R color and global EW(Hα), bluer color and larger EW (hence more actively star forming) galaxies being overluminous for their RC velocity. We also noted that different parameters gave conflicting results for our sample, and outliers mainly occur at the low mass end of the TFR. On the other hand, there was also a hint that star formation may not be important for TFR studies. As we saw in Sect. 2.6.5, local starburst TFR follow the local normal spiral TFR, with some outliers at the low mass end. We will now try to explain these observations using a simple model.

We plot in Fig. 2.7 the effect on luminosity of local galaxies for different starbursts (different SFRs, different duration of the starburst) calculated using models from Bruzual & Charlot (2003, (BC)) (Padova 1994 models, Cabrier IMF, solar metallicity). We added only the luminosity of the starburst, and neglected the effect of the additional mass on the RC velocity. As can be seen in this figure, the luminosity of low mass galaxies is dominated by even modest amounts of additional star formation. For galaxies with log(W_{20}) $\gtrsim$ 2.4 only strong starbursts have a significant effect on log(L). This is the W_{20} value where the BC model (see Fig. 2.7) for a short (10^7 yr) 10 M$_\odot$ yr^{-1} starburst lies 1 mag above the (local) TFR. This figure immediately explains why outliers are often low mass galaxies and why the zero point of the TFR at the high mass end is so stable.

High redshift galaxies have a younger and less massive population compared with local galaxies. The net effect on luminosity using BC models with an exponentially decreasing SFR is an increase in L_B for high redshift galaxies. Additional starforma-

tion will therefore have a smaller effect on the luminosities of high redshift galaxies compared to local galaxies.

We conclude that provided the older stellar population is sufficiently luminous and the measured velocity represents the mass of the galaxy, a starburst will not change the position of a galaxy in the TF plot and starburst galaxies are (from a TFR point of view) representative for the total galaxy population.

We will now attempt to check if the NICMOS galaxies fulfill these criteria and are therefore TFR-representative for the entire $z \sim 1.5$ spiral galaxy population. The linewidths indicate that the NICMOS galaxies are sufficiently massive for TFR studies: their linewidths (without inclination correction) are $\log(W) \gtrsim 2.4$. The non-detection of rotation curves can be explained by poor seeing. Improving the velocity measurements remains the biggest challenge for all high redshift Tully-Fisher studies.

For the case of the NICMOS galaxies, the luminosity of the older population is hard to constrain. The SFRs indicate we cannot assume the starburst luminosity to be negligible. The large EWs indicate the importance of a young stellar population. We used the starburst99 models (Leitherer et al. 1999) to estimate the age of the galaxies. Assuming constant star formation and a Salpeter IMF with mass range $1 - 100 M_\odot$, the EW indicate that the age of the galaxies is $\lesssim 1$ Gyr. This result strongly depends on the initial mass function and star formation history. A younger starburst could also produce the large EW, while contributing less to the total luminosity. Without additional data, we cannot calculate a reliable estimate of the starburst luminosity, and we cannot answer the question whether this sample is TFR-representative for the entire $z \sim 1.5$ spiral galaxy population. Note that this conclusion is specific for this sample and not for other samples at similar redshift. The EWs of this sample are extreme, and we have no photometric data that could provide constraints on the SFH.

2.7   Summary and conclusion

We studied the challenges in measuring $z > 1$ TFR using emission line galaxies using a sample of Hα emitting galaxies. We conclude:

   - We confirm only 5 out of 9 emission lines found by McCarthy et al. (1999). Of the 5 remaining sources, one is a broad line AGN, one probably a narrow line AGN. Our conclusions are therefore based one a very small number of sources.

   - Without reliable inclinations and extinctions, an ensemble averaged simultaneous inclination and extinction correction can be made assuming the relation between extinction and inclination follows that of local galaxies, which is in general a small correction because galaxies move approximately along the TFR.

   - The most difficult challenge for high redshift TFR studies, are the velocity measurements. Besides the observational challenges and limitations, there is also the fundamental question if what we observe is comparable to what we observe in the local galaxies (for example the question if the emission lines extent to the flat part of the RC). For the current data set, this leaves considerably uncertainties in the measured line widths, which cannot be quantified.

   - The high mass end of the local TFR is not sensitive to the sample used, therefore the choice of the local reference sample is not important for the high mass end of the

high redshift TFR.

- Extending the study of the high redshift TFR to low mass galaxies will be very difficult due to the selection effects in velocity and magnitude: it would require very high spectral resolution observations of very faint galaxies.

- Star formation increases the luminosity of galaxies, but the effect on $\log(L)$ is negligible for high mass galaxies with significant older population. Therefore star forming galaxies can be TFR-representative for all galaxies, and whether they are or not can be checked.

For the NICMOS galaxies, we measured a ~ 2 mag offset of the $z \sim 1.5$ rest frame B starburst TFR with respect to the local TFR. This offset is robust against the effects of inclination and extinction. The linewidths indicate sufficiently massive galaxies for TFR studies, the results is therefore also robust for the choice of local comparison sample. However, we cannot prove or disprove that all linewidths are due to rotation. Moreover, we cannot answer the question if the star burst luminosity dominates the total luminosity or not. This is due to the extreme nature of the galaxies and the sparseness of data for this sample.

Acknowledgements

References

Baker, A.J., Tacconi, L.J., Genzel, R., Lutz, D. & Lehnert, M.D. 2004 ApJ 604 125 140
Baker, A.J., Tacconi, L.J., Genzel, R., Lutz, D. & Lehnert, M.D. 2004 ApJ 613 L113
Barden, M. 2003 astro-ph 0308272
Barton, E.J., Geller, M.J., Bromley, B.C., van Zee, L., & Kenyon, S.J. 2001 AJ 121 625
Barton Gillespie, E. & van Zee, L. 2003, The Mass of Galaxies at Low and High Redshift. In Proceedings
        of the ESO Workshop held in Venice, Italy, 24-26 October 2001, p. 226
Bell, E.F. & De Jong, R.S., 2001, ApJ 550 212
Brinchmann, J., Charlot, S., White, S.D.M. et al. 2004, MNRAS 251 1151
Brungardt, C.L. 1988 ApJ 327 L51
Bruzual, G. & Charlot, S. 2003, MNRAS , 334 1000 1028
Courteau, S. 1997, AJ 114 2402
Davoust, E. & Contini, T., 2004 A&A 416 515
Denicoló, G., Terlevich, R. & Terlevich, E. 2002 MNRAS 330 69 74
Devillard, "The eclipse software', The messenger No 87 - March 1997
Erb, D.K., Shapley, A.E., Steidel, C.C. et al. 2003 ApJ 591 101
Erb, D.K. Steidel, C.C., Shapley, A.E., Pettini, M., Adelberger, K.L. 2004 ApJ 612 122
Förster-Schreiber, N. et al. 2005 in prep.
Gallego, J. Zamorano, J. Rego, M. & Vitores, A.G. 1997, ApJ 475 502 511
Hainline, L.J. Scoville, N.Z., Yun, M.S. et al. 2004 ApJ 609 61
Hicks, E.K.S. Malkan, M.A.; Teplitz, H.I.; McCarthy, P.J. & Yan, L. 2002, ApJ 581 205
James, P.A., Shane, N.S., Beckman, J.E. et al. 2004 A&A 414 23
Kannappan, S.J. & Barton, E.J., 2004, AJ 127 2694
Kannappan, S.J., Fabricant, D.G. & M. Franx 2002, AJ 123 2358
Kannappan, S.J., Fabricant, D.G. & M. Franx in prep. draft Kannappan's website.
Kennicutt, R.C. 1998, ApJ 435 22
Leitherer, C., Schaerer, D., Goldader, J.D. et al. 1999, ApJ 123 3
Lemoine-Busserolle, M., Contini, T., Pelló, R. et al. A&A 397 839

McCarthy, P.J., Yan, L., Freudling, W. et al. 1999, ApJ 520 548

McGaugh, S.S., Schombert, J. M., Bothun, G. D. & de Blok, W. J. G. 2000, ApJ 533 99

Mendes de Oliveira, C., Amram, P., Plana, H., & Balkowski, C. 2003 AJ 126 2635

Moorwood, A., van der Werf, P., Cuby, J.G. & Oliva, T. 2003 Rotation and Masses of Galaxies at z ∼ 3.2 in 'The mass of galaxies at low and high redshift' eds. R. Bender & A. Renzini Springer, Berlin, p. 256

Pérez, I. 2004 A&A 427 L17 L20

Pettini, M. Shapley, A.E., Steidel, C.C. et al. 2001, ApJ 554 981

Pisano, D.J., Kobulnicky, H.A., Guzmn, R., Gallego, J. & Bershady, M.A. 2001, AJ 122 1194

Rigopoulou, D., Franceschini, A., Aussel, H. et al. 2002, ApJ 580 789

Rix, H-W., Guhathakurta, P., Colless, M. & Ing, K. 1997, MNRAS 285 779

Stil, J.M. & Israel, F.P. 1998, astro-ph 9810151

Tully, R. B. & Fisher, J.R. 1977, A&A 54 661

Tully, R. B. & Pierce, M.J., 2000, ApJ 533 744

Tully, R. B., Pierce, M.J., Huang, J-S. et al. 1998, AJ 115 2264 2272

Van den Bosch, F.C. 2002, MNRAS 332 456

Van Dokkum, P.G. & Stanford, S.A. 2001 ApJ 562 35

Van Driel, W., van den Broek, A.C., & van Baan, W.A., 1995, ApJ 444 80

Verheijen, M. A. W., 2001, ApJ 563 694

Zwaan, M.A., van Dokkum, P.G. & Verheijen, M.A.W. 2001 Science 293 1800

Chapter 3

Dynamical properties of a large young disk galaxy at z=2.03

Context The study of high redshift Tully-Fisher relations (TFRs) is limited by the use of long slit spectrographs, rest frame B band and star formation selected galaxies.

Aims We try to circumvent these issues by using integral field spectroscopy (SINFONI), by studying the rest frame K band and stellar mass TFR, and by selecting targets without a bias to strongly star forming galaxies. In this paper, we demonstrate our methods on our best case. This galaxy, F257, at $z = 2.03$, was selected from a sample of candidate high redshift large disk galaxies in the Hubble Deep Field South that were selected with photometric and morphological criteria.

Methods We used SINFONI at the VLT to obtain an integral field spectrum of the Hα line and hence a velocity field and rotation curve. We also use UBVIJHK+IRAC band photometry to determine a stellar photometric mass.

Results We find that F257 is indistinguishable from local late type galaxies in many respects: it has a regular velocity field, increasing velocity dispersion towards its center, its rotation curve flattens at 1-2 disk scale lengths, it has the same specific angular momentum as local disks, its properties are consistent with the local K band TFR. Although mainly rotationally supported, its gas component is dynamically heated with respect to local galaxies ($V/\sigma_z \sim 4$) and it is offset from the local stellar mass TFR at the 2σ level. But, this offset depends on the SED modeling parameters. In particular, for a 2-component star formation history (SFH), F257 is in agreement with the local stellar mass TFR. F257 is then a nearly ($\sim 75\%$) maximum disk. The dynamical properties of F257 are more like those of local galaxies than those of any other galaxy at similar redshift observed to date. However, the gas-to-stellar mass ratio is unusually large: 2.5.

L. van Starkenburg, P. P. van der Werf, M. Franx, I. Labbé, G. Rudnick & S. Wuyts

3.1 Introduction

Starting with density fluctuations in the early universe, dark matter halos grow through gravity. Galaxy formation is described by semi-analytical models or hydrodynamical simulations. These may include physical processes such as gas cooling, star formation, feedback from stellar winds, supernovae and/or AGN, chemical evolution and stellar populations (Okamoto 2007 and references therein).

The disk formation epoch in earlier generations of models is relatively late and mostly at $z \lesssim 1$. These early models also predicted that these disks are much smaller than observed in local spiral galaxies and that their specific angular momenta are only 20% of that of their halo's (Navarro, Frenk & White 1995). More recent models produce more realistic size disks (Mo et al. 1998, Portinari & Sommer-Larsen 2007, Governato et al. 2007) and place the formation epoch somewhat earlier: $0.4 < z < 2.0$ (Buchalter, Jimenez & Kamionkowski 2001). Reproducing the specific angular momentum of local disk galaxies remains a challenge (e.g. Portinari & Sommer-Larsen 2007).

More than 30 years after the first publication of what is now known as the Tully-Fisher relation (TFR) (Tully & Fisher 1997), the origin of the TFR is still subject of debate. Some authors explain the TFR as a consequence of self-regulated star formation in disks with different masses (e.g. Silk 1997). In other models, the TFR is a direct consequence of the cosmological equivalence between mass and circular velocity resulting from the finite age of the universe which imposes a maximum radius from with matter can accrete to form a disk (e.g. Mo et al. 1998, Steinmetz & Navarro 1999). Steinmetz & Navarro (1999) show that although the slope of the TFR can be naturally explained by hierarchical models, the normalization and evolution of the TFR depend strongly on the star formation prescriptions and the cosmological parameters. Recently, Courteau et al. (2007) showed that two long known, different theoretical predictions for two different slopes of the TFR are in fact related.

Disk galaxy scaling relations, like the TFR, put strong constraints on galaxy formation scenarios, and in particular on the connection of the dark and baryonic component (van den Bosch 2000). The zero-point of the TFR constrains the SFH and the cosmological parameters that control the universal baryon fraction and the time of assembly of galaxies of different mass (Steinmetz & Navarro 1999). Many authors struggle to reproduce the zero-point of the TFR (e.g. Portinari & Sommer-Larsen 2007, Steinmetz & Navarro 1999). The slope of the TFR and the steepening of the slope towards longer wavelengths can only be explained by supernova feedback (van den Bosch 2000) although others claim it is a natural result of the hierarchical models (Steinmetz & Navarro 1999). The small scatter in the TFR is explained by scatter in halo spin parameters and formation redshifts (e.g. van den Bosch 2000). Even the most recent galaxy formation and evolution models are not able to simultaneously reproduce for example the slope, zero-point and scatter of the TFR and the zero-point and shape of the luminosity function (e.g. Courteau et al. 2007 and references therein).

The TFR defines a tight correlation between the luminosity and the flat rotation curve velocity of spiral galaxies. If luminosity is converted into stellar mass (which requires detailed modelling of the stellar spectral energy distribution (SED)), the tight correlation remains: the stellar mass TFR. Semi-analytic models predict evolution in

the slope, zero-point and scatter properties of the TFR and the stellar mass TFR (e.g. Steinmetz & Navarro 1999, Buchalter, Jimenez & Kamionkowski 2001, Portinari & Sommer-Larsen 2007). A key element is the relative evolution of the dark and stellar mass components, which is a direct test of the stellar mass buildup within a dark halo of a given mass.

Critical tests of these theories can be made by observing the evolution of disks backward in time. Rotation curves (RCs) of field galaxies out to $z = 1$ measured with the Keck telescope and Very Large Telescope (VLT) are found to be similar to those of nearby galaxies in both shape and amplitude implying that some massive disks were already in place at $z \sim 1$ (Vogt et al. 1996, 1997, Barden et al. 2003, Swinbank et al. 2006). Observations of $z \sim 2$ galaxies have revealed ordered rotation, but only the rising part of the rotation curve (e.g. the lensed sources of Lemoine-Busserolle et al. 2003). Van Starkenburg et al. (2006) found ordered rotation in a $z = 2.46$ galaxy, with an asymmetric line profile indicating a central starburst and weaker starformation in the outer parts. Ordered rotation has been found out to $z \sim 3.2$ by Moorwood et al. (2000, 2003) and by Nesvadba et al. (2006), the latter again on a lensed source.

Also, several attempts to measure size evolution and the TFR at redshift $0.5 - 1.5$ have been made over the past few years with contradictory claims about disk evolution. For instance, Mo et al. (1998) used previously acquired data (Vogt et al.1996, 1997; Schade et al. 1996; Lilly et al. 1998) to conclude that $z \sim 1$ galaxies are smaller than local galaxies at a fixed rest-frame B-magnitude or rotation velocity, consistent with hierarchical models. A brightening with redshift of disk galaxies at fixed rotation speeds was also detected by Barden et al. (2003). However, Simard et al. (1999) and Ziegler et al. (2002) have shown that massive galaxies at $z < 1$ are consistent with having no evolution in surface brightness, once selection effects are taken into account.

The largest source of uncertainty in those studies, all done with long slit spectra, are the velocity measurements. In recent years, it has become possible to do integral field spectroscopy at near infrared wavelengths, for example with SINFONI at the VLT (Eisenhauer et al. 2003, Bonnet et al. 2004). Integral field spectroscopy has significant advantages over long slit spectroscopy. First, long slit measurements may suffer from slit misalignment. More fundamentally, the photometric and kinematic axes may be different (due to star forming regions or intrinsic shape of galaxy). Kinematic disturbances are harder or impossible to identify in slit spectra. Integral field spectroscopy does not have all these slit related problems. Finally, integral field spectroscopy makes for a fairer comparison with low-z Tully-Fisher data, which are typically derived from full imaging of the HI velocity field with radio aperture synthesis. Integral field spectroscopy thus presents a major improvement over slit spectroscopy, provided significant resolution over the rotating disk is achieved. Recently, Förster Schreiber et al. (2006b) and Bouché et al. (2007) used SINFONI to obtain two-dimensional velocity fields of a number of galaxies at $z \sim 2$ with different selection criteria, clearly demonstrating the power of an efficient integral-field spectrograph such as SINFONI for this type of work.

A second major problem that plagued previous high-z TFR studies is the use of restframe B-band, which is very sensitive to small amounts of recent star formation and extinction by dust. There are now a number of deep surveys available with compre-

hensive photometric coverage ideal for studying the high redshift TFR in rest frame near-IR luminosities. We used the HDF-S and MS1054 fields which includes recent Spitzer IRAC data (Labbé et al. 2005). This allows us to use rest-frame near-IR luminosities, which define much tighter TFRs than rest-frame optical luminosities (e.g. Verheijen 2001). Rest-frame K band luminosities as derived from Spitzer data are much less sensitive to the effects of dust and recent starformation than rest frame optical or UV luminosities and will provide us with more accurate stellar masses.

A third limitation of previous studies is that many of these target starformation-selected galaxies (e.g., selected on rest-frame UV or bright emission lines). This compromises attempts to use these galaxies to trace the evolution of the TFR (see van Starkenburg et al. 1996 for a detailed discussion), since local TFR samples are composed of relatively quiescent galaxies. Although a certain amount of star formation is necessary to observe the velocity fields of high redshift galaxies, there are several ways to partly circumvent this problem.

First, by selecting from ultra-deep near-IR imaging surveys, such as the FIRES data of the HDF-S and MS1054 fields[1](Labbé et al. 2003b, Franx et al. 2003, Förster-Schreiber et al. 2006a), we can select galaxies in the rest frame optical instead of the rest frame UV. The FIRES data is sufficiently deep to select galaxies in the rest-frame optical out to $z \sim 4$ and the depth on the Hubble Deep Field South (HDF-S) is sufficient to detect non-evolving ($0.6L_*$ at $z = 0$) spirals out to $z = 3$.

A second improvement is to preselect massive galaxies. Contrary to low mass galaxies, their $\log(L)$ (and hence offset from the TFR) is not or less affected by the luminosity of a starburst (van Starkenburg et al. 1996). We observed several targets in this category in two redshift ranges, which will be discussed in two separate papers (van Starkenburg et al. 2008a, 2008b).

Finally, it is now possible to select high redshift galaxies that morphologically resemble local disks. A search for such disks in the FIRE survey of the 2.5 x 2.5 HDF-S field resulted in a surprisingly large number (6) of candidate large disks (Labbé et al. 2003a). These galaxies, at redshifts 1.4 to 3.0 (most of them spectroscopically confirmed), have exponential profiles with effective radii ranging from 0.65 to 0.9 (or $5.0 - 7.5h_{70}^{-1}$ kpc) and extending over 2-3 effective radii and appear remarkably regular in the near infrared (rest frame optical). Four are well fit by just exponential disks and two require an additional $r^{1/4}$ bulge component, contributing about 40% of the light. At shorter wavelengths, they have more extended and irregular morphologies. They have strong rest-frame optical breaks in their centres and evidence for intense star formation in the outer parts, reminiscent of local spirals, with blue star-forming disks and red bulges. Their sizes are comparable to the Milky Way and those of L* disks in the local universe. Specifically, these sizes are much larger than those of typical LBGs ($1 - 2h_{70}^{-1}$ kpc; Giavalisco et al. 1996; Lowenthal et al. 1997) and their sizes are in the upper end of the range found by Trujillo et al. (2006) for all galaxies at similar z in the two FIRES fields. They are bright in K (K= $19.7 - 21.1$) and have large stellar masses ($M > 10^{11}$ M$_\odot$). They constitute half of the most rest-frame luminous galaxies ($L_V > 6 \times 10^{10}h_{70}^{-2}L_\odot$) and their number density exceeds model predictions (e.g., Mo et

---

[1]The FIRES data are publicly available, see http://www.strw.leidenuniv.nl/~fires
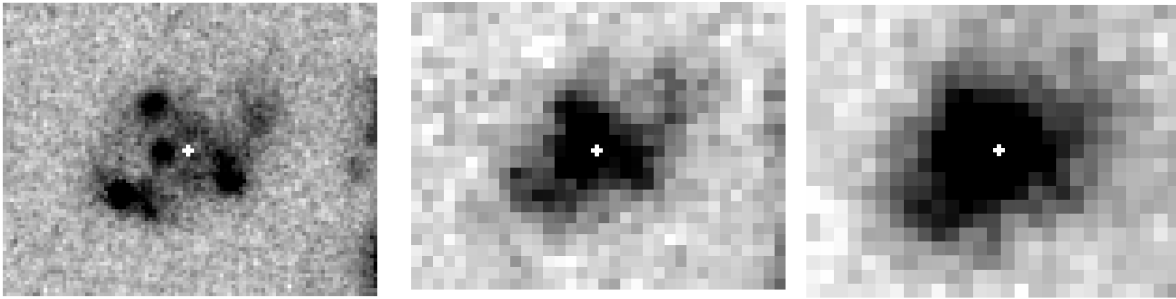
Figure 3.1 — From left to right: F814W image, NICMOS H band image and Ks image from FIRES data. Image size is always $3''$ times $4''$ and the images have been rotated so that east is to the top and north is to the right. The (K band) center from the FIRES data is marked by the white crosses.

al., 1998) by a factor of two. Obviously, the first and foremost question that needs to be resolved is whether these objects are truly rotationally supported disks, and this can only be tested by obtaining kinematic data.

In this paper, we present SINFONI observations[2] of one of the large disks of the Labbé et al. sample (id 257 in the FIRES HDF-S catalog). These observations were part of a larger project of SINFONI observations of mass and/or disk selected high redshift galaxies, which will be presented in two separate papers (van Starkenburg et al. 2008a, 2008b). Here, we will discuss our methods as used on our best case.

We observed F257 with SINFONI during the night of August 15, 2006. We selected F257 as our primary target for this observing run because it is the second brightest K band source ($K = 20.25$) of the large disks in the HDF-S (Labbé et al. 2003a) that has a known spectroscopic redshift ($z = 2.03$, Vanzella et al. 2002) with Hα at an observable wavelength with SINFONI. (We had observed the brightest K band target full-filling this criteria during an earlier observing run, see van Starkenburg et al. 2008b). Its effective radius is $0''.74$ in K band, the total radial extent above the K-band detection threshold is two effective radii or 3-3.5 scale lengths ($R_d = 0''.44$). The inclination ($\sim 54°$, calculated from the ellipticity of Labbé et al. 2003a) is suited for a velocity field analysis. F257 shows a clumpy distribution in the HST F814W filter (see Fig. 3.1a) which corresponds to rest frame UV. The rest frame optical (observed K band) image shows a smooth exponential profile (see Fig. 3.1c). This difference cannot be attributed to the different PSF of the F814W and the K band image: the F814W image smoothed to the K band PSF still shows the clumps. Labbé et al. (2003a) fitted an exponential profile without the need for a bulge component. NICMOS H band shows an intermediate picture (see Fig. 3.1b). The Sérsic index as determined by Trujillo et al. (2006) on the FIRES (ISAAC) H band image is 0.76. Wuyts et al. (2007) made an extensive study of the SEDs of high redshift galaxies in HDF-S and found for F257 $M_* = 3.5^{+0.5}_{-0.3} \times 10^{10}$ M$_\odot$, a mass weighted age of ~ 160 Myr and $A_V = 1.0$ using a Salpeter initial mass function (IMF), solar metallicity, a τ 300 model for the star formation history (SFH) and Bruzual & Charlot (2003) models. A number of $z \sim 2$ galaxies have been observed with SIN-

---

[2]Observations carried out using the Very Large Telescope at the ESO Paranal Observatory, Program ID 077.B-0079.

FONI and other IFUs (Genzel et al. 2006, Förster-Schreiber et al. 2006b, Bouché et al. 2007, Law et al. 2007). F257 is not different in terms of colors, SFR or age, and satisfies the conventional U-dropout criterium. It is the only galaxy selected as large disk galaxy, but the other galaxies were selected from catalogs with insufficient resolution to identify morphological large disk galaxies at optical rest frame wavelengths.

Throughout this paper, we use $H_0 = 70 \text{ km s}^{-1}\text{Mpc}^{-1}$, $\Omega_M = 0.3$, $\Omega_\Lambda = 0.7$ and Vega magnitudes.

3.2 Observing strategy

SINFONI (Eisenhauer et al. 2003, Bonnet et al. 2004) is the near infrared integral field spectrograph of the VLT. SINFONI slices a square image into 32 slitlets that are combined into a single pseudo slit and then dispersed. It operates in J, H, K and H+K band and offers three image sizes. We used the 8 x 8″ field of view (FOV) in K band. The spectral resolution in this mode is $R \sim 4500$ or FWHM $\sim 75 \text{ km s}^{-1}$.

We used an ABA'B'-like observing cycle, comparable to the ABBA-cycles used in near-IR long slit spectroscopy. Placing our targets at different positions in the FOV instead of taking sky frames ensures optimal use of observing time. Because there is a pair of galaxies close to F257, the last two offset positions are only slightly offset from the first two positions. We rotated SINFONI's FOV so that the other galaxies do not interfere with the observations of F257 (see Appendix A for details on SINFONI's FOV). Individual exposures were 900 s, total on source integration time 6 hours. We used 900 s exposures to keep the extra overheads (observations of PSF stars, see details in Appendix A) within reasonable limits. As our target is too faint to acquire directly, we performed a blind offset from a bright nearby star to our target. The seeing varied during the night between 0″.35 and 0″.86 (measured on the PSF stars). The seeing on the weighted combined cube is 0″.55. We also observed four hot standard stars for flux calibration during the entire night (which also included observation of another target).

3.3 Data reduction

We used a combination of IRAF tools and the SINFONI pipeline (version 1.3.0) (Modigliani et al. 2007) for data reduction. We reduced the standard calibration files provided by ESO for SINFONI (dark, distortion, flat, linearity, and arc frames) using the SINFONI pipeline to get bad pixel maps, darks, flats, wavelength calibration map, the positions of the slitlets on the detector and distortion correction.

We removed bad pixels from the science images and used LA_COSMIC (van Dokkum 2001) to remove cosmic rays. Some cosmic rays close to bright OH lines remained, we removed those close to the Hα line manually by replacing those pixels with the interpolated value of the surrounding pixels. We noticed an odd-even effect in some slitlets, with strength varying with time and in different quarters of the detector, sometimes absent. Therefore, we averaged all columns with the mean of their right and left neighbour to remove the odd-even effect. This causes a small (5% increase in the FWHM of the final PSF) smear in the x-direction after image reconstruction (see Appendix A for definition of x and y direction on SINFONI's FOV).

We used the SINFONI pipeline to correct our data for distortion, flat fielding, reconstructing the data cube, and combining our science data in pairs ("first subtraction") and did exactly the same for the PSF stars. We did an illumination correction on the science data using an early version of the recipe made by Juha Reunanen. We checked the combined cubes for faint star-like persistence effects (see van Starkenburg et al. 2008a) but there were none.

We measured the position and FWHM of the PSF stars at the wavelength range (averaged over 40 pixels) of the Hα and [N II]λ6583 line. We used these positions to combine the data in pairs ("second subtraction") for reasons described in Appendix A. The last two science frames were observed at the end of the night. There was no time left to observe PSF stars for these frames. We used the positions of the previous observation block (OB) for this pair (which will get very low weight in the final combination anyway because the seeing was poor).

Then, we flux calibrated the data using the PSF and standard star data. The flux of the PSF stars correlates well with 1/airmass, and we used this relation to do a relative flux calibration for all pairs of science frames. We also observed four bright standard stars during the night, but those did not show this tight correlation between airmass and flux (after correcting for different integration times and luminosity). Two standard stars gave consistent results (with the PSF star relation), the third differed in the amount of atmospheric absorption, the fourth was more noisy. Fortunately, Hα is not at a relevant wavelength for atmospheric absorption. We choose to use the average of the two consistent standard stars for absolute flux calibration and ignored the other two standard stars.

We used the FWHMs of the PSF stars to weigh the data when combining all data. We found the best result in terms of resolution and signal-to-noise (S/N) when weighting with the square of the FWHM in the y direction (which is unaffected by the complex FOV reconstruction). We measured the seeing in the combined image from the combined PSF star image (using the same weights, at wavelength of Hα and [N II]λ6583) and found 0$\farcs$55. The FWHM in the x direction is 20% larger.

Further details on the reconstruction of the FOV using the PSF stars are provided in Appendix A.

3.4 Results

The final integrated 1D spectrum of F257 is shown in Fig. 3.2 and shows Hα at redshift 2.028 together with [N II]λ6583 ([N II]λ6548 falls on top of a bright OH line). We do not detect the [S II] lines. The continuum is very faint but clearly detected in the median collapsed cube (excluding the wavelength range of the emission lines). The rest frame equivalent width (EW) of Hα is ~ 160 Å where the continuum flux was calculated from a linear interpolation of the observed H and K magnitudes from the FIRES data.

The [N II]/Hα ratio is ~ 0.22 (averaged over the whole galaxy) which is consistent with ionization by star formation. The metallicity calculated from this ratio is $12 + \log(O/H) = 8.6$ which corresponds to slightly subsolar metallicity (Denicolo et al. 2002, solar metallicity is $12 + \log(O/H) = 8.91$). The [N II]/Hα ratio is slightly larger in the centre of the galaxy ([N II]/$H\alpha \sim 0.4$) which gives metallicity $12 + \log(O/H) = 8.8$. The
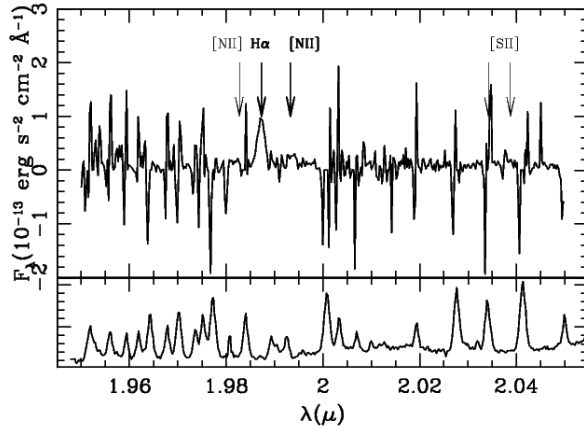
Figure 3.2 — The integrated 1D spectrum of F257. We detect Hα and [N II]λ6583. The positions of the [N II]λ6548 and [S II]λ6717/6731 are also marked in grey. The logarithm of the sky spectrum with OH lines is shown in the bottom panel.
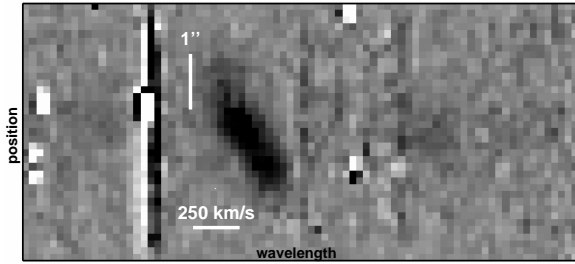

Figure 3.3 — Synthetic long slit spectrum. Scales are indicated in the figure. Note the presence of faint [N II] emission.

[N II]/Hα ratio is also consistent with ionization by star formation in the centre of the galaxy. Ionization by an AGN would would give larger a larger [N II]/Hα ratio.

Using the Kennicutt (1998) relation for a Salpeter IMF, the Hα flux corresponds to a star formation rate (SFR) of 116 $M_\odot yr^{-1}$ uncorrected for extinction. Using $A_V = 1.0$ from Wuyts et al. (2007), the SFR becomes 232 $M_\odot yr^{-1}$. This value is very close to the value found when dividing the best fit mass and age from the SED fitting: 219 $M_\odot yr^{-1}$.

The FWHM of the Hα line is 244 km s^{-1} after correction for instrumental resolution. Again, there is no evidence for the presence of an AGN in the form of broad lines. Stepping through the wavelength slices of the cube, one notices immediately the wavelength shift of Hα. A synthetic long slit spectrum (along the major axis, position angle 32° counterclockwise from the north) made from the cube integrated over the minor axis of the galaxy with slit width 1″25 shows the tilted emission line that flattens at at least one side, see Fig. 3.3. The RC measured from the synthetic long slit spectrum is shown in Fig. 3.4. We will discuss the full velocity field analysis in the next section.

From our final data cube, we extracted line maps of Hα and [N II]λ6583, shown in Fig. 3.5a and 3.5b. The Hα line map shows clumps which resemble the clumps of the F814W image. This is not surprising as both F814W(=rest frame UV) and Hα trace star formation.

The [N II]λ6583 line map shows a much more concentrated distributions, although [N II]λ6583 is detected over the whole galaxy. If the inferred metallicity gradient is also present in the stellar population, this would put the highest metallicity and hence oldest stars in the centre of the galaxy, consistent with the redder color in the centre of the galaxy as found by Labbé et al. (2003a). The [N II]λ6583/Hα line ratio (0.2-0.4) is consistent with star formation over the whole galaxy.

Figure 3.4 — Rotation curve as measured from the synthetic long slit spectrum by fitting a gaussian to each spatial position in Fig. 3.3. The formal fit errors are comparable to the size of the symbols, except for an increase in the outer parts. The points are correlated due to the 0.″55 seeing.
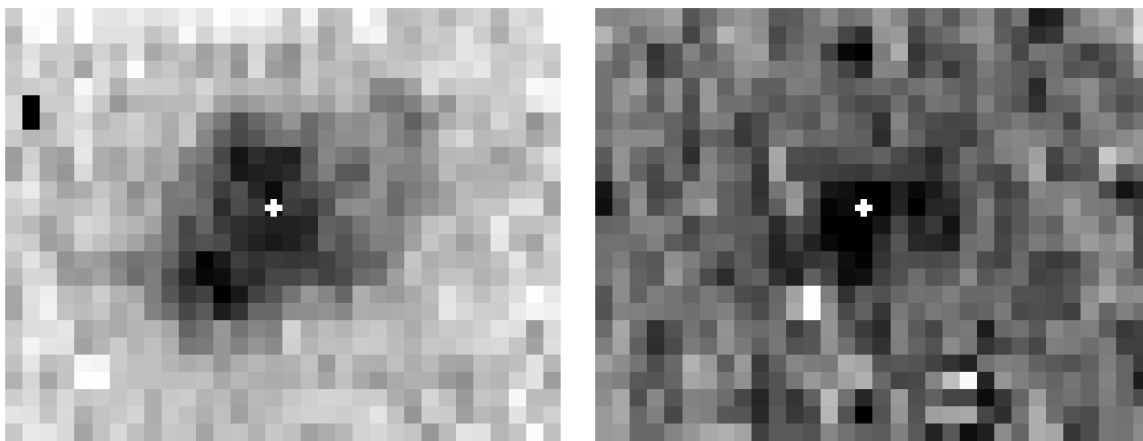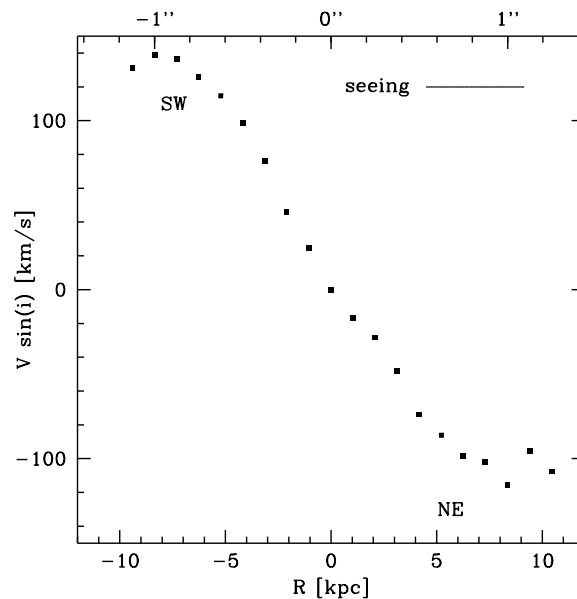
Figure 3.5 — a. Hα line map. b. [N II]λ6583 line map. Image size is again 3″ times 4″ and the images have been rotated so that east is to the top and north is to the right. The white crosses mark again the (K band) center (here determined from the PSF star positions).

3.5 Velocity field

We fitted a Gaussian to the Hα line at every position in the cube. We did this by hand using IRAF's splot because the S/N ratio of individual spectra is low and nearby OH line residuals confuse automatic fitting routines. For the outer parts of the galaxy, we were able to get a few additional data points by adding the spectra of 4 pixels (which were used as one pixel in the modeling). The resulting velocity field is shown in Fig. 3.6a on page 109. It shows a remarkably regular spider diagram of a rotating disk.

3.5.1 Tilted ring model

We continued by fitting a simple model to the data using GIPSY (van der Hulst et al. 1992, Vogelaar & Terlouw 2001), which contains a software package designed for
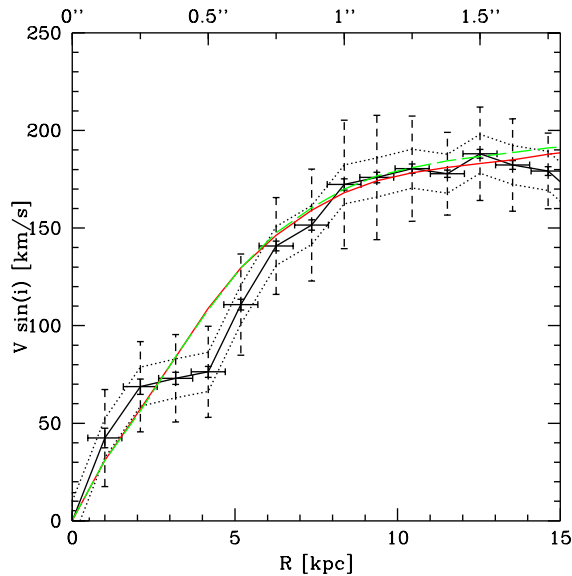
Figure 3.7 — Rotation curve from the velocity field model shown in Fig. 3.6b on page 109. To guide the eye, the data points (with errorbars) are connected by the (black) thick line and the dotted lines are $+10$ km s^{-1} and -10 km s^{-1}. The horizontal errorbars indicate the width of the rings. The full vertical errorbars are the errors on the fitted velocity, the dashed vertical errorbars are the range of velocities in the ring. The full (red) line is the best fit RC as discussed in Section 3.6.2 ($a = 1.0$, $b = 0.5$ and $i = 54°$). The long dashed (green) line shows an almost identical fit ($a = 1.1$, $b = 0.5$ and $i = 64°$).

fitting tilted rings to HI velocity fields. Free parameters for each ring are in principle the centre of the galaxy, its inclination, the position angle of the major axis, systemic velocity, expansion velocity and the rotation velocity. For simplicity, we fixed the centre to the centre of the FIRES data, and the inclination and position angle of the major axis to those of the FIRES K band image. We also fixed the systemic velocity to the velocity of the central pixel, and fixed the expansion velocity to zero. This leaves only the rotation velocity as a free parameter for each ring. The resulting model is shown in Fig. 3.6b on page 109 and the RC in Fig. 3.7. We will discuss the properties of the RC and the parameters of the the fit in the next section.

3.5.2 Residuals from fit

In Fig. 3.6c on page 109 we show the residuals of our tilted ring model fit. The lack of systematic residuals is a strong indication for a rotating disk. The mean absolute residual is 27 km s^{-1} while large residuals (> 52 km s^{-1}) only occur at the noisy outer edges of the galaxy. The mean residual excluding these points is 21 km s^{-1}.

These residuals are slightly larger than those of Wright et al. (2007) who observed a $z \sim 1.5$ disk galaxy and found a mean residual of 13 km s^{-1}. They note that this is only slightly larger than the deviations observed for local spirals (~ 10 km s^{-1}). They explain their larger deviations by beam smearing. Our seeing limited observation suffer even more from beam smearing than their AO observations. Modeling our residuals while taking into account these effects would require assumptions on the intrinsic distribution of the Hα flux and dispersion and the intrinsic velocity field. We did not attempt to make such a model as the many uncertainties would not add much to the current conclusion: the small random residuals provide evidence that F257 is a disk galaxy with a regular velocity field quite similar to that of local galaxies.

These results are in contrast to many other kinematic measurements of high-z galaxies which show significant deviations from regular rotation, e.g. the $z = 2.38$ galaxy for which Genzel et al. (2006) made a rotating disk model shows offsets up to ~ 170 km s^{-1}

(comparable to the maximum rotation curve velocity) and deviations from a simple disk geometry.

3.5.3 Dispersion field

A peak in the measured velocity dispersion at the centre of rotation would be consistent with a rotating disk model. Although the S/N of individual spectra is poor, we made an attempt to measure the velocity dispersion field. We measured the dispersion on the raw 1D spectra, corrected for instrumental resolution and then smoothed the dispersion map with a 2 pixel width Gaussian to increase S/N. The dispersion map is shown in Fig. 3.6d on page 109. The dispersion is larger in the centre (maximum is 103 km s^{-1}) and smaller in the outer parts (~ 65 km s^{-1}). The shape of the dispersion peak appears elongated, but the S/N is insufficient to make any statement about the precise shape.

Peaks in the centre are not commonly observed at this redshift: the $z = 2.4$ galaxy of Genzel et al. (2006) does show a peak in the centre but the overall shape is distorted, Förster-Schreiber et al. (2006a) find a peak for 1 out of 6 galaxies. Even at $z = 0.6$, Flores et al. (2006) find only 35% rotating disks (in their definition: the major axis of the velocity field coincides with the major axis of photometry plus a peak in centre of the dispersion field) in a representative sample of emission line galaxies.

3.5.4 Clumps

The Hα line map and F814W image showed a clumpy structure. This raises the question to what extent the observed velocity field is biased by the inhomogeneous surface brightness distribution of Hα, emphasizing selected velocity ranges. The flux in clumps is 10-30 % of the total flux (measured in F814W), so although prominent in the image, they will not dominate the velocity field observed. We checked this in the model velocity fields where the F814W image was used as model for the true Hα surface brightness distribution (see Sect. 3.6.2): there is no visible distortion of the velocity field at the location of the clumps. In addition, the smooth appearance of the velocity field and the agreement of kinematic and photometric (K band) major axis argues that the velocity field is dominated by the stellar mass. We conclude that the clumpy structure of the Hα surface brightness distribution has no significant impact on the velocity field observed.

3.5.5 Summary

The velocity field of F257 reveals a remarkably regular spider diagram. A tilted ring model, leaving only the rotation velocity as a free parameter for each tilted ring, fits the observations very well. The residuals from the fit are random and much smaller than in many other high-z galaxies with similar kinematic data (e.g. Genzel et al. 2006). The dispersion field shows an extended peak in the centre. The clumpy distribution of star formation activity has no significant impact on the velocity field observed. In the next section, we will discuss the RC found including the effect of PSF smearing on V_{flat} and R_{flat}, which we have ignored so far.
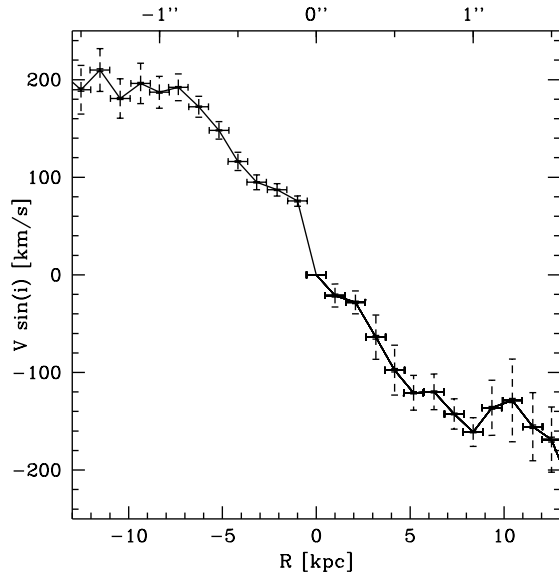
Figure 3.8 — Rotation curve from the velocity field model, approaching and receding side fitted separately. To guide the eye, the data points are connected by the thick line. The errorbars have the same meaning as in Fig. 3.7.

3.6 Rotation curve

The RC from the tilted ring model for the velocity field as discussed in the previous section was shown in Fig. 3.7. It rises until it reaches its maximum velocity of $\sim 170\,\mathrm{km\,s^{-1}}$ (not corrected for inclination) at $\sim 1''$ and then stays flat. Note that this velocity is significantly larger than the velocity found in the synthetic long slit spectrum which is probably due to the integration over the width of the synthetic slit. The synthetic long slit spectrum (see section 3.4 and Fig. 3.4) suggested that the RC flattens at both the receding and approaching ends at almost the same velocity. We repeated the fit of the velocity field as done in Sect. 3.5.1, but now fitting the approaching and receding sides separately. The resulting RC, shown in Fig. 3.8, confirms that the RC flattens at the receding and approaching half at the same radius and velocity. Although the Hα flux distribution is not symmetric (see linemap in Fig. 3.5), this appears to have no significant influence on the best fit RC. For simplicity and S/N, we use the fit of the entire velocity field in the remainder of this paper.

The errorbars on the RC were determined as follows: GIPSY calculates for each ring the error on the velocity ΔV and the range of velocities σ_V. The first is $\sim 3\,\mathrm{km\,s^{-1}}$, the latter on average $26\,\mathrm{km\,s^{-1}}$. Both ΔV and σ_V are shown in Fig. 3.7. Here, equal weights are assigned to all pixels. Within a single ring, all pixels have approximately the same Hα flux and hence the same errorbar. The S/N drops from the centre outwards while at the same time the number of pixels in the fit increases. Assuming the errorbar on the velocity of a single pixel scales with the inverse of the square root of the Hα flux, the errorbars on the RC are approximately constant except for the inner few rings and for $r \gtrsim 1\overset{''}{.}4$ where the errorbars increase.

3.6.1 Parameters of the fit

We now turn to the parameters we fixed when we made a model of the velocity field: the position angle of the major axis, inclination, centre, systemic velocity and expan-

Figure 3.9 — The observed RC (open squares connected by the black dashed line) and the PSF corrected RC (full squares connected by the red line).
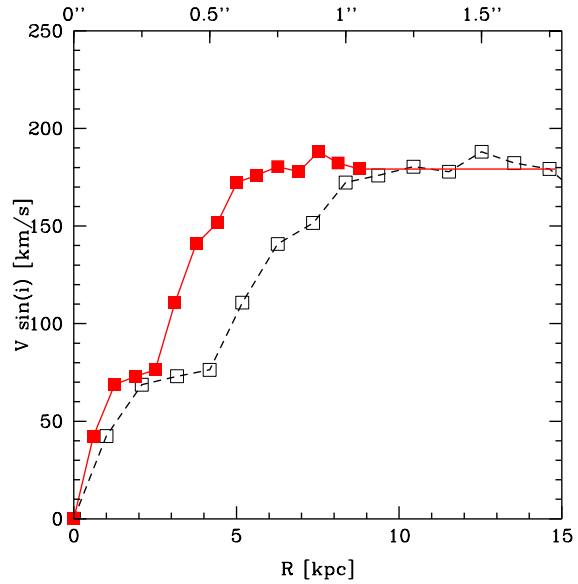
sion velocity. This is done in order to investigate if their values can be reproduced from the velocity field alone, and if so, if they are consistent with the values we assumed in Section 3.5.1. We also want to know the effect of small variations of these parameters on the best fit RC to get an estimate of the errorbars of the RC. It is not possible to leave all these parameters as free parameters at the same time. The number of free parameters is then too large for the number of independent data points, and the resulting best fit parameters for each ring vary strongly from ring to ring in an unphysical way (e.g. the inclination varies between 10 and 80°). Therefore, we study only the case of two free parameters: the rotation velocity plus one other parameter.

1. If the angle of the major axis is left as the second free parameter, one finds a consistent result between the orientation of the rings and the K band isophotes. This indicates that the orientation of the stellar mass distribution as traced by the K band light is consistent with the gravitational field as traced by the velocity field. Varying the position angle caused negligible changes in the RC of the fit.
2. When the expansion velocity is the second free parameter, we find $V_{exp} \sim 0$ km s^{-1} with small scatter in all rings.
3. Leaving the x and/or y position of the centre as free parameter(s), we find small (1-2 pixel) offsets from the K band centre, varying from ring to ring and with no significant effect on the RC found. When we vary the fixed centre around the K band centre, we also do not find systematic changes in the RC found. We therefore keep the centre at the K band centre.
4. We were not able to determine the inclination from the velocity field. If the inclination is a free parameter, the best fit inclination for each ring does not follow an ordered pattern, indicating that the S/N ratio does not allow determination of the inclination from the velocity field alone. However, fixing the inclination to different values causes small but systematic offsets in the flattening velocity: more edge-on galaxies have slightly smaller flattening velocities than more face-on galaxies. The difference between $i = 64°$ and $i = 44°$ is ~ 15 km s^{-1}. Without

the K band constraint on the inclination, this small systematic difference would result in a larger uncertainty in V_{flat}.

5. Leaving the systemic velocity as a free parameter, we find a small systematic offset from the velocity of the central pixel which we explain by the small difference in V_{flat} of the receding and approaching sides of ~ 10 km s^{-1}. The offset is smaller than the differences in V_{flat} we find fitting with different parameters (see conclusion below). Therefore, we ignore it in the remaining analysis.

6. GIPSY also offers different weighting possibilities to the pixels within a ring but this also does not significantly change the fitted RC.

We were able to reproduce all parameters except the inclination from the velocity field alone. They all agree within the errorbars with the a priori assumed values. The agreement between the centre and position angle of F257 in the Ks band image and the velocity field, and the agreement between the systemic velocity and the velocity of the centre, both strongly support the rotating disk interpretation.

Changing the parameters in the fit except the inclination results in random changes of the RC of the simplest model. The error on $V_{flat}\sin(i)$ derived by studying the variations due to the free parameter choice of the tilted ring model is ~ 15 km s^{-1}. Varying the inclinations causes systematic offsets, that will become important when converting the observed velocities to true inclination corrected velocities. Therefore, we will focus on the inclination hereafter and keep all other parameters fixed.

3.6.2 PSF

So far, we have ignored smearing of our velocity field by seeing. Although F257 is a large galaxy (we measure Hα over $\sim 3''$ diameter), the seeing of $0\rlap{.}''55$ has smeared the velocity field observed significantly. We will now model the effect of the PSF on the RC observed. For simplicity, we will focus on the RC only and not on the full velocity field. Specifically, we would like to know what the true $V_{flat}\sin(i)$ is, whether we can extract more information about the inclination of the galaxy and the radius where the RC flattens, R_{flat}.

We generated our model velocity fields by taking the observed RC and modify it according to

$$V_{model}(r) = \begin{cases} a * V_{obs}(br) & \text{if } br < r_{max} \\ a * V_{obs}(r_{max}) & \text{if } br > r_{max} \end{cases} \tag{3.1}$$

where $V_{obs}(r)$ is the velocity field observed at distance r from the centre, r_{max} is the largest radius for we could measure the rotation velocity, V_{model} is the velocity of the model, constant a scales the maximum velocity of the model and constant b scales the radius where the RC flattens. We then made synthetic model velocity fields (VF) for different a and b and created synthetic observations using

$$VF_{model,obs} = \frac{(VF_{model,a,b} \times F_{true}) \otimes PSF}{F_{true} \otimes PSF} \tag{3.2}$$

where $VF_{model,obs}$ is the model velocity field as "observed", $VF_{model,a,b}$ is the intrinsic model velocity field for constants a and b and F_{true} is the true flux distribution of the

emission line. F_{true} is of course also unknown. We used the F814W image, assuming that Hα and F814W (=rest frame UV) have the same distribution (as is likely, see section 3.4). We used the elliptical gaussian as reconstructed from the PSF star images for the PSF. We then fitted a RC to each model for different inclinations.

We found fitting RCs for $a = 1 - 1.1$. Larger values of a overpredicted $V_{flat}\sin(i)$ or R_{flat} (depending on the inclination), smaller values could not reproduce the maximum velocity observed. Our best fit $V_{flat}\sin(i)$ is then 179 ± 9 km s^{-1}.

The best fit RCs have $b = 0.5 - 0.6$, although acceptable fits can also be found for slightly larger values up to $b = 0.8$. If $R_{flat,obs} \approx 1''$, $R_{flat,true}$ becomes $0\rlap{.}''55 \pm 0\rlap{.}''15$ or 4.6 ± 1.3 kpc. Beam smearing has thus a profound effect on the observed flattening radius of the RC. This is illustrated in Fig. 3.9, where we show the observed RC and the PSF corrected RC. Although $R_{flat,true}$ is of the order of the seeing, the radius where the RC flattens is resolved: in the velocity field, the (true) flattening radius of the approaching and receding half are $2R_{flat,true}$ apart.

Including the effect of beam smearing in our analysis, we were not able to constrain the inclination better as is shown in the almost identical fits with different inclination in Fig. 3.7.

To summarise, we find $V_{flat}\sin(i) = 179 \pm 17$ km s^{-1}, $R_{flat} = 4.6 \pm 1.3$ kpc and no better constraints on inclination after correction for beam smearing. Using our best estimate of the inclination (from the K band photometry) $i = 54 \pm 5°$, we find $V_{flat} = 221 \pm 22$ km s^{-1}.

3.6.3 RC shape

The RC of F257 flattens at 4.6 ± 1.3 kpc. In the local universe, the R_{flat} depends on the bulge-to-disk ratio, larger bulge-to-disk ratio's correlating with steeper rising RCs (Noordermeer 2006). The RCs of local early-type spiral galaxies rise to their maximum velocity in < 1 kpc (Noordermeer 2006), which is clearly not the case for F257 as expected from the pure exponential disk profile found by Labbé et al. (2003a). Swaters, Madore & Trewhella (2000) compare the RCs of their low surface brightness late-type galaxies with three late-type high surface brightness galaxies from Begeman (1987). They all flatten at $2 - 5$ kpc. So, the shape of the RC of F257 appears consistent with late type local spirals.

Slowly rising RC at high redshift have also been noted by Swinbank et al. (2006). They studied gravitationally lensed galaxies at $z \sim 1$ using integral field spectroscopy and found that the galaxies with stable disk kinematics have slowly rising rotation curves and suggest that these have lower bulge-to-disk mass ratio's than their local counterparts.

3.7 Masses

From our model for the velocity field we calculate the total dynamical mass of the galaxy within $r = 1\rlap{.}''5$

$$M_{dyn} = \frac{v^2 r}{G} \tag{3.3}$$

and find $M_{dyn} = 1.4 \pm 0.3 \times 10^{11}$ M$_\odot$ (depending on geometric assumptions, this equation is found with different constants of order 1; when we compared our finding with those of others, we used their constant.)

Wuyts et al. (2007) made an extensive study of stellar masses for high redshift galaxies in HDF-S and found for F257 $3.5^{+0.5}_{-0.3} \times 10^{10}$ M$_\odot$ (using a Salpeter IMF). Using a 'diet' Salpeter IMF, a Salpeter IMF with 30% less mass to correct for the overprediction of low mass stars (as for example Bell & de Jong 2001), would reduce this mass to 2.5×10^{10} M$_\odot$.

A crude estimate of the gas mass may be found using the global Schmidt law for star forming galaxies which relates SFR and gas surface density (Kennicutt 1998, see also Bouché et al. 2007 for evidence that this relation also holds at high redshift). Using the SFR calculated from the Hα flux and the total area over which we observe Hα, this gives a total gas mass of $5.3 \times 10^{10} M_\odot$, and after correcting for extinction ($A_V = 1.0$, Wuyts et al. 2007) $8.7 \times 10^{10} M_\odot$. Although the interpretation of this number is uncertain due to the large scatter in the Kennicutt relation of ± 0.3 dex, it is comparable to or larger than the stellar mass, which is consistent with picture that this galaxy is building up its stellar mass at a fast rate.

From these masses, we get the following mass ratio's (Salpeter IMF, extinction corrected):
- $M_{gas}/M_* = 2.5$
- $M_*/M_{dyn} = 0.25$;
- $M_{baryon}/M_{dyn} = (M_* + M_{gas})/M_{dyn} = 0.9$
Local galaxies with similar gas-to-stellar mass ratio are rare, and such galaxies have stellar masses $\sim 1 - 2$ orders of magnitude smaller than the stellar mass of F257 (Kannappan 2004). Similar gas-to-dynamical mass ratio's are locally only found in extreme late type galaxies (Binney & Merrifield 1998). The gas-to-stellar mass ratio is consistent with the $z \sim 2$ rest frame UV selected galaxies of Erb et al. (2006). The stellar-to-dynamical mass ratio is at the low end of the range found by Erb. et al. They find galaxies with lower stellar-to-dynamical mass ratio's to be younger, and F257 is indeed a relatively young galaxy as found by Wuyts et al. Although F257 is photometrically young, its dynamical mass is at the high end of the range found by Erb et al.

The sum of stellar and baryonic mass is $1.2 \times 10^{11} M_\odot$ which is almost the same as the dynamical mass. Within the errorbars, there is no evidence for dark matter within $r < 12$ kpc in this galaxy.

F257 appears to be kinematically like a local late type spiral galaxy in many respects. We have seen that its velocity field is remarkably regular, a tilted model leaves small residuals and that the dispersion increases towards the centre. The RC slowly rises and then remains flat like those of local late type spirals. F257 is a very gas rich spiral compared to local galaxies. We will now further investigate the nature of this disk galaxy in terms of dynamical support and specific angular momentum. We will then investigate if it follows the local B, K, stellar and baryonic mass TFR.

3.8 Rotational support and specific angular momentum

Galaxies can be supported by rotation and/or dispersion. Disk galaxies are supported by rotation. V/σ is a measure of the dynamical support of a galaxy. There is no general agreement on what to use for σ for disk galaxies. Puech et al. (2007) use as σ the velocity dispersion in the z direction which they calculate from the mean observed σ in the outer regions of their disks. We followed Puech et al. (2007) and found an average σ_z of 57 km s^{-1} and hence $V/\sigma_z = 3.9 \pm 0.4$. This is comparable to the median V/σ_z found by Puech et al., $V/\sigma_z = 3.8 \pm 2$, for their $z = 0.6$ rotating disk galaxies. Their local comparison sample has median $V/\sigma_z = 6.1 \pm 1.1$ while their $z = 0.6$ perturbed rotating disks have $V/\sigma_z = 2.4 \pm 2.5$. Although the gas disk of F257 is heated compared to local galaxies, it is dynamically mainly supported by rotation, comparable to the $z \sim 0.6$ galaxies of Puech et al. (2007).

An important question in galaxy formation theory is when disk galaxies acquired their angular momentum. The specific angular momentum of a thin rotating disk is

$$\gamma = 2R_d V_{max} \tag{3.4}$$

which gives $\log(\frac{\gamma}{\text{kpc km s}^{-1}}) = 3.2 \pm 0.2$ for F257. This is slightly smaller than the average specific angular momentum of galaxies of the same mass at redshift zero, but consistent with the specific angular momentum - velocity relation for local galaxies (Puech et al. 2007, Navarro & Steinmetz 2000). Salucci et al. (2007) also found their $z \sim 1$ galaxies to be consistent with the local specific angular momentum - velocity relation. For other mass distributions, the factor 2 in equation 3.4 is slightly different, but this does not change our conclusion.

Another measure of angular momentum is the spin parameter λ. We followed again Puech et al. (2007) using their expression for λ in terms of disk scale length and flat rotation velocity and found $\lambda = 0.019 \pm 0.006$ which is comparable to the values found by Puech et al. (2007) for their $z \sim 0.6$ rotating disk sample and their local reference sample and also close to the estimate for the local value made by Tonini et al. (2006) ($\lambda \sim 0.03$).

We conclude that F257 is a dynamically fully formed disk galaxy: it is mainly rotationally supported and has the same specific angular momentum as local late type spirals. It is important to note that this makes F257 excellently suitable for a comparison with the local TFRs, which we will do now.

3.9 Tully-Fisher relations

Having established that F257 is dynamically very much like a local disk galaxy, we compare it to local TFRs to compare its baryonic components to dynamically similar local galaxies.

3.9.1 The rest frame B and K band TFR

In Fig. 3.10 we plot the local rest frame B band and rest frame K band TFR of Verheijen (2001) together with our data point for F257. F257 is marginally brighter than expected from the local B band TFR. The offset is 0.7 ± 0.4 mag in B band, where the errorbar
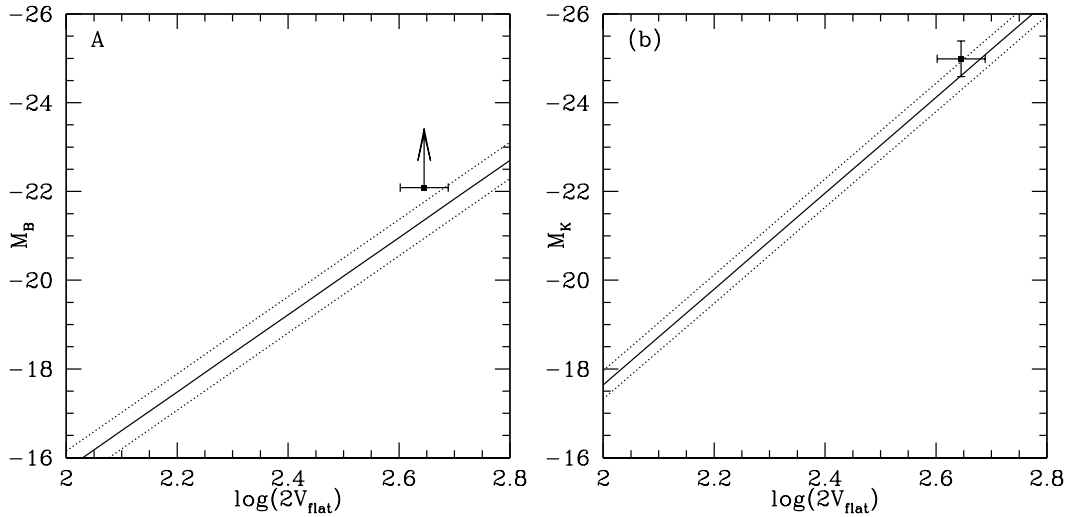
Figure 3.10 — The rest frame B band (left) and rest frame K band (right) TFR. The arrow indicates the extinction correction using the best fit A_V from Wuyts et al. (2007). The local TFR and its scatter (full and dashed lines) are from Verheijen (2001). The errorbar on the absolute B magnitude is smaller than the point size and is therefore not shown.

reflects the uncertainty due to the velocity uncertainty. Correcting for extinction using the A_V found by Wuyts et al. (2007), the offset increases to 2.1 mag. For comparison: the 1σ dispersion in the B band TFR as found by Verheijen (2001) is 0.41 measured along the magnitude axis.

F257 is consistent with the local K band TFR with $0.4 \pm 0.4 \pm 0.5$ mag brightening where the first errorbar reflects the errors bars in the IRAC fluxes from which the rest frame K band magnitude was calculated (F257 is blended with a nearby source), and the second reflects the uncertainty due to the velocity uncertainty. For comparison: the 1σ dispersion in the K band TFR as found by Verheijen (2001) is 0.32.

Local TFRs differ slightly from each other due to for example different choice of samples, different velocity parameters (e.g. linewidth or velocity, and also maximum or flat RC velocity) and RC fitting methods (e.g. Puech et al. 2008, Kannappan & Barton 2004). The differences are smallest at the high mass end of the TFR and do not change our conclusions (van Starkenburg et al. 2006 and references therein). We choose the Verheijen (2001) TFR as reference TFR because it is based on velocity fields, it is defined in optical and near-IR bands and uses the flat RC velocity, which (locally) minimizes the scatter in the TFR.

3.9.2   The stellar and baryonic mass TFR

The relation between the stellar mass and rotation velocity is known as the stellar mass TFR. When we compare F257 with the local stellar mass TFRs of Bell & de Jong (2001) and Pizagno et al. (2005) as shown in Fig. 3.11a, we find that F257 lies below these stellar mass TFRs (after reducing the stellar mass found by Wuyts et al. 2007 by 30% to account for the different IMFs used). The offset in $\log(M_*)$ is 0.66 ± 0.20 and 0.44 ± 0.12 respectively where the errorbars reflect the uncertainty due to the uncertainty in the
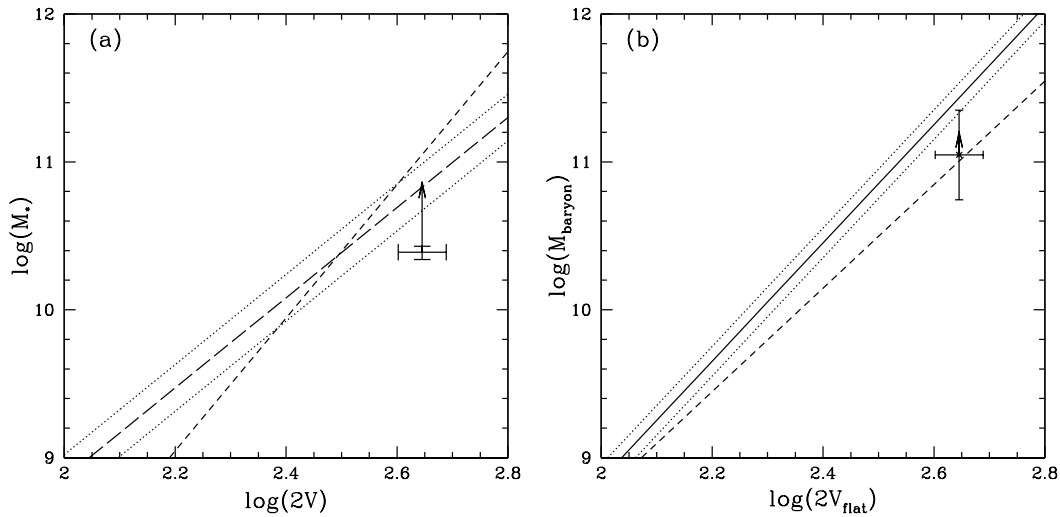
Figure 3.11 — a. The local stellar mass TFR and 1σ scatter of Pizagno et al. (2005) (long dashed and dotted lines) and Bell & de Jong (2001) (dashed line). b. The local baryonic mass TFR and 1σ scatter of Verheijen (2001) and Bell & de Jong (2001) (dashed line). The arrows indicate where F257 would lie for the maximally old plus young burst assumption (see text).

velocity (the uncertainty in the stellar mass was 0.05). The 1σ dispersion in the Pizagno et al. stellar mass TFR is 0.158 so the offset is significant at the $\sim 2\sigma$ level.

Wuyts et al. (2007) also discuss the effect on the best fit stellar mass of fitting a 2-component model instead of a 1-component model to the SED. The best fit stellar mass for a maximally old population plus a 100 Myr burst for F257 is 1.0×10^{11} M$_\odot$. This brings F257 in agreement with the local stellar mass TFR, as indicated by the arrow in Fig. 3.11. It is interesting to note that this 2-component model mass makes F257 a nearly ($\sim 75\%$) maximum disk.

Some authors (e.g. Verheijen 2001, Bell & de Jong 2001) added the gas mass to the stellar mass to get a baryonic mass TFR, see also Fig. 3.11b. Although the gas mass of F257 is uncertain due to the large scatter in the Kennicutt relation, we also compare F257 with these local baryonic mass TFRs and find that F257 is consistent with the baryonic mass TFR from Bell & de Jong (2001): $\log(M_{bar}) = -0.04 \pm 0.29 \pm 0.3$ where the first errorbar reflects the uncertainty due to the uncertainty in the velocity and the second errorbar reflects the uncertainty in the baryonic mass (assuming of a factor 2 uncertainty in the gas mass).

Although Bell & de Jong (2001) use an earlier version of the data set of Verheijen (2001), they find significantly different baryonic mass TFRs, especially at the high mass end. This difference is explained by the different M/L that they use to convert K band light to stellar mass. The (constant) M/L used by Verheijen is ~ 3 times larger than the (best fit for each galaxy) M/L of Bell & de Jong (2001). Verheijen (2001) uses this M/L because it minimizes the scatter in the baryonic mass TFR. However, according to Bell & de Jong, this M/L is unrealistically high. A lower M/L would shift the Verheijen relation downward, especially at the high mass (i.e. low gas fraction) end.

3.9.3 Comparison to other high-z samples

Several authors have attempted to measure rest frame near-IR and stellar mass TFRs at high redshift. Conselice et al. (2005) analyzed 101 disk galaxies in the redshift range $0.2 < z < 1.2$ and find no evolution in the rest frame K band TFR and in the stellar mass TFR.

Kassin et al. (2007) use a combination of rotation velocities and velocity dispersions ($S_{0.5} = \sqrt{0.5V_{rot}^2 + \sigma_{gas}^2}$) to construct a stellar mass TFR for galaxies with strong emission lines in the redshift range $z = 0.1 - 1.2$. This reduces the scatter in the stellar mass TFR. However, they find no z-evolution in the stellar mass TFR using this $S_{0.5}$ parameter. F257 is a rotation dominated galaxy and hence consistent with their normal stellar mass TFR and their $S_{0.5}$ parameter stellar mass TFR.

Weiner et al. (2006) study the rest frame B and J band TFR out to $z = 1.2$. They find significant brightening in rest frame B band (1-1.5 mag between redshift 0.4 and 1.2). However, although they find that the slope of the J band TFR evolves, the overall luminosity in J band does not.

Flores et al. (2006) published the first high redshift TFR using integral field spectroscopy. They observed a sample of [O II] emitting galaxies at $z = 0.4 - 0.75$ using the GIRAFFE IFU on the VLT. They find that only 35% of their sample are rotating disks in their definition (the major axis of the velocity field coincides with the major axis of photometry plus a peak in centre of the dispersion field). They find no evolution and small scatter in the rest frame K band and stellar mass TFR and some galaxies that are brighter in rest frame B band.

To summarize, other authors have not found evolution in the near-IR or the stellar mass TFR out to redshift 1.2. This non-evolution in near-IR $z = 1$ TFR was predicted by Buchalter, Jimenez & Kamionkowski (2001) and in the stellar mass $z = 1$ TFR by Portinari & Sommer-Larsen (2007). Our findings suggest that the K band TFR may not evolve out to redshift 2. F257 is $\sim 2\sigma$ below the stellar mass TFR, a hint that the stellar mass of F257 is still building up, which would be consistent with its young age, large SFR and gas mass. However, it should be noted that the offset depends on the SED modeling. If a maximally old population is added, F257 is consistent with the local stellar mass TFR.

3.9.4 Summary and discussion

We conclude that F257 is a fully formed, rotationally supported disk galaxy. Within the errorbars, it is consistent with the local K band TFR. The small offset from the local B band TFR can be explained by star formation activity and the young stellar population.

F257 lies slightly below the local stellar mass TFR, an offset significant at the 2σ level. Evolving from redshift 2 to the present, the stellar mass must increase without a significant increase in the K band luminosity. However, the best fit stellar mass strongly depends on the SED modeling. When we add a maximally old population, F257 is in agreement with the local stellar mass TFR.

F257 is consistent with the baryonic mass TFR, but the uncertainties are large. To study offsets from the baryonic TFR, one needs more galaxies and/or more accurate gas masses. We present our full sample in van Starkenburg et al. (2008b). In the near

future, ALMA will provide us with the latter.

We finally note that the regular dynamical structure of F257 is remarkable for its young age: the estimated age of the stellar population of ~ 160 Myr equals the rotation period of the galaxy at $1 - 2R_d$ and at $1 - 2R_{flat,true}$). Therefore, the galaxy has dynamically relaxed on a very short timescale, much shorter than the timescale for the buildup of the final stellar population.

3.10 Summary and conclusions

Labbé et al. (2003a) presented photometric evidence that F257 is a large disk galaxy at $z = 2.03$. We confirm the disk nature of this galaxy by its kinematical properties and find that is in many respects similar to local disk galaxies. Specifically, we find:

1. The velocity field is consistent with a rotating disk galaxy, a tilted ring model leaves small random residuals and no evidence for non circular motions;
2. There is no evidence for an AGN in the form of broad lines or a large [N II]/Hα ratio;
3. The [N II]/Hα ratio peaks in the centre;
4. The disk is primarily rotation supported: $V/\sigma_z \sim 3.9$;
5. The dispersion increases towards the center;
6. The RC slowly rises like that of a late-type spiral in the local universe and then flattens. There is no evidence for dark matter within $r < 12$ kpc;
7. F257 has a specific angular momentum and spin parameter comparable to those of local galaxies;
8. F257 is consistent with the local K band TFR;
9. F257 lies below the local stellar mass TFR at the 2σ level and is consistent with the local baryonic mass TFR. A 2-component model for the SFH increases the stellar mass so that F257 is consistent with the stellar and baryonic mass TFR and makes F257 a nearly maximum disk.

Despite its very young age, high star formation rate, gas mass and clumpy star formation, F257 is very similar to local late type spiral galaxies. Its dynamical properties are more like those of local galaxies than those of other galaxies observed at similar redshift.

These findings put constraints on the evolution of F257 from $z = 2.03$ to the present. If the stellar mass increases so that F257 becomes consistent with the local stellar mass TFR, the K band mass-to-light ratio must also increase so that that the total K luminosity does not change. Infalling gas must have the same specific angular momentum as the galaxy, i.e. it must fall in from the outer parts of the present halo.

Acknowledgements

References

Barden, M. 2003 astro-ph 0308272

Begeman, K.G. 1987 PhD thesis

Bell, E.F. & de Jong, R.S., 2001, ApJ 550 212

Binney, J. & Merrifield, M. 1998, Galactic Astronomy (Princeton University Press, Princeton) 494

Bonnet, H. et al. 2004, The ESO Messenger 117, 17

Bouché, N. Cresci, G., Davies, R. et al. 2007 astro-ph 0706.2656

Bruzual, G. & Charlot, S. 2003, MNRAS 334 1000 1028

Buchalter, A. Jimenez, R. & Kamionkowski, M. 2001 MNRAS 322 43

Conselice, C.J., Bundy, K., Ellis, R.S. et al. 2005 ApJ 628 160

Courteau, S., Dutton, A.A., van den Bosch, F.C. et al. 2007, ApJ 671 203

Denicoló, G., Terlevich, R. & Terlevich, E. 2002 MNRAS 330 69 74r

Eisenhauer, F. et al. 2003, SPIE 4841, 1548

Erb, D.K. Steidel, C.C., Shapley, A.E. et al. 2006 ApJ 646 107

Flores, H., Hammer, F., Puech, M., Amram, P. & Balkowski, C. 2006 A&A 455 107

Förster-Schreiber, N. M., Franx, M., Labbé, I. et al. 2006a AJ 131 1891

Förster-Schreiber, N. M., Genzel, R., Lehnert, M.D. et al. 2006b ApJ 645 1062

Franx, M., Labbé, I., Rudnick, G. et al. 2003 ApJ 587 L79

Genzel, R., Tacconi, L.J., Eisenhauer, F. et al. 2006 Nature 442 786

Giavalisco, M., Steidel, C.C. & Macchetto, F. D. 1996 ApJ 470 189

Governato, F., Willman, B., Mayer, L. et al. 2007 MNRAS 374 1479

Kannappan, S. J. 2004 ApJ 611 L89

Kannappan, S.J. & Barton, E.J. 2004 AJ 127 2694

Kassin, S.A., de Jong, R.S. & Weiner, B.J. 2006 ApJ 643 804

Kassin, S.A., Weiner, B.J., Faber, S.M. et al. 2007 ApJ 660 L35

Kennicutt, R.C. 1998, ApJ 435 22

Labbé, I., Rudnick, G., Franx, M. et al. 2003a ApJ 591 L95

Labbé, I., Franx, M., Rudnick, G. et al. 2003b AJ125 1107

Labbé, I., Huang, J., Franx, M. et al. 2005 ApJ 624 81

Law, D.R., Steidel, C.C., Erb, D.K. et al. 2007 astro-ph 0707.3634

Lemoine-Busserolle, M., Contini, T., Pelló, R. et al. 2003 A&A 397 839

Lilly et al. S., Schade, D., Ellis, R. et al. 1998 ApJ 500 75

Lowenthal, J.D., Koo, D.C., Guzman, R. et al. 1997 ApJ 481 673

Mo, H. J., Mao, S. & White, S.D.M. 1998 MNRAS 295 319

Modigliani, A., Hummel, W., Abuter, R. et al. 2007 arXiv:astro-ph 0701297

Moorwood, A.F.M., van der Werf, P. P., Cuby, J. G. & Oliva, E. 2000 A&A 362 9

Moorwood, A.F.M., van der Werf, P.P., Cuby, J. G., & Oliva, T. 2003, Rotation and Masses of Galaxies at $z \sim 3.2$ in The mass of galaxies at low and high redshift, ed. R. Bender, & A. Renzini (Berlin: Springer), 256

Navarro, J.F., Frenk, C.S. & White, S.D.M. 1995, MNRAS 275 56

Navarro, J.F. & Steinmetz, M. 2000 ApJ 538 477

Nesvadba, N.P.H., Lehnert, M.D., Eisenhauer, F. et al. 2006 ApJ 650 661

Noordermeer, E. 2006 PhD thesis Chapter 4

Okamoto, T. 2007 astro-ph 0712.0086

Pizagno, J., Prada, F., Weinberg, D.H. et al. 2005 ApJ 633 844

Portinari, L. & Sommer-Larsen, J. 2007, MNRAS 375 913

Puech, M., Hammer, F., Lehnert, M.D. & Flores, H. 2007 A&A 466 83

Puech, M., Flores, H, Hammer, F. et al. 2008 A&A arXiv:0803.3002

Salucci et al. 2007, astro-ph 0708.0753

Schade, D., Carlberg, R.G., Yee, H.K.C., Lopez-Cruz, O. & Ellingson, E. 1996 ApJ 465 103

Silk, J. 1997 ApJ481 703

Simard, L., Koo, D.C., Faber, S.M. et al. 1999 ApJ519 563

Steinmetz, M. & Navarro, J.F. 1999 ApJ 513 555

Swaters, Madore & Trewhella 2000 ApJ 531 107

Swinbank, A.M., Bower, R.G., Smith, G.P. et al. 2006 MNRAS 368 1631

Tonini, C., Lapi, A., Shankar, F. & Salucci, P. 2006 ApJ 638 L13

Trujillo, I. Förster Schreiber, N.M., Rudnick, G. et al. 2006 ApJ 650 18

Tully, R. B. & Fisher, J. R. 1997 A&A54 661

van den Bosch, F.C. 2000 ApJ 530 177

van der Hulst, J.M., Terlouw, J.P., Begeman, K., Zwitser, W. & Roelfsema, P.R. "The Groningen Image Processing System, GIPSY", in: Astronomical Data Analysis Software and Systems I, (eds. D. M. Worall, C. Biemesderfer and J. Barnes), ASP Conf. series no. 25, p. 131, 1992

van Dokkum, P.G., 2001, PASP, 113, 1420

van Starkenburg, L., van der Werf, P.P., Yan, L. & Moorwood, A.F.M. 2006 A&A 450 25 (Chapter 2)

van Starkenburg, L. et al. 2008a in prep. (Chapter 4)

van Starkenburg, L. et al. 2008b in prep. (Chapter 5)

Vanzella, E., Cristiani, S., Arnouts, S. et al. 2002 A&A 396 847

Verheijen, M. A. W., 2001, ApJ 563 694

Vogelaar, M.G.R. & Terlouw, J.P. "The Evolution of GIPSY, or the Survival of an Image Processing System", in: Astronomical Data Analysis Software and Systems X, (eds. F. R. Harnden, Jr., F. A. Primini & H. E. Payne), ASP Conf. series Vol. 238, p. 358, 2001.

Vogt, N.P. Forbes, D.A., Philips, A.C. et al. 1996 ApJ 465 L15

Vogt, N.P., Philips, A.C., Faber, S.M. et al. 1997 ApJ 479 L121

Weiner, B.J., Willmer, C.N.A., Faber, S.M. et al. 2006 ApJ 653 1049

Wright, S.A., Larkin, J.E., Barczys, M. et al. 2007 ApJ 658 78

Wuyts, S., Labbé, I., Franx, M. et al. 2007 ApJ 655 51

Ziegler, B.L., Böhm, A., Fricke, K. J. et al. 2002 ApJ564 69

Appendix A.   FOV reconstruction

A.1   Introduction

Our targets are too faint to acquire directly or to detect in individual frames. When we made our first observations with SINFONI, we adopted the normal strategy for these faint targets: blind offsetting from a nearby bright star. We also followed the recommendation in the SINFONI manual to reobserve the blind offset star in the same OB as the science observations to be able to accurately combine the data from different OBs. We refer to these star observations as "PSF stars" (the template used for the observation is the calibration template "PSF").

We also followed the standard procedure to reconstruct the FOV from the raw images. SINFONI's FOV is sliced into 32 slitlets (see also Fig. A.1) that are combined into a single pseudo-slit and then dispersed. These 32 slitlets are projected on the detector in a brick-wall pattern. The slitlet distances (measured on calibration data made with fibers) define the distances on the detector between points with the same x coordinate (see Fig. A.1 for a definition of the x and y direction). These slitlet distances are used to reconstruct the FOV in the reduction process.

Having reduced our first data sets, we noticed that the reconstructed images of the PSF and standard stars showed some peculiarities. The centre of the star changed from slitlet to slitlet, often back and forth, but in some cases the gradual shift in centre resulted in a stretched stellar image. An example is shown in Fig. A.2. Also, the overall shape of the stars was not round but elliptical, especially if the seeing was good. FWHM ratios varied between 1 and 1.6, much larger than we could explain. As all reconstructed stars looked different, a simple error in the slitlet distances was excluded.
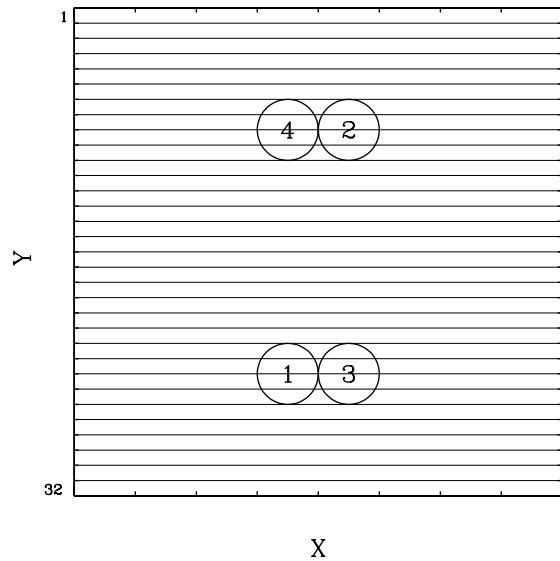
Figure A.1 — SINFONI observing strategy. The target is observed at positions 1, 2, 3 and 4. The distance between position 1 and 3 is 1″, and the distance between 1 and 4 is 4″. The positions of the slitlets and the X and Y directions are marked. Slitlets are numbered from top to bottom. The total FOV size is 8″times 8″.
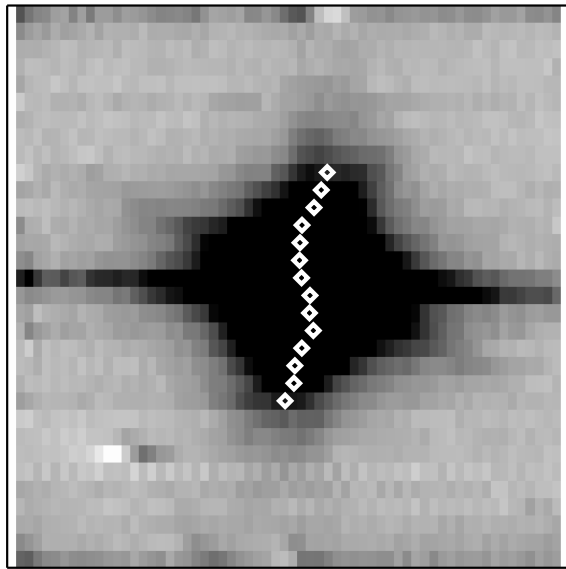
Figure A.2 — The reconstructed image of one of the bright standard stars observed for F257. To guide the eye, the center of the star in each slitlet has been marked.

After careful study of the reconstructed images of our PSF and standard stars of our first observing runs, we concluded that the details of SINFONI's FOV reconstruction are more complicated and that the quality of the velocity fields measured might be improved if the details are treated carefully. In this Appendix, we describe our investigations, the effects we found, their effect on the data quality and our new improved observing strategy.

A.2   Further investigations: varying pixel scale

To investigate the details of SINFONI's FOV reconstruction, a PSF star was observed at the same positions in the FOV as the science target, in some cases even before and after the science target. The positions in the SINFONI FOV are shown in Fig. A.1.

   When we compared the star traces of the PSF stars that are in the same slitlets in

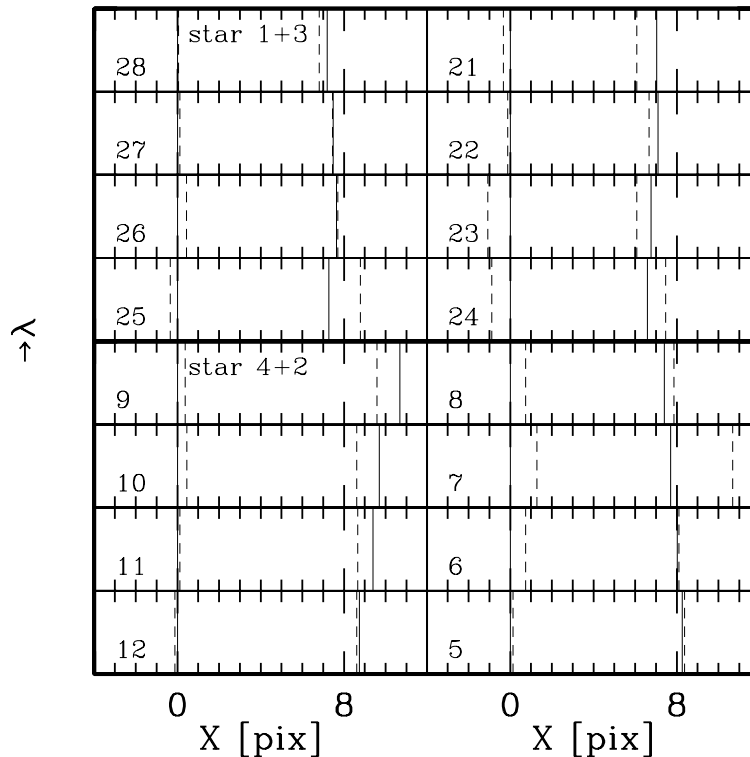**Figure A.3 —** The star traces for the test observing sequence with observing strategy as shown in Fig. A.1. Each panel represents one slitlet, the slitlet number is indicated in the lower left of each panel. The vertical lines show the positions of the star traces before (full lines) and after (dashed) lines observations of the science frames (time difference is about 1 hour). For each slitlet, the position of the first observation of the left star has been shifted to zero. The centers of the two stars could be measured in 8 slitlets. Those of the two stars in the lower half of the FOV (stars 1 and 3 in Fig. A.1) are in the upper 8 panels, those of the stars in the upper half of the FOV (stars 2 and 4 in Fig. A.1) are in the lower 8 panels. The distance between two star traces should be 8 pixels if the pixel scale is 0".125. Note that the distances between the two stars are different and change differently in each slitlet. Also note that the distance is less than 8 pixels for most slitlets in the lower half of the FOV and more than 8 pixels for most slitlets in the upper half of the FOV.

the *raw* frames (i.e. stars 1 and 3, and stars 2 and 4 in Fig. A.1), we noted that the distance between the star traces varies as is illustrated in Fig. A.3. From the telescope offset in the x direction (1") and SINFONI's spatial pixel scale (0".125 pix^{-1}) the distance between the star traces should be 8 pixels in all slitlets. The average value we found was indeed 8 pixels, but we found offsets of $\sim 10\%$ around this value (see Fig. A.3). In other words: the pixel scale varied up to 10%. The effect was not stable in time, we have seen significant changes in only 1 hour as can also been seen in Fig. A.3.

We emphasize that we measured these positions on the *raw* frames, so that reduction artifacts are excluded. Also, this effect is not caused by errors in the telescope offset: the pixel scale also varied (by less than 10%) from slitlet to slitlet for a single pair (see the upper or lower half of the panels in Fig. A.3), and the pixel scale in the y direction (i.e. the distance between stars 1 and 4 or 2 and 3 in Fig. A.1) was stable to measurable accuracy.

This explains the odd shapes of the reconstructed stellar images. The slitlet distances measured on fiber data are only valid for that observation and only approximately valid for other observations. The changing pixel scale explains why the FWHM of the stars in x and y direction is not the same for good seeing data.

SINFONI is a Cassegrain-mounted instrument, which makes is sensitive to flexure. As we saw in later observing runs (where we adopted our new multiple PSF star strategy (see below)) in many consecutive hours of observations of the same target, the pixel scale changes smoothly in time and hence parallactic angle. Therefore, we suspect flexure in the instrument as the origin of the effects described above. This could also explain the 'moving slitlets' phenomenon: for some parallactic angles, the positions of the slitlets on the detector shifts up to ~ 2 pixels in a few hours (of observing the same target).

We do not have sufficient observations of PSF stars to be able to predict the pixel scale for a given slitlet at a given target at a given time (or even to be sure that pixel scale can be predicted from parameters like parallactic angle and airmass). We have indications that the upper and lower half of the FOV have systematically different pixel scales (as is the case for the example shown in Fig. A.3). We only looked at data taken with SINFONI's largest FOV without AO and have not searched for differences between J, H, H+K and K band although we have noted these effects in all 4 filters.

A.3   Effects on data quality

Given these complex pixel scale changes, the question arose what the consequences were for data sets with observation of a single PSF star and what improvements could be made in future observations (including the observations discussed in this paper).

We assumed that the addition of many frames will average out the pixel scale differences so that the pixel scale in the combined image is the same in both spatial directions: 0.″125 (which seems safe to assume, as the pixel scales we find have on average this value). The changes in object size are negligible compared to the seeing even for the large high redshift galaxies in our sample, moreover seeing variations are usually larger than 10%.

However, the varying pixel scale results in a position uncertainty which can be important. In our science exposures, the telescope offset between A and B frames in the x direction is about 4″ for all our data (this paper, and van Starkenburg et al. 2008a, 2008b). 10% of 4″ is comparable to our best seeing observations (e.g. this paper 0.″55). This position uncertainty causes an additional smear in the x direction which cannot be removed with the observation of one PSF star per OB. As our targets are too faint to measure their position in individual frames, our new observing strategy should solve this position uncertainty in another way.

To summarize: the varying pixel scale causes a position uncertainty that could degrade the data quality in one spatial direction if the target is faint and observed under good seeing conditions.

A.4 Multiple PSF star observing strategy

Given these results, we changed our observing strategy as follows. The position uncertainty is the most important factor to correct. Observing a PSF star at every position where we observed the science target and as closely in time as possible provides us with accurate positions (i.e. in term of an ABB'A'-like observing cycle $A_{psf}B_{psf}A_{science}$-$B_{science}A'_{science}B'_{science}A'_{psf}B'_{psf}$). We then use these PSF positions when we combine our data.

As a bonus, we can seeing-weight the images (using the FWHM in the y direction) to improve image quality further. Another benefit is that we do not have to worry about the 'moving slitlet' effect anymore (it is unclear whether the moving slitlets are simply a shift in projection of the same part of the sky or a projection of a slightly different part of the sky or a combination of both).

When preparing the observations, we also take into account that the FOV size might be slightly smaller in the x direction than expected or that the target might be closer to the edge of the FOV than you would expect from the offsets. Also, when possible we put the major axis of the galaxy along the y direction in the FOV to ensure maxium resolution where we need it most.

We did not attempt to correct the individual frames and slitlets for the pixel scale variations as we saw before that these effects are negligible compared to the seeing. Moreover, in the case of correcting individual slitlets, one would need very bright PSF stars to get enough flux in all slitlets where the (large) science target is, and those are in general not available (the example shown in Fig. A.3 is with a very bright PSF star).

A.5 Other artifacts

For the very bright standard stars, we noted that their centres in the reconstructed image varied as a function of wavelength. This may indicate even more complex flexure effects, but a more probable explanation is that the distortion correction of the (earlier versions of the) SINFONI pipeline did not remove the distortion entirely. As we are only interested in a single emission line, we solved this by measuring the position and shape of the PSF stars at the wavelength of the emission line.

Chapter 4

The Tully-Fisher relation of ISO $15\mu m$ selected galaxies at $z \sim 0.7$

Context The Tully-Fisher relation (TFR) and its evolution put strong constraints on the formation and evolution of disk galaxies, especially on the relation between dark and luminous matter. Evolution in the stellar mass TFR relates the build-up of stellar mass to the mass of the halo.

Aims We aim to measure the rest frame B and K band and the stellar mass TFR of ISO $15\mu m$ selected galaxies at $z \sim 0.7$.

Methods We observed three ISO $15\mu m$ detected galaxies at $z \sim 0.7$ with the near-IR integral field spectrograph of the VLT, SINFONI, aiming at Hα. We derive velocity fields (VFs) for two galaxies, that are consistent with rotating disks. We combine this data with other spectroscopic observations of galaxies from the same sample. We derive stellar masses for the entire sample by spectral energy distribution (SED) fitting. We compare our results with a different SED fitting method from literature, with more freedom in the star formation histories.

Results We find that the results for the rest frame B band TFR are very sensitive to extinction corrections. The rest frame K band TFR is slightly less luminous than the local relation ($\sim$ 0.5 mag). We also find that $z \sim 0.7$ galaxies have smaller stellar masses than their local counterparts. The amount of evolution depends on the method for the stellar mass estimates. Using the two different estimates, we find 0.81 and 0.36 dex evolution. Our results are consistent with the [O II] derived $z \sim 0.6$ rest frame K band and stellar mass TFR of Puech et al. 2008.

L. van Starkenburg, P. P. van der Werf & S. Wuyts
to be submitted to *Astronomy & Astrophysics*

4.1 Introduction

The TFR defines a tight correlation between the luminosity and rotation velocity of spiral galaxies (Tully & Fisher 1977). The tightest correlation is found using near-IR luminosities and the velocity of the flat part of the rotation curve (RC) (Verheijen 2001). If luminosity is converted to stellar mass, one obtains the stellar mass TFR. The stellar mass TFR relates the properties of the dark halo with the baryonic mass of the galaxy as a function of dynamical mass.

The origin of the TFR is still not well understood. Recently, Courteau et al. (2007) showed that two theoretical predictions for the slope of the TFR are related. The TFR and its evolution with redshift put strong constraints on galaxy formation and evolution theories, in particular on the connection between dark and luminous matter (van den Bosch 2000). There are no models that can simultaneously reproduce the slope, scatter and zero-point of the TFR and the zero-point and shape of the luminosity function (e.g. Courteau et al. 2007 and references therein).

H I is a perfect tracer for the VF of disk galaxies, but cannot be used at cosmological redshifts. Rest frame optical emission lines, such as [O II] and Hα, are luminous and can be detected to $z \sim 2$ and higher using near-IR spectroscopy. Their extent is however limited to the star forming disk. Only recently, it has become possible to do integral field spectroscopy at near-IR wavelengths, for example with SINFONI at the VLT, opening the window for $z > 0.5$ TFR studies using integral field spectroscopy. Integral field spectroscopy has some major advantages over slit spectroscopy, as kinematic disturbances are more easily missed by slit spectroscopy.

The VFs are observed using rest frame optical emission lines like [O II] and Hα. Therefore, VFs can only be obtained for galaxies with a sufficiently high star formation rate (SFR). The luminosities of massive galaxies are less effected by the luminosity of a starburst than those of less massive galaxies (van Starkenburg et al. 2006). Therefore, massive galaxies are of special interest in high redshift TFR studies.

Franceschini et al. (2003) selected from a sample of galaxies detected in the ISO LW3 filter ($\lambda_{eff} = 15\mu m$) all galaxies with optical and near infrared photometry from the ESO imaging survey (EIS) (da Costa et al. 1998). Furthermore, these galaxies were required to have a secure counterpart in the I or K image and the (expected) wavelength of Hα should be observable with ISAAC. They present optical and/or near infrared spectroscopy for 21 of these 25 sources. Their redshifts are between 0.2 and 1.6.

Franceschini et al. (2003) find that these 15μm selected galaxies have large baryonic masses, even when compared to K-selected galaxies at similar redshift. These large baryonic masses ($\sim 10^{11} M_\odot$ as derived from modeling of the UV+optical+nearIR SED) are in agreement with the large dynamical masses derived from resolved RCs measured by Rigopoulou et al. (2002) using medium resolution ISAAC spectra for three of these sources. Some of the high resolution HST F814W images of these galaxies show bulges and spiral arms. These galaxies are therefore suited for TFR studies. In this paper, we present integral field observations of three galaxies from the Franceschini et al. (2003) sample. We also observed MIPS 24μm selected sources at $z \sim 2$. As this is essentially the same selection criterium at larger redshift, we can make a clear compar-

ison between two redshift ranges. The results for the MIPS 24μm sources are presented in a different paper (van Starkenburg et al. 2008b).

This paper is organized as follows: the sample is presented in Sect. 4.2. Then we discuss the observations and data reduction in Sect. 4.3 and Sect. 4.4. Sect. 4.5 gives general results from spectroscopy and SED fitting, and the derived VFs and RCs are discussed in detail in Sect. 4.6. We continue with a discussion of the masses in Sect. 4.7 followed by the TFRs of this sample in Sect. 4.8. We finish with a summary and conclusions in Sect 4.9.

Throughout this paper, we use $H_0 = 70$ km s^{-1}Mpc^{-1}, $\Omega_M = 0.3$, $\Omega_\Lambda = 0.7$ and Vega magnitudes.

4.2   Sample

From the source list of Franceschini et al. (2003) we selected all targets for which the wavelength of Hα is observable with SINFONI (the ISAAC observations were done with Z, SZ, J and H band gratings, SINFONI has J,H and K gratings) and that were not identified as AGN by Franceschini et al. (2003). We also required that the target could be kept inside SINFONI's field of view (FOV) during the observations, which can be difficult due to the large size of the galaxies compared to the FOV of SINFONI. This excluded one target in a very crowded region. The remaining four targets were prioritized according to Hα flux. We were able to observe three targets (S43, S55 and S62).

S43 and S55 fall inside the area of the HDF-S FIRES field for which we have UV+optical+nearIR+IRAC photometry (Labbé et al. 2003, 2005). S62 falls outside this area, and we use EIS UV+optical+nearIR photometry for this source.

4.2.1   Additional data

Spectroscopic data exist of another six ISO galaxies of the Franceschini et al. (2003) sample. We used those data to enlarge our sample when studying the TFRs in Section 4.8.

Medium resolution ISAAC long slit spectra targeting Hα exist for three sources: S25 (which is a pair of galaxies that are similar in size and mass), S27 and S55 (Rigopoulou et al. 2002). These targets were randomly chosen from the Franceschini et al. (2003) sample.

Puech et al. (2008 and references therein) observed a sample of [O II]$\lambda 3727$ emitting galaxies at $z \sim 0.6$. Three of the galaxies of their sample are also in the ISO sample of Franceschini et al. (2003) (S14, S23, which seems a triple system, and S53, which appears to be an interacting system of a large and a small source). They used the optical integral field spectrograph GIRAFFE at the VLT, aiming at [O II] and hence observed slightly lower redshift galaxies than Rigopoulou et al. (2002).

For all these sources, we have EIS UV+optical+nearIR photometry and for some also FIRES UV+optical+nearIR+IRAC photometry. Identifications, redshifts, emission line observed and slit/IFU observations are summarized in Table 4.1

Table 4.1 — Observed redshifts and rotation velocities of ISO galaxies. The ISO IDs are from Franceschini et al. (2003) and refer to the ISO detections. In some cases, the optical and near infrared images show a merger or multiple components. In those cases, we labeled these components a,b,c and specified their identification in the last column, see also Sect. 4.6.3. References are Rigopoulou et al. (2000, 2002) and Puech et al. (2008). Rotation velocities are in units km s^{-1}.

ISO ID	FIRES ID	Puech ID	z	line	slit/IFU	V_{flat}	author
S43	686	—	1.12[a]				
S55	610	—	0.76	Hα	IFU	250 ± 50	this work
S62	—	—	0.70	Hα	IFU	190 ± 30	this work
S14	—	4130	0.41	[O II]	IFU	220 ± 53	Puech08
S23a[b]	9	4170	0.46	[O II]	IFU	230 ± 37	Puech08
b[c]	14	—	0.46	Hα			Rigopoulou00
c[d]	29	—	—				
S25a[e]	591	—	0.58	Hα	slit	260 ± 45	Rigopoulou02
b[f]	820	—	0.58	Hα	slit	249 ± 52	Rigopoulou02
S27	193	—	0.58	Hα	slit	460 ± 40	Rigopoulou02
S53a	409	5030	0.58	[O II]	IFU	130 ± 69	Puech08
b[g]	410	—	0.58				
S55	610	—	0.76	Hα	slit	270 ± 75	Rigopoulou02

[a] redshift from Vanzella et al. (2002).
[b] SW component
[c] center component
[d] NE component
[e] SW component
[f] NE component
[g] small clump near S53a

4.3 Observations

We observed our ISO galaxies with the near-infrared integral field spectrograph of the VLT: SINFONI (Eisenhauer et al. 2003, Bonnet et al. 2004). We used its largest FOV (8″x 8″, or 0.″125 pixels) and the J band grating which has $R \sim 2000$ or FWHM ~ 170 km s^{-1}.

We used the same observing strategy as described in van Starkenburg et al. (2008a), except that we observed only one PSF star per OB. We refer to van Starkenburg et al. (2008a) for a detailed description of our observing strategy. Briefly, we blind offset from a nearby bright star as our targets are too faint to acquire directly. We kept the target inside the FOV but at different locations, comparable to the ABA′B′ cycles used in near-infrared long slit spectroscopy. This ensures maximally efficient use of observing time. Individual exposures were 900s, and the total (on source) integration times was 2hrs, 5hrs15min and 3 hours for S43, S55 and S62 respectively. The observing conditions were moderate, with seeing in the combined data cubes of 0.″8 and 1″ for S55 and S62 respectively (as measured on the PSF stars). We observed telluric standard stars for flux calibration.

Figure 4.1 — Reconstructed median collapsed cube with star-like persistence effect (left) and with the effect removed (right) on the same intensity scale. Shown is the full $8'' \times 8''$ FOV of SINFONI. The continuum emission from the target is too faint to detect in this case. Other residuals are still visible in the right panel.
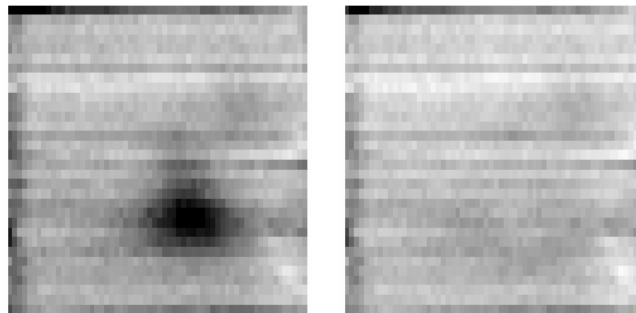
4.4 Data reduction

We used a combination of IRAF tools and SINFONI pipeline recipes (Modigliani et al. 2007) for data reduction. We refer to van Starkenburg et al. (2008a) for a detailed description of our data reduction strategy. We followed that strategy as much as possible for this data set. In summary, we first remove bad pixels and cosmic rays from the raw frames using LA_COSMIC (van Dokkum 2001). We remove the odd-even effect by averaging each column with its neighbours (this has negligible effect on the shape of the PSF compared to other smearing effects, see below and van Starkenburg et al. 2008a). We reduced the calibration frames (dark, linearity, flat fields, distortion and arc frames) using the SINFONI pipeline (version 1.6) to obtain a dark, flat field, bad pixel map, distortion correction, wavelength calibration and slitlet positions on the detector. The science frames are then flat fielded, distortion corrected, wavelength calibrated and combined in pairs (similar to the first subtraction in near infrared long slit spectroscopy).

In J and H band, a star like persistence effect with constant slope spectrum is sometimes observed at the beginning of an OB. An example is shown in Fig. 4.1. For illustrational purposes, this example was chosen from the J band observations because the effect is strongest in J band. It is faint but in some cases, we start to see the continuum emission of our target only after we remove this persistence effect. Its origin is unclear, although its constant slope spectrum points to lamp light. During another observing run, we tried to identify the source of the persistence effect, but failed to do so. It can be removed by fitting (after the first subtraction) the slope of the spectrum, creating an artificial long slit spectrum for each slitlet with appropriate center, FWHM and flux (as determined in the median collapsed cube), and then subtract it from the original cube. The effect can be removed from the second pair of frames in the OB by scaling the total flux (for DIT=900 s, this is about 15%). We removed this persistence effect for S43 (one OB), S55 (three OBs) and S62 (two OBs).

We combined our data using the positions measured from the PSF star and the telescope offsets (second subtraction). We observed only one PSF star per OB for this data set. Later, we found this number to be insufficient for accurate combination of the data (see van Starkenburg et al. 2008a). However, the seeing conditions for this data set are mediocre so that the additional smearing is relatively small ($\sim 10\%$). For the first 1hr45min of data of S55, we do not have PSF stars at all. As the quality of that data is significantly worse than the remaining 3hrs30mins due to the observational
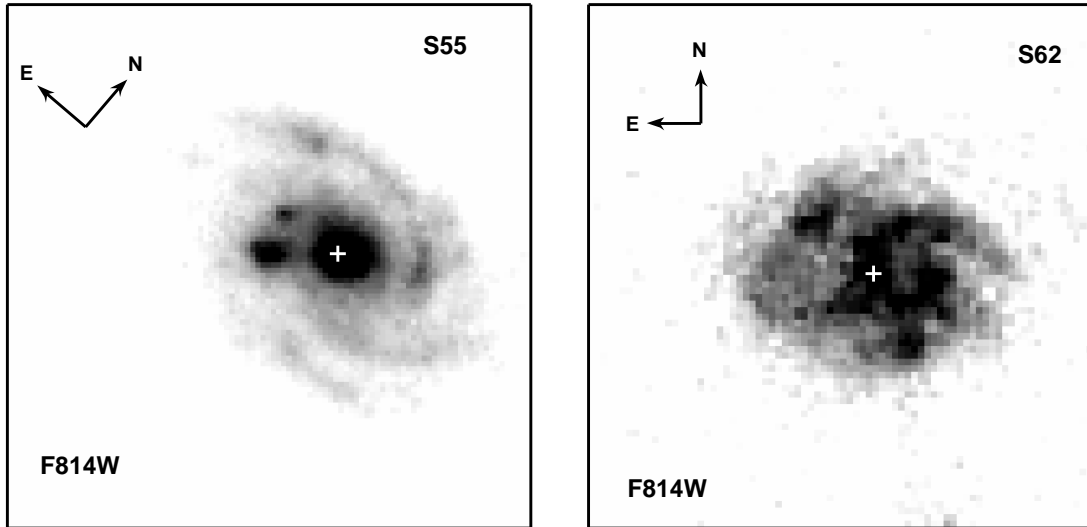
Figure 4.2 — F814W image of S55 and S62. Image size is $4'' \times 4''$. The image size, position and orientation are identical to the final SINFONI FOV. The white plus marks the position of the center according to the FIRES catalog (S55, Labbé et al. 2003) or HDF-S flanking field catalog (S62, Lucas et al. 2003). The grey scales were chosen so that the complex structure is well visible.

circumstances, we decided not to use the first 1hr45min of data of S55. One OB of S55 was observed with a different position angle. We rotated this data before we made the final, psf weighted average of all frames.

4.5 Results

4.5.1 SINFONI results - Discussion of individual sources

S55.   The F814W image of S55, see Fig. 4.2a, shows a bulge, spiral arms and a few star forming knots, the brightest just south-east of the center. Not shown in Fig. 4.2a (that shows the SINFONI FOV), is the smaller 'companion'. Contrary to the statement of Franceschini et al. (2003), this is not an interacting pair. The small elliptical galaxy has a different redshift (Vanzella et al. 2002). We estimate the inclination from the F814W image and find $49 \pm 5°$.

We integrated for 3hrs30min on source and found Hα, [N II]λ6583/6548 and [S II] λ6717/6731 at the expected redshift ($z = 0.76$). Line fluxes and line ratios are given in Table 4.2. The line ratios are consistent with star formation as only ionization source. The derived SFR, 6 M$_\odot$ yr^{-1}, is consistent with previous estimates (Franceschini et al. 2003 and references therein). We derive a VF and discuss it in Sect. 4.6.1.

S62.   The F814W image from the HDF-S flanking fields (Lucas et al. 2003) of S62 shows a complex structure, see Fig. 4.2b. Several star forming knots are visible, and there is a hint of spiral structure. We estimate the inclination from the F814W image and find $43 \pm 5°$.

After integrating 3 hours, we detect Hα, [N II]λ6583/6548 and [S II]λ6717/6731 at

Table 4.2.   Emission line fluxes, line ratios and SFRs. The fluxes are in units 10^{-16} erg s^{-1} cm^{-2} and the SFRs have units M$_\odot$ yr^{-1}. Values between parentheses suffer from severe OH line contamination.

ID	Hα	[N II]λ6583	[N II]λ6548	[S II]λ6717	[S II]λ6731	[N II]λ6583/Hα	([S II]λ6717 + λ6731)/ Hα	SFR$_{H\alpha}$
S55	1.68 ± 0.05	0.30 ± 0.05	$(0.2) \pm 0.1$	0.2 ± 0.1	0.1 ± 0.1	0.18 ± 0.03	0.2 ± 0.1	6
S62	6.1 ± 0.1	2.3 ± 0.2	1.6 ± 0.5	1.3 ± 0.5	0.7 ± 0.5	0.38 ± 0.03	0.3 ± 0.1	18

$z = 0.70$, see Table 4.2. The line ratios integrated over the entire galaxy are listed in Table 4.2 and indicate star formation as the source of ionization.

Franceschini et al. (2003) give a redshift of 0.73 for this source. We checked the low resolution ISAAC observations of Rigopoulou et al. (2000) and concluded that they probably confused the [S II] lines with Hα+[N II]. The wavelength and flux of their emission line is in agreement with our estimates for the [S II] line. The flat field of ISAAC declines fast towards shorter wavelengths, and this might be the reason they missed the Hα line. This also increases the estimate of the Hα SFR from 6.4 $M_\odot$ yr^{-1} (Franceschini et al. 2003) to 18 $M_\odot$ yr^{-1} (both values are uncorrected for extinction). We derive a VF and discuss it in Sect. 4.6.2.

S43. The redshift of S43 as given by Franceschini et al. (2003) which was taken from Rigopoulou et al. (2000) is 0.95. However, S43 was also observed by Vanzella et al. (2002, their id is 789) who find $z = 1.116$. We find evidence for Hα at neither redshift. It might be too faint to detect in 2hrs, S43 is ~ 1.5 mag fainter in Js than S55 and S62.

4.5.2 SED fitting

To get more insight in the nature of these galaxies and to be able to study the stellar mass TFR, we fitted the SEDs of the galaxies in our sample, the additional sample and companion galaxies following the method of Wuyts et al. (2007). In short, we fit Bruzual & Charlot (2003) models with Salpeter IMF, $0.1 - 100$ $M_\odot$ mass range, solar metallicity and three different star formation histories (delta burst, exponentially decreasing SFR with e-folding time 300 Myr, continuous star formation) to the best SED of each galaxy (see below for specification of best SED). For the latter two star formation histories, we allowed extinction following the Calzetti et al. (2000) law with A_V between 0 and 4. Best fit stellar masses, SFRs, ages and A_Vs are listed in Table 4.3. Stellar masses can be derived more reliably than SFR, age and A_V, and the format fit errors for these parameters may be unrealistically small. Therefore we only give the fitting errors for the stellar masses. The best fit values for SFR, age and A_V should be interpreted as indications for the true values.

The best SEDs of each galaxy were chosen as follows. When possible, we prefer an SED from the FIRES data as the photometry was measured consistently over a large wavelength range (UBRIJHK+IRAC) (Labbé et al. 2003, 2005). Second choice is the EIS UBVRIJHK photometry given by Franceschini et al. (2003) (if possible combined with FIRES IRAC data) to get the cleanest comparison with the stellar masses derived by Franceschini et al. For multiple component sources, Franceschini et al. (2003) do not fit all components. In that case, we looked up the EIS UBVRIJHK photometry of the individual component in da Costa et al. (1998) and combined this with IRAC photometry from FIRES if possible. We visually checked the best fit results for different SEDS for all sources. This means that we used the following SEDs for individual sources:
- For S27, S43, S53a and S53b, we used FIRES data over the full wavelength range.
- S55 falls just outside the FIRES U and B band image. The Balmer/4000Å-break is however between R and I band, therefore the parameters derived from SED fitting should still be reliable. When we compared the FIRES and Franceschini SEDs, we noted that there is a systematic offset between the two SEDs. The best fit parameters vary only

Table 4.3. Results from SED fitting. Stellar masses have units $10^{10}M_\odot$, SFRs have units $M_\odot$ yr^{-1} and ages have units Gyr. The extinction corrected SFRs were corrected with the A_V estimate from the Balmer decrement when available, and A_V from SED fitting from Franceschini et al. otherwise. Note that the SED for S62 from Franceschini et al. was done with $z = 0.73$ instead of $z = 0.70$ and the SED fit for S43 for $z = 0.95$ instead of 1.12. Also, S53a and S53b are not resolved in the EIS catalog, so the Franceschini et al. SED fit for S53a includes also S53b. See text for specification of the precise SED used for each source for the Wuyts et al. method for SED fitting.

ID	M_* Wuyts	M_* Franceschini	SFR$_{\rm SED}$ Wuyts	SFR$_{\rm SED}$ Franceschini	SFR$_{H\alpha}$ this work/Franceschini	SFR$_{H\alpha}$ ext. corr.	age Wuyts	A_V Wuyts	A_V Franceschini	A_V Balmer
S43	$5.3^{+0.02}_{-0.4}$	5.0^{+5}_{-3}	30	58	—		0.64	1.8	2.4	
S55	$4.7^{+0.5}_{-0.02}$	13.0^{+3}_{-7}	44	45	6	36	0.51	1.8	1.8	2.6
S62	$1.9^{+0.7}_{-0.1}$	$6.6^{+2.4}_{-0.31}$	24	37	18	47	1.02	1.2	1.4	—
S14	$1.6^{+0.01}_{-0.1}$	$3.2^{+0.8}_{-1.2}$	5	10	—		0.81	0.4		
S23a	$6.5^{+0.7}_{-0.1}$	$9.7^{+5.3}_{-5.5}$	37	50	> 1.5	> 5	0.64	2.8	2.4	
S25a	$2.9^{+0.3}_{-0.02}$	8.0^{+4}_{-3}	62	56	4	17	0.32	2.2	2.1	
b	$1.4^{+0.9}_{-0.1}$		35				0.29	1.2		
S27	$15.8^{+0.03}_{-0.07}$	47.0^{+10}_{-8}	185	45	7	23	0.45	2.2	2.0	1.7
S53a	$2.7^{+0.8}_{-0.9}$	12.0^{+3}_{-2}	80	39	13	55	0.40	1.6	1.4	2.1
b	$0.4^{+0.01}_{-0.1}$		3				1.9	0.6		

slightly. We therefore choose to use the FIRES RIJHK+IRAC SED.

- S62 en S14 fall outside the FIRES area. We therefore use the UBVRIJHK SED from Franceschini et al. (2003).

- For S23abc we have EIS UBVRIJHK and FIRES IRAC photometry. Franceschini et al. identify S23b as the source of the $15µm$ emission (see their appendix) but when we compare the coordinates and SED of their S23, they have fitted the SED of S23a. As Puech et al. (2008) observed the VF of S23a, we are mainly interested in the SED of S23a. The quality of the SED fit is poor. We use the results from the Franceschini + IRAC photometry, but note that the stellar mass estimate is probably not as reliable as that of the other sources.

- For S25ab, we have JHK+IRAC photometry from FIRES. Franceschini et al. (2003) identify S25a as the source of the $15µm$ emission and the coordinates and photometry of their S25 source are consistent with those of S25b. Although S25a is the brighter source, S25a and S25b are clearly detected in IRAC. Because there is kinematic data for both, we use both in our analysis. For S25a, we combine the EIS UBVRIJHK photometry from Franceschini et al. with the FIRES JHK+IRAC photometry for the SED fit (the JHK fluxes from EIS and FIRES catalogs are consistent). For S25b, we use EIS UBVRIJHK photometry from da Costa et al. and JHK+IRAC photometry from FIRES. There is a slight offset between the EIS and FIRES JHK fluxes. We checked the mass estimates from the other sources using different input SEDs and estimate the offset between the JHK fluxes results in $\lesssim 10\%$ overestimate of the stellar mass of S25b.

Franceschini et al. (2003) also fitted the UV+optical+nearIR+ISO SEDs of this sample using a method specially devised to model dusty starbursting galaxies. They fit the SED of the galaxy with a combination of 10 single stellar populations with different age and extinction. The single stellar populations have the same IMF as the model from Wuyts et al. (2007). Their best fit stellar masses and, SFRs and A_Vs are also listed in Table 4.3. Franceschini et al. (2003) did not fit the companion galaxies. In particular, for S25 which appears to be an interacting pair of similar mass and size galaxies, they only fitted the brightest galaxy of the two (S25a, see also Sect. 4.6.3).

The stellar masses derived by Franceschini et al. (2003) are larger than the stellar masses derived using the method of Wuyts et al. (2007). The reason the Franceschini et al. masses are larger than the Wuyts et al. (2007) masses is probably that the Franceschini et al. method allows a substantial amount of mass in the older stellar populations that contribute relatively little to the integrated light. Wuyts et al. (2007) find for $z > 2$ galaxies that their stellar masses are ~ 2 times larger if they fit a combination of a maximally old population and a recent starburst instead of exponentially decreasing star formation histories. Although Franceschini et al. (2003) do not specify the masses per single stellar population, their method naturally includes this maximally old population.

We also list in Table 4.3 the SFRs from Hα with and without extinction correction. After extinction correction, the SFRs from Hα are of the same order as the SFRs from SED fitting.

Finally, for a few targets, Hα and Hβ fluxes have been measured and a direct measure of the extinction using the Balmer decrement (Franceschini et al. 2003) is available.

The A_Vs found using this method are in rough agreement with the A_Vs from SED fitting (see Table 4.3).

4.6   Velocity fields and rotation curves

We measured the VFs using the method described in van Starkenburg et al. (2008a) for our best case. In short, the S/N of individual spectra is poor, and automatic fitting routines easily confuse emission lines with OH line residuals. Therefore, the VFs are derived from manually fitting gaussians to the Hα line at every spatial position. For S55 and S62, we also binned the spectra spatially to $0\overset{\prime\prime}{.}25 \times 0\overset{\prime\prime}{.}25$ pixels to increase the S/N of the individual spectra.

We derive a RC by modeling the VF using the same method as described in van Starkenburg et al. (2008a). In short, we fit tilted ring models to the VFs observed using GIPSY (van der Hulst 1992, Vogelaar & Terlouw 2001). Parameters for each ring are the center, position angle, inclination, systemic velocity, expansion velocity and the rotation velocity. This number of parameters is too large for the number of independent data points. Therefore, we fix the center, position angle and inclination to those of the F814W image, the systemic velocity to the velocity of the center pixel and the expansion velocity to zero. This leaves only the rotation velocity as free parameter for each ring. After a successful fit, we refit the model, leaving a second free parameter. If the best fit gives consistent values for this second parameter and it is different from the default value, we fix the value of this parameter to the new value and continue with the next parameter, until none of the parameters changes anymore.

We emphasize that the observed RC derived using this method may be different from the intrinsic RC. The observed RC is smoothed by seeing, and because we do not know the Hα distribution at high spatial resolution, we cannot exclude that certain velocities are emphasised due to peaks or gaps in the Hα surface brightness. We have attempted to model these effects for our best case, and found that even for that case it is very hard to model these effects and derive the intrinsic rotation curves, except for the flat rotation curve velocity (van Starkenburg et al. 2008a). The quality of the SINFONI observations is significantly poorer for these galaxies. Therefore, we present in this paper only the observed RC without a model for the seeing and the intrinsic Hα distribution.

For our best case, HDF-S 257, observed in K band, we were also able to measure the velocity dispersion field (van Starkenburg et al. 2008a). For the J band data, the spectral resolution is too small to measure the velocity dispersion.

We will now discuss the VFs and RCs of the galaxies that we observed with SINFONI. In Sect. 4.6.3, we will briefly discuss the VFs of ISO galaxies observed by others.

4.6.1   S55

The observed VF is shown in Fig. 4.3a on page 110. The VF is quite noisy, partially due to OH line residuals. We fitted tilted ring models to the VF as described above. The best fit model and the residuals from the model are shown in Fig. 4.3b and c on page 110. Although the VF is quite noisy, we were able to derive the center and (roughly
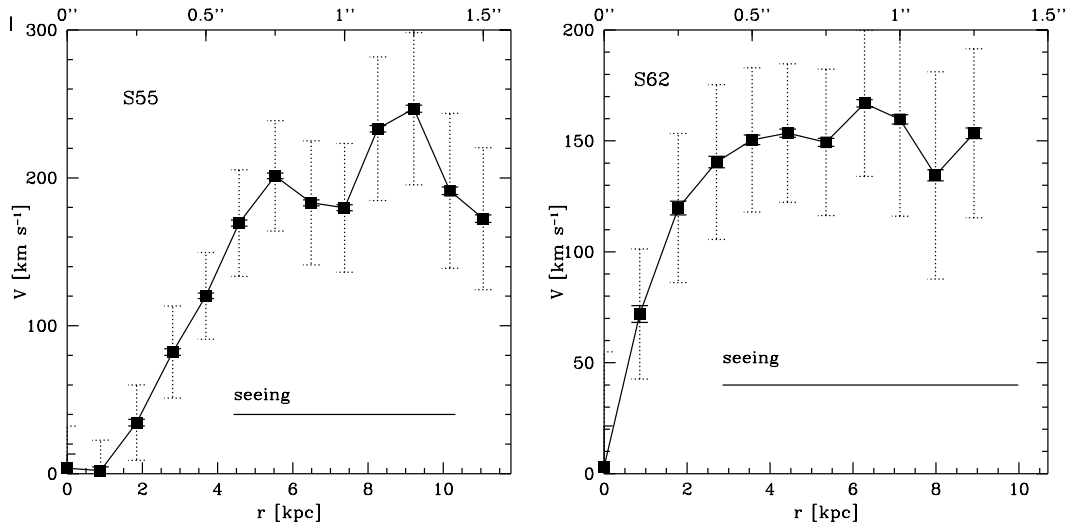
Figure 4.4 — RCs of S55 and S62. The full error bars give the formal fitting error to the velocities as given by GIPSY. The dotted error bars indicate the scatter in the observed values.

the) PA from the VF and both are consistent with the values derived from the F814W imaging. There are no systematic residuals from a rotating disk.

The RC of the best fit model is shown in Fig. 4.4a. It rises to ~ 200 km s^{-1} and then stays more or less flat. We refitted the VF with slightly different values for the inclination, centre, position angle and systemic velocity but this has little effect on the fitted RCs. However, we have not taken into account the seeing of $\sim 0\overset{''}{.}8$ which has significant effect on the derived RC and could lead to an underestimate of the rotation velocity. This seeing is considerably worse than for our other SINFONI observations (van Starkenburg et al. 2008a, 2008b). For our best case HDF-S 257 (see van Starkenburg et al. 2008a), we modeled the effects of seeing on the derived RC and estimated that the seeing resulted in less than 5% underestimate of V_{flat}. However, this galaxy has slightly smaller scale length and similar size as S55 and was observed with $0\overset{''}{.}5$ seeing. To quantify the amount by which we underestimate the true rotation velocity for S55 (and S62, which was observed in similar conditions), we made a toy model RC that rises linearly to radius R_{flat} and then remains constant until the last observed point. For different values of R_{flat}, we made model VFs. Using the F814W flux distribution and PSF of S55, we made 'observed velocity fields' and 'observed rotation curves'. We find that for $R_{flat,model} \lesssim 0\overset{''}{.}5$, $V_{flat,observed}$ is underestimated by $\sim 20\%$ at $R_{obs} = 1''$. Given the observed R_{flat} and the seeing for both S55 and S62, we can safely assume that $R_{flat,model} < 0\overset{''}{.}5$, and apply a 20% correction factor. We then get $V_{flat} \sim 250 \pm 50$ km s^{-1}. This value for the rotation velocity is consistent with the velocity derived by Rigopoulou et al. (2002) using ISAAC in medium resolution mode: $V_{flat} = 270 \pm 75$ km s^{-1}.

4.6.2   S62

After binning to $0\overset{''}{.}25$ pixels we derive the VF shown in Fig. 4.5 on page 111. Even after binning, the S/N of the Hα line is still poor and this contributes significantly to the

noise in the derived VF, especially on the east side of the galaxy. The west side of S62 is also brighter in the F814W image.

We fitted a tilted ring model to the VF as described above. The PA is roughly confirmed from the VF. The best fit systemic velocity is slightly different from the velocity of the center pixel, but within expected ranges from the noise in the VF and the velocity gradient observed. We were not able to derive other parameters from the VF. The best fit VF (with default parameters except for the systemic velocity), and the residuals from the model are shown in Fig. 4.5 on page 111. Although noisy, there are no systematic deviations from a rotating disk.

The RC of the best fit VF is shown in Fig. 4.4b. The distance between the point where the RC flattens in the receding and approaching halves is about one seeing element. Therefore, R_{flat} is not resolved. We repeated the fit for slightly different values for the parameters of the fit, and conclude this has little effect on the RC found. We also fitted the receding and approaching half of the VF separately, and found a similar RC for both halves. In all cases, the RC rises steeply to $\sim 150 \pm 20$ km s^{-1} and then remains flat until the largest observed radius of $\sim 1\rlap{.}''25$. Given the seeing and the models described in the previous subsection, we estimate that the true velocity is $V_{flat} = 190 \pm 30$ km s^{-1}.

4.6.3 VFs and RCs of other ISO targets

We will now discuss the VFs and RCs of the ISO targets observed by Rigopoulou et al. (2002) and Puech et al. (2008). A summary of all IDs, redshifts, observed lines and rotation velocities may be found in Table 4.1.

S14. S14, at $z = 0.41$, was observed by Puech et al. (2008 and references therein). It is viewed almost face-on ($i \sim 36°$) and they estimate its rotation velocity to be $V_{flat} = 220 \pm 53$ km s^{-1}. Puech et al. (2008) divide their sample intro three subsamples: rotating disks, perturbed rotators and complex kinematics. Rotating disks are characterized by a VF consistent with rotation and a peak in the velocity dispersion field, and are consistent with being relaxed rotators. Perturbed rotators show some weak deviations from this pattern. Galaxies with complex kinematics are dynamically not relaxed and are likely associated with mergers. They classify the VF of S14 as kinematically complex.

S23. S23 is likely a triple system, separated by $3\rlap{.}''5$ and $6\rlap{.}''1$ (20 and 36 kpc respectively at the redshift of the source) from SW to the NE component (labeled 'a', 'b' and 'c' respectively). The redshifts of the center and SW components have been measured to be 0.46 (Rigopoulou et al. 2000, Puech et al. 2008) and the photometric redshift of the NE component is consistent with this redshift ($z_{phot} = 0.70$, range $0.45 - 0.98$, redshift obtained with EAZY photometric redshift code from Brammer et al. 2008).

Franceschini et al. (2003) assumed that the center component is the brightest $15 \mu m$ source. The SW component is however much brighter in the IRAC imaging than the two other components. Therefore, we take the SW component as the ISO source.

Puech et al. (2008) observed the VF of the SW component, for which the F814W

image reveals a small object close to the main galaxy. They classify it as a rotating disk galaxy with $V_{flat} = 230 \pm 37$ km s^{-1} (corrected for its inclination of 51°). They do not detect [O II] emission for the small object, nor a disturbance of the VF near the position of the small object.

S53. S53 is an interacting system. The velocity difference between the two galaxies is ~ 500 km s^{-1} and the larger galaxy shows a circum-nuclear ring caused by the previous encounter with the smaller galaxy (Franceschini et al. 2003). The morphology of the larger galaxy was classified as peculiar/merger by Neichel et al. (2008). Puech et al. (2008 and references therein) derive its VF and classify it as kinematically complex with $V_{flat} = 130 \pm 69$ km s^{-1}. The smaller galaxy S53b does not fall inside their FOV.

S25. S25 is a interacting pair of galaxies of similar size and mass at $z = 0.58$ separated by 2″46 (which corresponds to 16.2 kpc at this redshift). They were observed in the same slit by Rigopoulou et al. (2002) who find $V_{flat} = 260 \pm 45$ km s^{-1} and $V_{flat} = 249 \pm 52$ km s^{-1} after correcting for inclination $i = 65°$ for the NE and SW galaxy respectively (named S25a and S25b respectively in this paper).

Franceschini et al. (2003) assume that the ISO 15μm flux is associated with the brightest galaxy, to which we refer as S25a. We checked the IRAC photometry of both galaxies and both are detected in all four IRAC bands. S25a is only ~ 2 times brighter than S25b. We therefore take into account both galaxies in our analysis.

S27. The F814W image of S27 shows a bulge and spiral structure with star forming regions. It is remarkably large (FWHM of Hα is $\sim 4''$ or 26 kpc) and massive: Rigopoulou et al. (2002) derive an (inclination 49° corrected) flat RC velocity of 460 ± 40 km s^{-1}.

4.7 Masses

We calculated the dynamical massed using

$$M_{dyn} = \frac{v^2 r}{G} \tag{4.1}$$

where v is the best estimate of the rotation velocity and r is the maximum observed radius of the RC. The dynamical masses are listed in Table 4.4. We also calculated the dynamical masses for the Rigopoulou et al. (2002) sources from data in their paper. Dynamical masses for the last three sources were taken from Puech et al. (2006). These masses are also listed in Table 4.4.

We also list the stellar masses from SED fitting determined by the method from Wuyts et al. (2007) and Franceschini et al. (2003) in Table 4.4 (see Section 4.5.2 for an explanation of the different methods).

We estimated the gas masses for the targets with SINFONI spectra, S55 and S62, using the global Schmidt law which relates SFR and surface density of the gas (Kennicutt 1998). This relation has considerable scatter, but there is some evidence it is also valid at high redshift (Bouché et al. 2007). We did not attempt to calculate gas masses for other targets. Puech et al. (2008 and references therein) did not observe Hα and

Table 4.4 — Masses and mass ratios. The dynamical mass estimates from the sources observed by Rigopoulou et al. (2002) were calculated from the extent of the RC in their figures 2,3 and 4. We did not use the values in their table 3 as the physical scales in their table 2 are not consistent with their assumed cosmology as stated in their Section 1. The dynamical masses of the sources observed by Puech at al. (2008) were taken from Puech et al. (2006) (their Table A.1 and corrected for the slightly different method). Gas masses between parentheses are extinction corrected gas masses. Note that the stellar mass estimate for S23a is less reliable than for the other galaxies (see Sect. 4.5.2). All masses are in units 10^{10} M$_\odot$.

ISO ID	M_{dyn}	M_* Wuyts	M_* Franceschini	M_{gas}	M_*/M_{dyn} Wuyts	M_*/M_{dyn} Franceschini
S55	16	4.7	13.0	0.6 (3.1)	0.3	0.8
S62	7.5	1.9	6.6	1.2 (2.5)	0.3	0.9
S14	6.3	1.6	3.2	—	0.3	0.5
S23a	7.1	6.5	9.7	—	0.9	1.4
S25a	16	2.9	8.0	—	0.2	0.5
b	14	1.4	—	—	0.1	—
S27	65	15.8	47.0	—	0.2	0.7
S53a	1.5	2.7	12.0	—	1.8	8
S55	16	4.7	13.0	—	0.3	0.8

Franceschini et al. (2003) only for part of the sample. Moreover, Franceschini et al. (2003) do not give the area over which they detect Hα.

There is no evidence for dark matter within the observed radii if we take the stellar masses from Franceschini et al. (2003). Using the masses from Wuyts, the stellar-to-dynamical mass ratios are ~ 0.3. The gas masses of S55 and S62 suggest that they are large enough to result in $M_{bar}/M_{dyn} \sim 1$.

4.8 Tully-Fisher relations

4.8.1 Rest frame B and K band TFR

Rest frame B magnitudes were calculated by interpolating between the two closest observed bands from the FIRES data. Two sources fall outside the FIRES area, and for those sources we used EIS photometry. EIS and FIRES results may differ by ~ 0.5 mag. These sources have an open symbol in Fig. 4.6a.

The rest frame B band TFR is shown in Fig. 4.6a together with the local TFR of Verheijen (2001). All galaxies are consistent with or are less luminous than expected from the local TFR. We indicated how the positions would change if an A_V correction is applied. After extinction correction, all galaxies are consistent or brighter than expected from the local TFR. Offsets from the local TFR seem to increase with decreasing mass, which is consistent with observations of others (e.g. Puech et al. 2008, Böhm et al. 2004) and model expectations (e.g. van Starkenburg et al. 2006).

The rest frame K band TFR is shown in Fig. 4.6b together with the local TFR of Verheijen (2001). Rest frame K band magnitudes were calculated using the IRAC photometry of the FIRES field. The rest frame K band magnitude of the two sources outside the FIRES field were taken from Puech (2008) and estimated from the continuum fit of
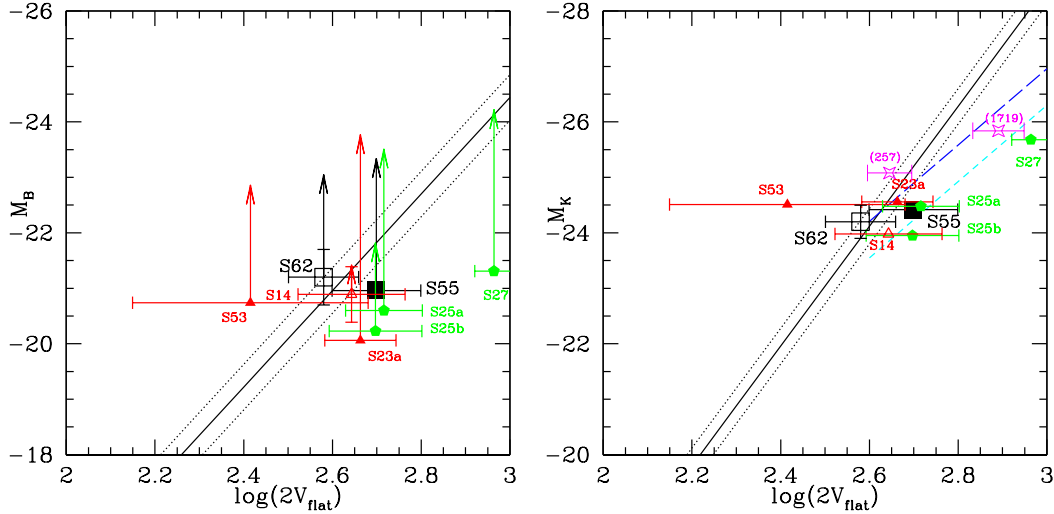
Figure 4.6 — Rest frame B and rest frame K band TFR. The local TFRs and its scatter (full and dotted lines) are from Verheijen (2001). We show also the rest frame K band TFR from Puech et al. (2008) for $z = 0$ (long dashed (blue) line) and $z = 0.6$ (short dashed (cyan) line). Black squares refer to velocities derived in this paper, (red) triangles are velocities from Puech et al. (2008) and the (green) pentagons are from Rigopoulou (2002). For comparison, we show also the position of two of our $z \sim 2$ sources by thin (magenta) stars with IDs between parentheses (see van Starkenburg et al. 2008a, 2008b for more information about these sources). Absolute magnitudes calculated from the FIRES data are indicated with full symbols, magnitudes calculated from other sources by open symbols. The other sources are: EIS photometry (rest frame B magnitudes), taken from Puech et al. (2008) (S14, rest frame K - the difference between the absolute K magnitude from Puech et al. and ours is < 0.1mag for the other two Puech sources) and estimated from the continuum fit shown in Fig. A.1 of Franceschini et al. (2003). The arrows indicate where the points would lie after extinction correction using the A_V from Wuyts. We labeled each points with its ISO id to facilitate tracking the individual sources through the diagrams.

Franceschini et al. (2003). The rest frame K band TFR shows much less scatter than the rest frame B band TFR. Our galaxies are consistent with or slightly less luminous than expected from the local TFR, except S27 which is much less luminous than the local TFR. Interestingly, we found a similarly massive galaxy in our $z \sim 2$ sample which is also relatively less luminous (van Starkenburg et al. 2008b). S27 is also consistent with the $z \sim 0.6$ TFR of Puech et al. (2008) which has a different slope than the Verheijen (2001) TFR and is also shown in Fig. 4.6b. The other data points are close to the point where the two local TFRS cross. The weighted average offset from the local TFR of Verheijen (2001) is 0.53 mag (excluding S53 and S27) while the 1σ scatter in the local relation is 0.32 mag. This offset is consistent with the offset found by Puech et al. (2008), who find an average offset of 0.66 mag from the local rest frame K band.

In our $z \sim 2$ sample, there is also one very massive galaxy (MS1054 1719) that is also underluminous compared to the local relation (van Starkenburg et al. 2008b). Our most reliable $z \sim 2$ point is slightly brighter than expected from the local TFR. We show both points also in Fig. 4.6b.
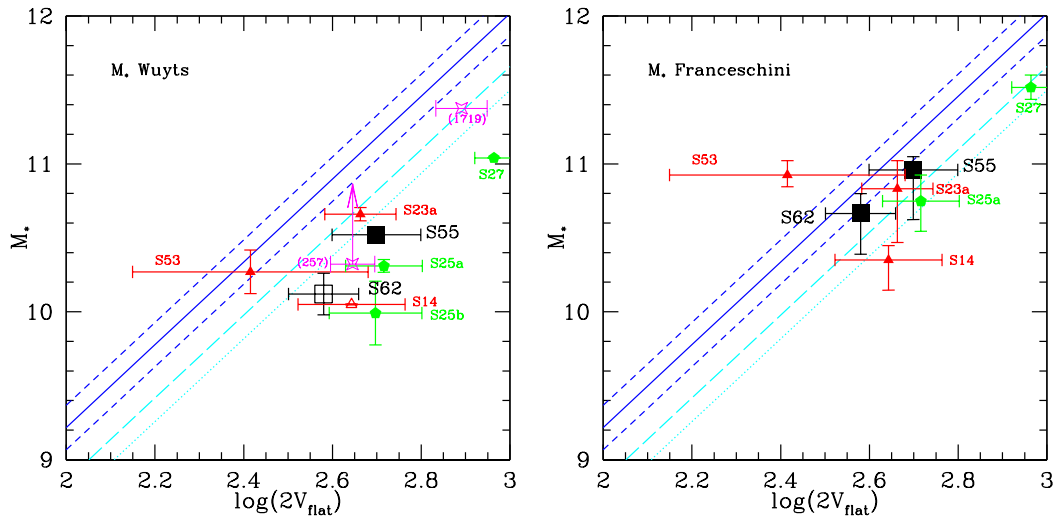
Figure 4.7 — Stellar mass TFR, using the stellar masses from Wuyts or Franceschini (as indicated in the figures). The local stellar mass TFR and its 1σ scatter were taken from Puech et al. (2008) and is shown as the full and dotted (blue) lines. Their best fit $z \sim 0.6$ relation is shown by the (cyan) long dashed line. Their estimate of the $z \sim 0.6$ stellar mass TFR using mass estimates from fitting Bruzual & Charlot models instead of the Bell et al. (2003) M_*/L_K method is shown by the (cyan) dotted line. Coding of the data points is the same as in Fig. 4.6. For the Wuyts et al. masses, full symbols indicate masses derived from SEDs including IRAC photometry and open symbols indicate masses derived from SEDs without IRAC photometry (the masses of the $z \sim 2$ sources are derived using UV+optical+nearIR+IRAC photometry). The $z \sim 2$ The arrow of the (257) points indicates how it would shift if a maximally old population is added.

4.8.2 Stellar mass TFR

As we found systematic differences between the stellar mass estimates using the method from Wuyts et al. (2007) and Franceschini et al. (2003), we show the stellar mass TFR for both mass estimates in Fig. 4.7a and Fig. 4.7b respectively. Note that the stellar mass TFR with stellar masses from Franceschini does not include S25b. S53 shows not significant offsets from the general trend due to the large uncertainty in the velocity estimate. We do not take into account S53 in the discussion below. The other galaxies appear to form a TFR for both mass estimates, although the zero-point depends on the stellar mass estimate method.

We take the $z = 0$ and $z = 0.6$ stellar mass TFRs of Puech et al. (2008) for [O II] emitting galaxies as comparison TFRs. The $z = 0$ relation is very similar to the local stellar mass TFR of Pizagno et al. (2005) that we used in our previous papers (van Starkenburg et al. 2008a, 2008b). Puech et al. (2008) found 0.36 dex evolution from $z = 0$ to $z = 0.6$ and estimate that after correction for systematic errors, the true evolution is ~ 0.46 dex. We corrected the stellar masses to 'diet Salpeter' IMF masses (correction factor is 0.7) for comparison with the Puech et al. (2008) results. Using the Wuyts masses, we find stronger evolution than Puech et al. (2008) found: average offset is 0.81 dex with respect to the $z = 0$ relation of Puech et al. For the Franceschini et al. masses, the stellar mass TFRs is consistent with the Puech et al. (2008) result (average offset is 0.36 dex with respect to $z = 0$).

We find different evolution for our sample using two different methods to estimate the stellar masses. This differences probably originates from the allowed star formation histories. Massive old stellar populations that contribute little to the observed light are naturally incorporated in the Franceschini et al. method. These different results illustrate the need for well calibrated stellar masses. Differences arise also when different stellar evolution models are used (e.g. the Maraston models, see Wuyts et al. 2007).

Puech et al. (2008) estimate their stellar masses using the B-R color of their galaxies and associated M_*/L_K of Bell & de Jong (2003). They estimate that they would have found 0.16 dex more evolution if they had used Bruzual & Charlot models, as our fitting procedure does. The total evolution in the stellar mass TFR using Bruzual & Charlot models is then 0.52 dex for the Puech et al. sample. It would be better to compare our results to a local stellar mass TFR that also uses the SEDs over a large wavelength range to obtain stellar masses. We have searched for such reference stellar mass TFRs, but have not found any. Most use the B-R color plus M/L_K conversion of Bell & de Jong (2001, 2003) or a similar prescription. These relation are well calibrated for local galaxies and their typical ages, star formation histories and dust content. Full SED modeling takes into account differences in typical ages, star formation histories and dust content.

Given the errors on velocity and stellar mass and the uncertainty in the zero-points of the different relations, both the Franceschini and the Wuyts method are consistent with the Puech et al. (2008) results. Although the samples were selected with different selection criteria, the TFRs are consistent. This confirms that our infrared-based selection provides samples that are suitable for TFR studies.

We also show in Fig. 4.7a two of our $z \sim 2$ galaxies. Although the number of galaxies is very small, there is no trend toward stronger evolution for $z \sim 2$ galaxies.

Interestingly, this evolution in the stellar mass TFR was not predicted by simulations of disk galaxy formation. Portinari & Sommer-Larsen (2007) predict that individual galaxies move along the stellar mass TFR so that the stellar mass TFR does not evolve.

4.9   Summary and conclusions

We observed three ISO 15μm detected galaxies from the Franceschini et al. (2003) sample of ISO 15μm emitting galaxies in the HDF-S. We detect emission lines in two of them, and the [N II]/Hα and [S II]/Hα ratios are consistent with star formation as only ionizing source.

Rigopoulou et al. (2002) obtained long slit spectroscopy of three ISO sources. They concluded that the derived RCs are consistent with these galaxies being massive rotating disks. We confirm this result from our derived VFs.

We combine the rotation velocity measurements of galaxies from the Franceschini et al. (2003) sample from this work, the work of Rigopoulou et al. (2002) and Puech et al. (2008) to study the rest frame B and K band TFR and the stellar mass TFR of $z \sim 0.7$ 15μm emitting galaxies. We find that the results for the rest frame B band TFR strongly depend on the extinction correction which is large for this sample. The rest frame K band TFR shows less scatter and the galaxies are on average 0.53 magnitude

less luminous than expected from the local TFR. This is consistent with the findings of Puech et al. (2008). The most massive galaxy is 2.4 ± 0.5 mag offset from the local relation. A similarly massive $z \sim 2$ galaxy showed a similar offset (van Starkenburg et al. 2008b).

The stellar mass TFR appears to exist at $z \sim 0.7$. The offset from the local stellar mass TFR depends however strongly on the method that was used to derive the stellar masses. We find 0.81 and 0.36 dex offset for stellar masses using the method of Wuyts et al. (2007) and Franceschini et al. (2003) respectively. Both are consistent with the [O II] emitters TFR at $z \sim 0.6$ of Puech et al. (2008) after correction for the different method used for fitting the stellar masses. The main difference between the Wuyts et al. (2007) and Franceschini et al. (2003) methods for estimating the stellar mass are the allowed star formation histories.

Acknowledgements

References

Bell, E.F. & de Jong, R.S., 2001, ApJ 550 212

Bell, E.F., McIntosh, D.H., Katz, N. & Weinberg, M.D. 2003 ApJ149 289

Böhm, A., Ziegler, B.L., Saglia, R.P. et al 2004 A&A 420 97

Bonnet, H. et al. 2004, The ESO Messenger 117, 17

Bouché, N. Cresci, G., Davies, R. et al. astro-ph 0706.2656

Brammer, G.B., van Dokkum, P. G. & Coppi, P. 2008 arXiv 0807.1533

Bruzual, G. & Charlot, S. 2003, MNRAS 334 1000

Calzetti, D., Armus, L., Bohlin, R.C. et al. 2000 ApJ 533 682

Courteau, S., Dutton, A.A., van den Bosch, F.C. et al. 2007, ApJ 671 203

da Costa, L., Nonino, M., Rengelink, R. et al. 1998 astro-ph 9812105

Eisenhauer, F. et al. 2003, SPIE 4841, 1548

Franceschini, .A., Berta. S, Rigopoulou, D. et al. 2003 A&A 403 501

Kennicutt, R.C. 1998, ApJ 435 22

Labbé, I., Franx, M., Rudnick, G. et al. 2003 AJ 125 1107

Labbé, I., Huang, J., Franx, M. et al. 2005 ApJ 624 81

Lucas, R.A., Bauw, S.A., Brown, T.M. et al. 2003 AJ 125 398

Modigliani, A., Hummel, W., Abuter, R. et al. 2007 arXiv:astro-ph 0701297

Neichel, B., Hammer, F., Puech, M. et al. 2005 A&A ... arXiv 0803.2370

Pizagno, J., Prada, F., Weinberg, D.H. et al. 2005 ApJ 633 844

Portinari, L. & Sommer-Larsen, J. 2007, MNRAS 375 913

Puech, M., Hammer, F., Flores, H., Östlin, G. & Marquart, T. 2006 A&A 455 119

Puech, M., Flores, H, Hammer, F. et al. 2008 A&A arXiv:0803.3002

Rigopoulou, D., Franceschini, A., Aussel, H. et al. 2000 ApJ 537 L85

Rigopoulou, D., Franceschini, A., Aussel, H. et al. 2002 ApJ 580 789

Tully, R. B. & Fisher, J. R. 1997 A&A54 661

van der Hulst, J.M., Terlouw, J.P., Begeman, K., Zwitser, W. & Roelfsema, P.R. "The Groningen Image Processing System, GIPSY", in: Astronomical Data Analysis Software and Systems I, (eds. D. M. Worall, C. Biemesderfer and J. Barnes), ASP Conf. series no. 25, p. 131, 1992

van den Bosch, F.C. 2000 ApJ 530 177

van Dokkum, P.G., 2001, PASP, 113, 1420

van Starkenburg, L., van der Werf, P.P., Yan, L. & Moorwood, A.F.M. 2006 A&A 450 25 (Chapter 2)

van Starkenburg, L. van der Werf, P.P., Franx. M et al. 2008a A&A 488 99 (Chapter 3)

Van Starkenburg, L. et al. 2008b in prep. (Chapter 5)

Vanzella, E., Cristiani, S., Arnouts, S. et al. 2002 A&A 396 847

Verheijen, M. A. W., 2001, ApJ 563 694

Vogelaar, M.G.R. & Terlouw, J.P. "The Evolution of GIPSY, or the Survival of an Image Processing System", in: Astronomical Data Analysis Software and Systems X, (eds. F. R. Harnden, Jr., F. A. Primini & H. E. Payne), ASP Conf. series Vol. 238, p. 358, 2001

Wuyts, S., Labbé, I., Franx, M. et al. 2007 ApJ 655 51

Chapter 5

Velocity fields of infrared selected disk galaxies at $z \sim 2$

Context The Tully-Fisher relation (TFR) at high redshift can best be studied using massive galaxies and using galaxies that resemble local disk galaxies. The rest frame K band TFR is locally tighter and less sensitive to extinction than the rest frame B band TFR, and rest frame K band magnitudes can now be obtained at high redshift using IRAC. The stellar mass TFR is a measure of the build-up of the stellar population within halo's.

Aims We target a sample of massive and a sample of morphologically and photometrically large disk galaxies at $z \sim 2$, most of which are selected at MIPS $24\mu m$. As we showed in a separate paper, one of these large disks galaxies is very similar to local disk galaxies.

Methods We used VLT-SINFONI to observe the Hα velocity fields and hence rotation curves of eight $z \sim 2$ galaxies. IRAC and MIPS $24\mu m$ photometry are available for all targets.

Results We derive velocity fields for four galaxies. The S/N of a fifth galaxy is too low to measure the VF. All are consistent with a rotating disk interpretation, although irregularities are observed in two cases and the extent of the Hα distribution limits the interpretation of two velocity fields. All galaxies are massive, with flat or maximum rotation curve velocities of $200 - 400$ km s^{-1}. Within the observed radii, there is no evidence for dark matter. The morphological and photometrically large disk selected galaxies have similar angular momentum and spin parameter as local spiral galaxies. The zero points of the rest frame B and K band TFR at $z \sim 2$ are (after correction for extinction) ~ 2.4 and ~ 1.4 mag brighter than in the local universe. All galaxies appear to be consistent with the local baryonic mass TFR. However, the interpretation of the TFR results is strongly limited by the small sample of galaxies which all have peculiarities.

L. van Starkenburg, P. P. van der Werf, S. Wuyts, M. Franx, M. Kriek, I. Labbé &
G. Rudnick
to be submitted to *Astronomy & Astrophysics*

5.1 Introduction

In the local universe, the best tracer of the velocity fields (VFs) of disk galaxies is H I. The H I disk extends to a few times larger radius than the stellar and molecular gas disk. However, H I can only be observed for nearby galaxies. The VFs of galaxies at cosmologically significant redshifts can only be observed using other tracers.

Alternative tracers for VFs are rest frame optical emission lines, such as Hα, [O III] $\lambda 5007/4959$ and [O II]$\lambda 3727$. Their extent is limited to the star forming disk. Also, these lines shift out of the range of optical spectrographs at $z \sim 0.3, 0.7$ and 1.3 respectively.

Until recently, the rotation curves (RCs) of galaxies at larger redshifts could only be observed using long slit near infrared spectrographs. Integral field spectra have significant advantages over long slit spectra with respect to identifying kinematic disturbances. Near-infrared integral field spectrographs, like VLT-SINFONI, are able to observe the VF of galaxies at $z \gtrsim 2$ provided the rest-frame optical emission lines are sufficiently bright.

A number of Hα and [O III]$\lambda 5007$ velocity fields (VFs) of redshift $z \sim 1 - 3$ galaxies have now been observed (Förster-Schreiber et al. 2006, Genzel et al. 2006, Bouché et al. 2007, Law et al. 2007, van Starkenburg et al. 2008a (hereafter PaperI), Wright et al. 2007, Nesvadba et al. 2006, 2008, Bournaud et al. 2008). Most galaxies observed were UV or optically selected. Some VFs are consistent with rotating disks, others appear to be mergers (see also Shapiro et al. 2008). Many show dynamical disturbances. A convincing case for a ordered rotating disk at $z \sim 2$ was presented in PaperI. Interestingly, this galaxy is one of the morphologically selected large disk galaxies of Labbé et al. (2003b).

The Tully-Fisher relation (TFR) is a tight correlation between luminosity and rotation velocity. Its scatter decreases from optical to near-infrared wavelengths (e.g. Verheijen 2001). If luminosity is replaced by stellar mass, determined from SED modeling, the tight correlation remains. Finally, the baryonic mass TFR relates the total baryonic (stellar and gas mass) to the rotation velocity.

Predictions for evolution in the slope, zero-point and scatter of the TFR and stellar mass TFR have been made (e.g. Steinmetz & Navarro 1999, Buchalter, Jimenez & Kamionkowski 2001, Portinari & Sommer-Larsen 2007). However, theoretical models fail to simultaneously reproduce the zero-point, scatter and slope of the TFR in all photometric bands and the shape and zero-point of the luminosity function (e.g. Courteau et al. 2007).

We attempted to select galaxies suited for a TFR analysis. We therefore selected galaxies with photometry over a large wavelength range, so that we have rest-frame K band luminosities (so that our results are not sensitive to uncertain extinction corrections) and can derive reliable stellar masses. We selected our galaxies from the two FIRES fields, HDF-S and MS1054 (Labbé et al. 2003, Förster-Schreiber et al. 2006). The FIRES data cover optical and near infrared bands and are publicly available[1]. For these fields, we also obtained IRAC imaging and MIPS 24 μm imaging (Labbé et al. 2005, Labbé private communication, Egami et al. 2006, Gordon et al. 2005).

Although some star formation (i.e. Hα, [O II] or [O III] emission line) is needed to

---

[1]see http://www.strw.leidenuniv.nl/~fires

measure the VFs, samples strongly biased towards extreme star formation rates are not suited for TFR studies because measured 'offsets' from the TFR can be due to recent star formation only (e.g. van Starkenburg et al. 2006). Also, massive galaxies are prefered because their $\log(L)$ are less affected by star formation than the $\log(L)$ of less massive galaxies (van Starkenburg et al. 2006). Magnitude limits and resolution effects also drive one to massive galaxies and local reference samples agree best on the high mass end of the TFR (van Starkenburg et al. 2006). Franceschini et al. (2003) studied a sample of ISO $15\mu m$ selected galaxies at $z \sim 0.2$ to 1.5 in the HDF-S and found that these are among the most massive galaxies in the field. We have obtained VFs of a subsample of these and will present the results in a forthcoming paper (van Starkenburg et al. 2008b). Here, we apply the same selection at a higher redshift and focus on MIPS $24\mu m$ selected targets at $z \sim 2$. This strategy allows the selection of massive galaxies and simultaneously allows a comparison between similarly selected galaxies in two different redshift ranges.

We also attempted to select suitable galaxies by selecting galaxies that morphologically resemble large disk galaxies (Labbé et al. 2003). These galaxies are characterized by an exponentially declining light profile extending over $2 - 3$ effective radii. Their sizes are comparable to those of local L_* galaxies. Their appearance in the rest frame optical is remarkably smooth and becomes irregular and more extended at shorter wavelengths (larger effective radii, r_e). Their SEDs show large rest frame optical breaks in their centers and bluer colors in the outer parts. This is reminiscent of local spiral galaxies with red bulges and blue disks. These large disks galaxies are bright in Ks band and are massive with stellar masses $> 10^{11} M_\odot$. These galaxies, if true disks, are ideal targets for high redshift TFR studies. We have confirmed the disk nature of one of these candidate disks and have shown that it has an ordered VF similar to well-developed disk galaxies in the local universe (PaperI).

The morphology of the large disk galaxies of Labbé et al. (2003b) shows some similarity with the double clump and clump-cluster galaxies of Elmegreen et al. (2005b). Both classes of galaxies show clumps at rest frame UV wavelengths. The large disk galaxies were selected by their exponentially declining light profiles and large scale lengths. Also, the clumps are symmetrically distributed around their K band centers. This is not generally the case of double clump and clump cluster galaxies (Elmegreen et al. 2005a, 2005b). These galaxies do appear to be spiral galaxy progenitors (Bournaud et al. 2007 and references therein) and recent SINFONI observations of one of these clump cluster galaxies at $z = 1.6$ revealed indeed a VF consistent with a rotating disk (Bournaud et al. 2008), albeit with significant kinematic disturbances related to the clumps.

In this paper, we present our sample of infrared and/or morphologically selected galaxies at $z \sim 2$[2]. Sample selection is further discussed in Sect. 5.2 followed by a short overview of the observations and data reduction in Sect. 5.3 and 5.4. We discuss the properties of the 1D spectra in Sect. 5.5. The VFs and RCs are presented in Sect. 5.6. We then discuss the masses in Sect. 5.7 and angular momenta in Sect. 5.8. Finally, we present the rest frame B and K band TFR and the stellar and baryonic mass TFR in Sect.

Table 5.1 — Sample selection criteria, redshifts and Ks magnitudes. The IDs of the MS1054 and HDF-S targets are the IDs from the FIRES catalog . The selection criteria are labeled as SCUBA ($850\mu m$ detection), MIPS ($24\mu m$ detection) and LD (morphologically large disk galaxy). The $24\mu m$ fluxes have units μJy and upper limits are three σ. For galaxies without a spectroscopic redshift, we used the photometric redshifts of Rudnick et al. (2001, 2003). The spectroscopic redshifts marked with a * were obtained from this work and had previously only a photometric redshift.

FIELD	ID	selection	F($24\mu m$)	z	Ks mag
MS1054	1383	SCUBA MIPS LD	202 ± 15	$z_{spec} = 2.43$	19.55
HDF-S	302	LD	< 12	$z_{spec} = 1.44$	19.70
MS1054	383	MIPS LD	54 ± 12	$z_{spec} = 2.12$	19.42
MS1054	1459	MIPS	107 ± 19	$z_{spec} = 2.08$	19.46
MS1054	1714	LD MIPS	64 ± 13	$z_{spec}^* = 1.46$	19.61
MS1054	1719	MIPS	289 ± 14	$z_{spec}^* = 1.72$	18.93
HDF-S	257	LD	< 15	$z_{spec} = 2.03$	20.25
HDF-S	267	LD MIPS	18 ± 3	$z_{phot} = 1.82$	19.98

5.9 followed by our conclusions in Sect. 5.10.

Throughout this paper, we use $H_0 = 70$ km s^{-1}Mpc^{-1}, $\Omega_M = 0.3$, $\Omega_\Lambda = 0.7$ and Vega magnitudes.

5.2   Sample selection

We selected both $24\mu m$ detected and morphologically large disk galaxies. We selected morphologically large disks galaxies in the MS1054 field using the same selection criteria as Labbé et al. (2003b) for the HDF-S field.

A special case is MS1054 1383 (Förster Schreiber et al. 2006). This galaxy is also detected with SCUBA at $850\mu m$ (Knudsen et al. 2005) and satisfies the Distant Red Galaxy criterion (Franx et al. 2003).

Choosing targets from each sample, we preferred targets bright in Ks band and with known spectroscopic redshift. Hα should be observable with SINFONI (we choose Hα for consistency with other data sets and to get a reliable estimate of the SFR). Also, it had to be possible to keep the target inside SINFONI's field of view (FOV) during the observations, so some targets in very crowded regions were excluded. In one case, it was possible to observe two targets (MS1054 1714 and 1719) at the same time. This increased their priority, especially of the fainter large disk galaxy. Selection criteria, $24\mu m$ flux, redshifts and K magnitudes are summarized in Table 5.1. There is significant overlap between the two samples.

5.3   Observations

We observed our targets with SINFONI (Eisenhauer et al. 2003, Bonnet et al. 2004), the near infrared integral field spectrograph of the VLT. We used the 8$''$ x 8$''$ FOV and the H, K or H+K grating depending on (photometric) redshift. The spectral resolution in these modes is respectively $R \sim 2900$, $R \sim 4500$ and $R \sim 1600$.

Our targets were observed during 3observing runs in 2005 and 2006. We used an

Table 5.2 — Observations. See Table 5.1 for an explanation of the IDs. The seeing is the seeing in y direction of SINFONI's FOV (see PaperI for a definition of x and y direction). The image quality is worse in the x direction, especially for targets observed with the single PSF star strategy.

FIELD	ID	run	t_{int}	grating	PSF strategy	emission lines	seeing
MS1054	1383	April 2005	7h	K	single	Hα, [N II]	0.″4
HDF-S	302	April 2006	2h20m	H	multiple	Hα, [N II][a]	—
MS1054	383	April 2006	2h40m	H+K	multiple	Hα, [S II][b]	0.″50
MS1054	1459	April 2006	3h	H+K	multiple	Hα, [N II]	—
MS1054	1714	April 2006	2h	H+K	multiple	Hα	—
			2h	H	multiple	Hα, [N II]	0.″55
MS1054	1719	April 2006	2h	H+K	multiple	Hα, [N II]	0.″54
			2h	H	multiple	Hα, [N II]	0.″53
HDF-S	257	August 2006	6h	K	multiple	Hα, [N II]	0.″55
HDF-S	267	August 2006	2h	H	multiple	—	—

  [a] lines fall on OH lines.
  [b] OH lines at [N II] wavelength.

ABA'B observing strategy, keeping the target in the FOV at all times for optimal efficiency. Offset positions and rotation angle were chosen so that nearby galaxies did not interfere with the observations of the target galaxy. As all our targets are too faint to acquire directly, we blind offset from a nearby bright star. Individual exposures were 600 or 900 s. Total integration times varied between 1 and 7 hours. For galaxies with photometric redshifts, we switched to the next target if we did not detect an emission line after integrating for 1-2 hours. The seeing (measured on the PSF star images) varied between 0.″4 and 0.″55.

For all but one,the galaxies in this paper were observed using the multiple PSF star strategy described in PaperI. Briefly, this means that a star is observed at every position in the FOV where we observe the target, as closely in time as possible. The positions and FWHMs of these PSF stars are then used to combine the data. The details of SINFONI's FOV reconstruction require a star for every position, as explained in PaperI. For the galaxy from the 2005 run,we used the 'single PSF star strategy' which means only one PSF star per OB was observed and the data is combined using the telescope offsets (see also van Starkenburg et al. 2008b).

We also observed one or more telluric standard stars for flux calibration for each target. We refer to PaperI for a detailed description of our observing strategy. Table 5.2 summarizes our observations.

5.4   Data reduction

When possible, we follow the data reduction scheme described in PaperI. Briefly, this includes removal of bad pixels and cosmic rays, removal of the odd-even effect, distortion correction, flat fielding, wavelength calibration and cube reconstruction. After first subtraction, an illumination correction is applied using a recipe from Juha Reunanen. The frames are combined using the positions of the so called "PSF stars" observed at

the same positions in the FOV as the target while weighting with the FWHM of the PSF stars squared (in y direction and measured at the wavelength of Hα, see PaperI). We used a second weighting parameter to correct for the different airmass of each frame, using the correlation between PSF star flux and airmass.

Compared to the reduction scheme described in PaperI, the following changes were made for (some of the) targets presented here.

For MS1054 1383, we observed only one PSF star in the center of the FOV per OB of four exposures. We combined the exposures according to this single PSF star and the telescope offsets, but note that the increased position uncertainty of the target in the x direction of SINFONI's FOV and hence worse image quality (see also PaperI).

We determine the position and FWHM of the PSF stars at the wavelength of Hα (see for an explanation PaperI). In the case of MS1054 383, the PSF stars were too faint to reliably measure the FWHM. Therefore, we combined the cubes using the position measured at the relevant wavelength while weighting with the FWHM as measured on the median collapsed cube. In the final combined PSF cube, it is possible to measure the FWHM at the relevant wavelength, and this is the FWHM we use for seeing.

For HDF-S 257, we did a relative flux calibration using the correlation between PSF star flux and air mass. For the other targets, we did not apply this correction because either the number of PSF stars was too small, the conditions were not good enough (no or weak correlation between PSF star flux and airmass) or we did not detect any emission lines.

The SINFONI pipeline uses arc frames for wavelength calibration. However, the positions of the slitlets on the raw science frames is not entirely stable. Small shifts in the wavelength direction lead to strong OH line residuals in the final reconstructed cubes. For the J and H band data, the SINFONI pipeline can be easily modified to do the wavelength calibration on the OH sky lines, which enables us to measure the wavelength calibration for individual science frames and correct for small shifts accordingly.

In J and H band, a star like persistence effect with constant slope spectrum is sometimes observed at the beginning of an OB. We give a full description of this effect and how to remove it in van Starkenburg et al. (2008b). For the galaxies presented in this paper, we only removed this faint persistence effect for HDF-S 302.

During the two observing nights in April 2006, telluric standards without directly measured H and K magnitudes were used for some targets (MS1054 1459 first and second night, MS1054 1714 and 1719 second night, MS1054 383 second night). In these cases, we used the correlation between H or K and I magnitudes from all stars of the same spectral type from the same catalog (Hipparcos) to estimate the H or K magnitude. These correlations have ∼ 0.1 mag spread with outliers up to 0.5 mag. The uncertainty in the final flux calibration according to ESO documentation is 5-20%.

5.5　Results

We detect Hα and at least one more emission line in 7 out of 8galaxies. We can derive VFs for four galaxies, three are presented in this paper. Our best case, HDF-S 257, was presented in PaperI. The fifth galaxy does not show rotation and a sixth galaxy shows a

Table 5.3 — Hα flux (units 10^{-16}erg s^{-1} cm^{-2}), SFR derived from Hα flux ($M_\odot$yr^{-1}), SFR corrected for extinction using the best fit A_V from Wuyts et al. (2007), (rest frame) EW(Å), [N II]/Hα ratio and FWHM (km s^{-1}). The line ratio of MS1054 383 refers to a [S II]/Hα ratio (marked with a '*').

FIELD	ID	F(Hα)	SFR$_{H\alpha}$	SFR$_{H\alpha,A_V}$	EW(Hα)	[N II]/Hα	FWHM
MS1054	1383	3	380	1700	211	0.7	422
MS1054	1714	1	26	90	95	0.2	357
MS1054	1719	1	43	170	39	> 0.3	444
MS1054	383	0.8	66	110	54	0.16*	372
MS1054	1459	0.56	44	100	34	0.48	574
HDF-S	257	1.6	116	260	159	0.22	244

velocity gradient in a synthetic long slit spectrum but the S/N is insufficient to derive a VF. The last galaxy for which we detect emission lines has insufficient S/N because of strong OH line residuals.

We calculated the SFR for each galaxy with a reliable Hα detection using the Kennicutt (1998) relation for a Salpeter IMF assuming all Hα flux is due to star formation (see Table 5.3). All targets are forming stars at large rates. Two are in the ULIRG regime. We also list the A_V corrected star formation rates in Table 5.3), using the best fit A_V from SED fitting. We note that these are A_V's derived from the continuum, and the true A_V's for the line fluxes might be different. Unfortunately, we do not have Hβ measurements for any of our targets.

The rest frame EWs were calculated using the interpolated broad band fluxes for continuum. We find that EW correlates with SFR and specific SFR (SFR/M_*). The FWHMs of Hα integrated over the target are also listed in Table 5.3. All but one are < 500 km s^{-1}.

We calculated the [N II]/Hα or [S II]/Hα ratios for all galaxies for which we detect emission lines. In three cases (MS1054 1383, 1459 and 1719), the [N II]/Hα ratio suggests the presence of a type II AGN or shocks (see also Table 5.3). In one case, MS1054 1459, the Hα line is also broad: FWHM $= 570 \pm 150$ km s^{-1}.

Using the method described by Wuyts et al. (2007), we fitted the SEDs to obtain the best fit stellar masses, ages, extinction A_V and SFRs. This method assumes a Salpeter IMF with stellar masses in the range $0.1 - 100$ M$_\odot$ and solar metallicity. The results are presented in Table 5.4. The SFRs determined from SED fitting and from Hα (uncorrected for extinction) are remarkably consistent, except for MS1054 1719 where the SFR from SED fitting is 6 times larger than the SFR from Hα. This is surprising as one would expect that the extinction corrected SFR from Hα would agree better with the SFRs from SED fitting (which are corrected for extinction). The overprediction of the SFR by the SED fitting method for MS1054 1719 could be explained by the presence of an AGN. In that case, the SED fit also overestimates the extinction and underestimates the age (Wuyts et al. 2008). The best fit A_V of MS1054 1719 is indeed quite large (2.0) but the best fit age is the oldest in our sample (1.4 Gyr).

We will now discuss the properties of individual galaxies. First, we discuss the galaxies for which we can derive a VF (except HDF-S 257, for which we refer to PaperI). More information about the other 5 galaxies can be found in Sect. 5.5.2.

Table 5.4 — Results from SED fitting. The stellar masses are in units of $10^{10} M_\odot$, the ages in Myr and the SFRs in $M_\odot$ yr^{-1}. The SFR from Hα is listed in the final column for comparison. The stellar mass of HDF-S 267 was calculated with slightly different photometric redshift (1.78) than listed in Table 5.1 because we used improved photometric redshifts of Brammer et al. (2008) during analysis of the data. when preparing the observations.

FIELD	ID	M_*	age	A_V	SFR$_{SED}$	SFR$_{H\alpha}$
MS1054	1383	$37.7^{+6.0}_{-3.3}$	510	2.2	352	380
MS1054	1714	$9.0^{+1.1}_{-0.6}$	810	1.8	28	26
MS1054	1719	$33.9^{+2.5}_{-0.8}$	1400	2.0	259	43
MS1054	383	$9.6^{+0.1}_{-2.4}$	510	0.8	89	66
HDF-S	302	$3.4^{+0.1}_{-0.4}$	450	1.0	40	—
MS1054	1459	$29.5^{+2.1}_{-0.6}$	1300	1.2	19	44
HDF-S	257	$3.0^{+0.3}_{-0.1}$	180	1.2	143	116
HDF-S	267	$4.9^{+0.5}_{-0.9}$	360	1.4	87	—

5.5.1 Notes on individual targets with VF

MS1054 1383   We selected MS1054 1383 for observations because it is detected at $850\mu m$ (5.1 ± 1.5 mJy) with SCUBA (Knudsen et al. 2005, van Dokkum et al. 2004) and Hα was detected before (van Dokkum et al. 2004). It is also bright at $24\mu m$ and is a large disk galaxy with inclination $i \sim 54°$. It also fulfills the DRG criterium (Franx et al. 2003).

The Js and Ks images (from FIRES data) are shown in Fig. 5.1 (we show the Js image instead of the F814W that we show for the other galaxies because MS1054 1383 is not detected in the F814W image). The Ks band profile is smooth, in Js band a small extension is visible on the eastern side of the galaxy. Van Dokkum et al. (2004) mention the possibility that this extension is not an extension but a background galaxy at $z = 3.52$. There is also an extension on the north-west side of the galaxy in Js band. In the NIC-MOS H band image (Toft et al. 2007), this appears to be a tidal tail. Toft et al. (2007) also show a stacked $V_{F6060W} + i_{F775W} + z_{F850LP}$ image. This image shows a compact source located slightly offset from the K band center and a fainter source on the opposite side of the K band center and some very faint emission at larger distances. These compact sources near the K band center could correspond to star forming regions, or could indicate an ongoing merger.

We detect Hα and [N II] at $z = 2.43$. The derived SFR is $380 M_\odot$ yr^{-1} (uncorrected for extinction), consistent with the values found from the $850\mu m$ flux ($\sim 500 M_\odot$ yr^{-1}, van Dokkum et al. 2004) and from SED fitting ($\sim 350 M_\odot$ yr^{-1}).

The emission lines are tilted and we discuss the VF and RC in Sect. 5.6.

MS1054 383   MS1054 383 was selected as MIPS $24\mu m$ source and as large disk galaxy. The redshift was previously obtained after integrating 24 hours in January and March 2005 with WHT/LIRIS in multi-object mode (H+K grating) by Kriek. This galaxy has a small companion (see Fig. 5.2) as will be discussed further in Sect. 5.6.2. The K band (rest frame optical) profile is a smooth disk with inclination $i \sim 59°$, the F814W (rest frame UV 2600Å) image shows an irregular distribution with two prominent clumps.

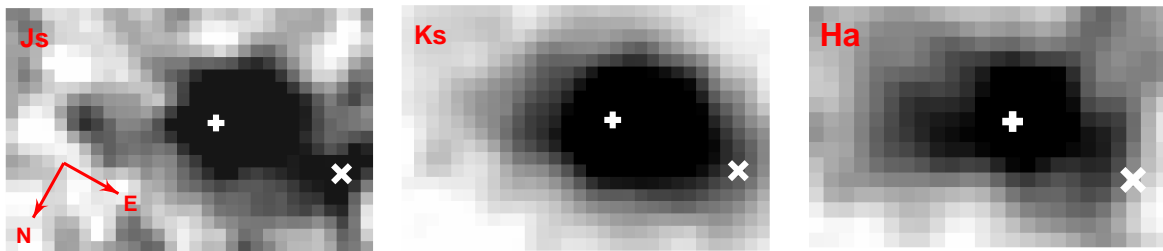**Figure 5.1 —** Js (FIRES) image, Ks (FIRES) image and Hα linemap of MS1054 1383 (MS1054 1383 is not detected in F814W, therefore we show the ISAAC Js image). Image sizes are 3″x 2″. The Hα linemap has been smoothed by a 3 pixel width gaussian to increase S/N. The + point marks the Ks position from Labbé et al. (2003a), the X point marks the brightest pixel of the Js extension. The contrast was increased in all figures to show the extent of the emission.
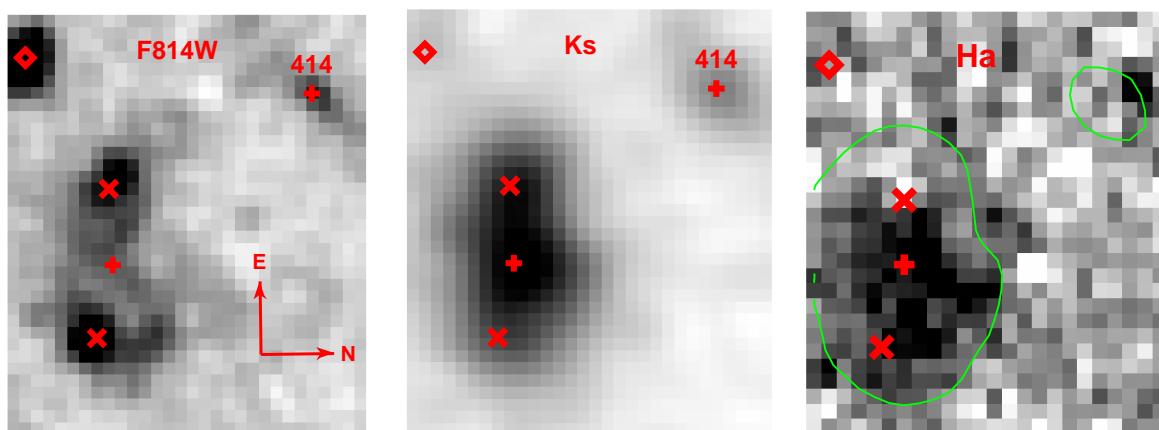

Figure 5.2 — F814W (rebinned to FIRES) image, Ks (FIRES) image and Hα linemap of MS1054 383. Image sizes are 3″x 3″.5. The + point marks the Ks position from Labbé et al. (2003a), the X points mark the centers of the F814 clumps and the diamond marks the location of the satellite. A Ks band contour is shown in the Hα linemap. Note that Hα only covers the western clump and the central part of the Ks band image. Also visible in the F814W and Ks images is a second, unrelated, galaxy, id 414 in the FIRES catalog.

The satellite is also bright in the F814W image.

After integrating 2hrs40mins, we detect Hα and faint [S II]λ6717/6731. The [S II]/Hα ratio is consistent with values found for star forming galaxies (Veilleux & Osterbrock 1987). The expected positions of the [N II]λ6583/6548 lines coincide with two bright OH lines. The distribution of the Hα emission is different from both the K and F814W images: it is concentrated around the western clump and the K band centre, but the eastern clump is not detected in Hα, see Fig. 5.2c. The satellite has a very faint Hα line, while it is bright in F814W.

We can derive a VF and discuss it in Sect. 5.6.

MS1054 414 was also in the FOV, see Fig. 5.2. We detect [O III]λ5007/4959, [O II]λ3727 and [Ne III]λ3869 at $z = 3.229$, consistent with the photometric redshift.
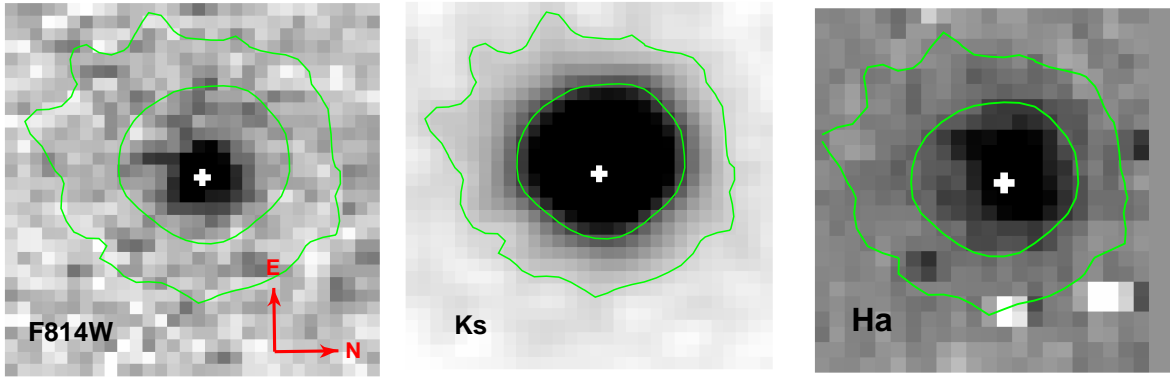
Figure 5.3 — F814W (rebinned to FIRES) image, Ks (FIRES) image and Hα linemap of MS1054 1719. Image sizes are $3''x\,3''$. The right-most two columns in the Hα image are missing. The + point marks the Ks position from Labbé et al. (2003a). Two Ks band contours are shown. The bright contour corresponds approximately to the Hα distribution, while the fainter contour shows the total extent of the Ks band image. The F814W flux is even more concentrated than the Hα flux.

MS1054 1719   We selected MS1054 1719 for observations because it has a MIPS $24\mu m$ detection and it is bright in K. Its half light radius is $0\!''\!.40$ and its Sersic index is 2.10 (measured in Js band) (Trujillo et al. 2006). The seeing corrected inclination is $41°$ (Trujillo et al. 2006). The Ks band emission is much more extended than the F814W emission, see Fig. 5.3, in contrast to the large disk galaxies.

We detect Hα and [N II]$\lambda6583/6548$ at $z = 1.716$. The extent of the Hα emission is in between the Ks and F814W, see Fig. 5.3. The [N II]$\lambda6583$ line is on top of an OH line which makes it difficult to put constraints on the [N II]$\lambda6583/$Hα ratio. We estimate it is underestimated by a factor two from the [N II]$\lambda6548$ line flux. [S II]$\lambda6717/6731$ is in a region with many OH lines and not detected.

The Hα line (and the [N II] lines) are tilted. We discuss the VF and RC in Sect. 5.6.

5.5.2   Notes on individual targets without VF

For 5 galaxies, we could not derive a VF. In one case, the S/N is good but there is no velocity gradient. In another case, we detect a velocity gradient, but the S/N is too low to extract a RC. In a third case, Hα is on a bright OH line and cannot be used for a velocity analysis. In two cases, we do not detect any emission lines. We discuss possible reasons for each galaxy below.

HDF-S 302   We detect Hα at the expected redshift, but the line is faint and on top of a bright OH line, as is [N II]$\lambda6583$. Even a synthetic long slit analysis failed.

MS1054 1459   This galaxy was selected because it is bright in K and had a previously obtained spectroscopic redshift ($z = 2.08$) from ISAAC MR spectroscopy in April 2004 by Kriek and van der Werf. We detect Hα and [N II]$\lambda6548/6583$. We do not detect [S II]$\lambda6716/6731$, [O III]$\lambda4959/5007$ and Hβ ([O III] and Hβ are in a region where to OH lines are blended at the resolution of the H+K grating).
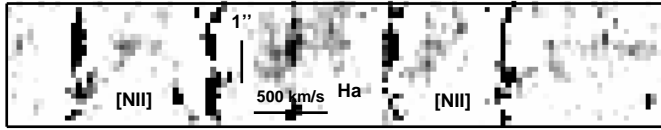
Figure 5.4 — Synthetic long slit spectrum along the K band major axis (position angle 87° counterclockwise from the north, slit width 1."25) of MS1054 1714. The horizontal axis is wavelength (or velocity), the vertical axis is position. The contrast and scales were chosen so that the lines are visible in print. Hα and [N II]λ6583/6548 are visible as tilted emission lines. Also visible as dark vertical stripes are OH line residuals.

We find no hints for rotation in the cube or synthetic long slit spectra. One explanation could be that the galaxy is viewed almost face-on. A second explanation is that the emission line flux is dominated by emission from an AGN: the FWHM of Hα is $\sim 570 \,\mathrm{km\,s^{-1}}$ and [N II]/H$\alpha = 0.48 \pm 0.10$.

MS1054 1714 We observed MS1054 1714, a large disk galaxy, as a bonus galaxy in the same FOV as (the MIPS 24μm selected galaxy) MS1054 1719. The Ks band profile is a very smooth edge-on disk ($i \sim 70°$), but at shorter wavelengths, a small clump at the west side of the disk is visible.

The photometric redshifts of MS1054 1714 and 1719 placed their Hα lines between H and K band and indicated they were possibly at the same redshift. To maximize the chance of detecting an emission line, we started our observations using the H+K grating. After we detected Hα in H band for MS1054 1719, we switched to H band for better spectral resolution. In the H grating data, we were able to identify Hα and possibly [N II] at a different redshift, $z = 1.46$, for MS1054 1714. Although close together on the sky, MS1054 1714 and 1719 are not a pair. We do not detect [S II]λ6717/6731.

The S/N is too poor to measure a VF. In a synthetic long slit spectrum, the Hα line is clearly tilted and extends over $\sim 500 \,\mathrm{km\,s^{-1}}$ in $\sim 1.5''$ but we were not able to measure a RC, as the line lies on top of an OH line and the S/N remains poor. The synthetic long slit spectrum is shown in Fig. 5.4.

HDF-S 267 As third HDF-S large disk target, we choose HDF-S 267 because it was the brightest of the remaining targets (after HDF-S 302 and HDF-S 257) and had a (photometric) redshift that would put Hα at an observable wavelength with SINFONI. We detect no emission lines after 2 hrs integrating in H band ($z_{phot} = 1.82$). There are several possible reasons for this non detection. HDF-S 267 has a photometric redshift which puts Hα between H and K band. We choose the H grating and not the H+K grating because the spectral resolution of the H+K grating is often not sufficient to resolve emission lines between the many OH lines in H band. But it is possible that Hα falls outside H band and other lines are too faint to detect.

5.6   Velocity fields and rotation curves of individual targets

We followed the method described in PaperI to measure and model the VF and RC. Here, we summarize our methods and refer to PaperI for a more detailed description.

Because the S/N of individual spectra is low, automatic fitting routines confuse Hα with OH line residuals. We therefore manually fit gaussians to Hα using IRAF's 'splot'. We sum over 4 or 9 pixels to increase S/N if necessary.

For HDF-S 257, we also measured the velocity dispersion field (see PaperI). For the galaxies presented in this paper, we were not able to measure a dispersion field. The spectral resolution was insufficient (H+K grating) and/or the S/N of the individual spectra was too small.

The VFs reveal generally monotonic velocity gradients. In order to test whether these represent order rotation, we fit tilted ring models using GIPSY (van der Hulst 1992, Vogelaar & Terlouw 2001) to model our VFs. We start with fixed values for all parameters except the rotation velocity (i.e. position angle of the major axis, inclination and center fixed to the Ks band values, systemic velocity fixed to the velocity measured in the center, and expansion velocity fixed to zero). We then redo the fit with a second free parameter. If we get consistent results for the second parameter between the rings, we replace the original value of the second parameter by the average of the free fit values for each ring. We continue with the next parameter until our best fit values do not change anymore. We found that the S/N of the VF is insufficient to constrain most parameters from the VF alone. For these parameters, we keep the default values mentioned above. We make a model VF from our best fit model and compare this to the observations. In particular, we look for systematic differences between the observations and models.

We compare the RC of our best fit VF to the RCs of fits with slightly different parameters to quantify the uncertainties of the best fit velocities, and in particular those of V_{max} or V_{flat}.

For HDF-S 257, we also modeled the effect of the PSF and the Hα surface brightness distribution on the best fit RC (see PaperI). Here, we did not attempt to model these effects on the best fit RCs for reasons specified below for each target. We emphasize that the RCs presented here are therefore observed rotation curves and that the intrinisic RCs may be different due to the effects of seeing and the Hα distribution.

5.6.1   MS1054 1383

Although MS1054 1383 has the longest integration time of our sample, 7 hours, the S/N of individual spectra is poor. Therefore, we summed each pixel with its 8 neighbours to measure the VF. The resulting VF therefore shows strong pixel-to-pixel correlations, see Fig. 5.5a on page 112. Looking at the VF, one notices immediately that its shows strong non-regularities: the major and minor axis (defined as the line connecting the most extreme velocities and the contour at the systemic velocity) are not orthogonal but make an angle of $\sim 105°$. Also, the position angles of the major and minor axis of the VF are different from the position angles of the major and minor axis of the Hα linemap and the Ks band continuum (which is often observed in local ULIRGS, see Colina et al. 2005). There are also several regions with velocities offset from the general trend, for example at the receding end of the major axis. However, there is no obvious relation between the J band extension and the tidal tail and the distortions in the VF. We investigate below the possible relation between the ACS sources and the observed VF.

Figure 5.6 — Integrated spectrum of MS1054 1383 over the area where the emission lines are double peaked. The lower panel shows the logarithm of the sky spectrum.
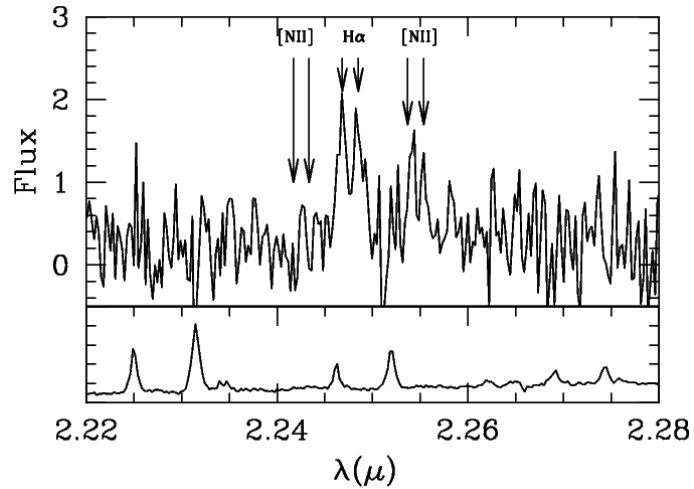
Another interesting feature of the data is that over a small region (~ 1 seeing element) just off the (photometric) center Hα and [N II]λ6583 are double peaked. The area is marked in Fig. 5.5 on page 112 and the integrated spectrum over the whole region is shown in Fig. 5.6. The velocity shown in the VF in Fig. 5.5 on page 112 is the velocity measured after smoothing the spectra so that a single gaussian can be fit to both peaks. We discuss the properties of this region and the possible interpretation below.

We fitted a tilted ring model to the VF following the method described above. The best fit position angle is 115° CCW from the north, where we expected $\sim 70°$ from the K band photometry. The major and minor axis as fit from the VF are shown in Fig. 5.5a on page 112 as the full axes. The minor axis follows the systemic velocity line. We were not able to reproduce other parameters from the VF. We also fitted the receding and approaching half of the VF separately because the RC appeared to be asymmetric, see Fig. 5.7a. This did not change the best fit PA. The VF, the best fit model (with new PA and both halves fitted separately) and its residuals are shown in Fig. 5.5a-c on page 112. Note that there are strong systematic residuals between the observed and modeled VF. There is no clear correlation between the J band extension and the irregularities in the VF.

The resulting RC is shown in Fig. 5.7a. The receding half is flat at ~ 85 km s^{-1}. The approaching half steeply rises to ~ 400 km s^{-1} and then the S/N is insufficient to decide between a shallower rise or a flatting.

The strong residuals from the fit led us to investigate the VF further. We noted that the photometric center is not the point with the largest velocity gradient as determined in a spider diagram. This point lies $0\rlap{.}''375$ (3 pixels) to the left in Fig. 5.5 on page 112 and we will refer to it as the 'spider center'. When we made a new tilted ring model taking this point as the center of rotation, we were able to reproduce the systemic velocity from the VF, the quality of the fit increases (see Fig. 5.5d-f on page 112, residuals from the fit are smaller and there are less systematic differences) and the RC becomes almost symmetric: the receding and approaching half flatten at ~ 240 km s^{-1} and ~ 190 km s^{-1}, see Fig. 5.7b. We use the average of these two velocities, 215 ± 40 km s^{-1} in the analysis below.
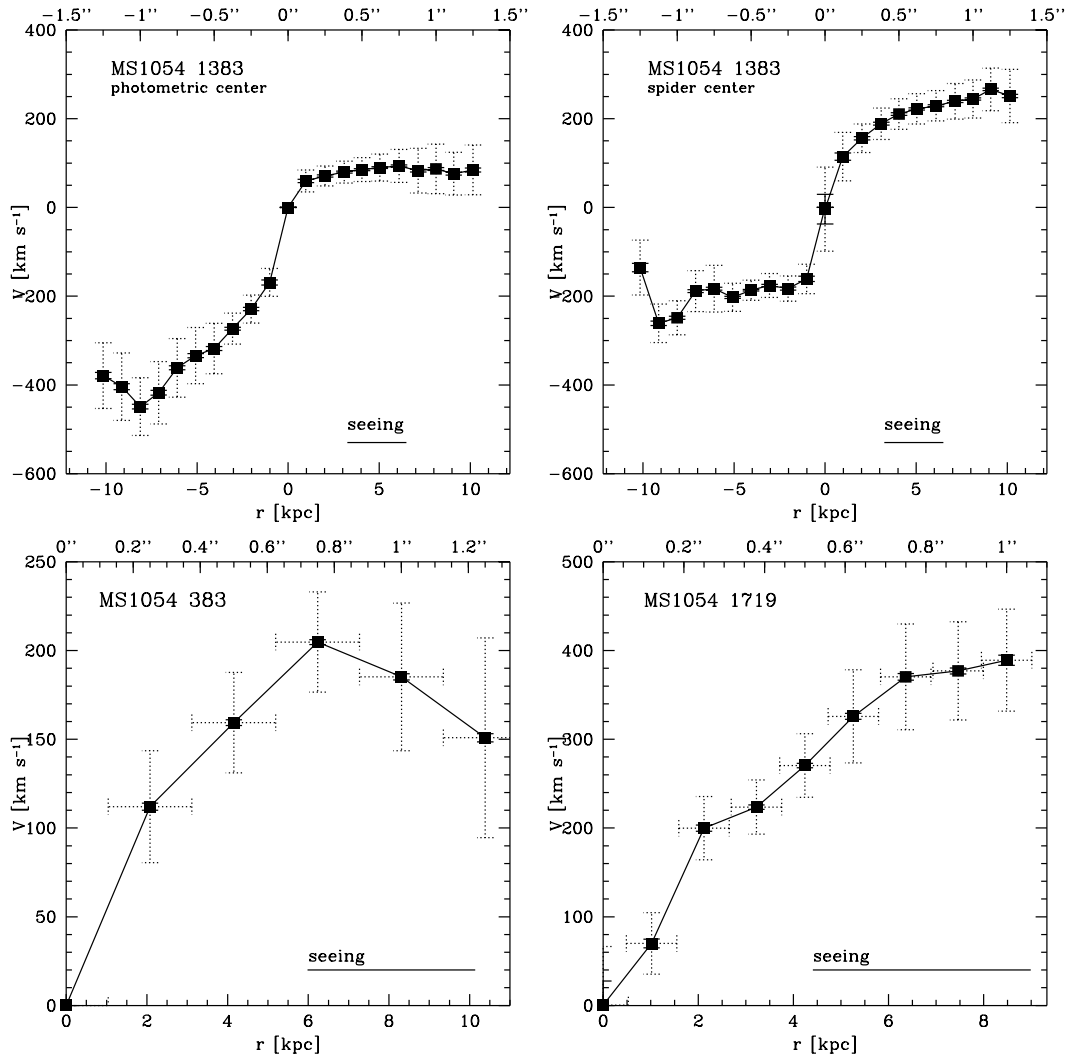
Figure 5.7 — RCs of MS1054 1383 (upper two panels, for two different choices of dynamic center, receding and approaching sides fitted separately), MS1045 383 (lower left panel) and MS1054 1719 (lower right panel). The full velocity errorbars give the formal fit errors from GIPSY. The dotted velocity errorbars give the scatter around the best fit value. The radius errorbars in the lower panels give the range in radius for which we fitted the velocity. We did not plot those errorbars in the upper two panels, as the points in those panels are also correlated by the binning to 9 pixels when we derived the VF.

The photometric center was determined in the K band image. At this redshift, observed K band corresponds to rest frame R band. In local ULIRGS, offsets between the optical nucleus (or nuclei) and the near-IR center are not uncommon due to heavy extinction. Also, the resolution of the K band image (0.″46 which corresponds to 3.7 kpc at this redshift) does not rule out the possibility of double nuclei. A ongoing merger would be consistent with the tidal feature seen in the NICMOS image (Toft et al. 2007). The ACS image from Toft et al. (2007) shows indeed two components near the K band center. The distance between the components is consistent with the distance between the photometric and spider center. However, the orientation of the ACS clumps is $\sim 30°$ different from the orientation of the photometric and spider center. We conclude

that an ongoing merger could explain many observed phenomena, but there is no conclusive evidence.

We did not attempt to model the effect of the PSF on the RC observed. As MS1054 1383 is not detected in F814W, we do not have a high resolution model for the intrinsic Hα distribution.

The velocity gradient in the center is very steep. This implies a large concentration of mass in the centre. For $r < 0\,''.25$, the inferred mass is $1.4 \times 10^{10} M_\odot$ (smearing by the seeing was not taken into account) or $\Sigma_{dyn} = 1.1 \times 10^3 M_\odot \, \mathrm{Pt}^{-2}$.

We conclude that the VF of 1383 shows some irregularities from a simple rotating disk. There is some evidence for a different photometric and dynamical center or an ongoing merger. However, insufficient S/N prohibits definitive conclusions about the interpretation of the irregularities.

5.6.1.1 Double peaked emission line region

We will now investigate the nature of the double peaked emission line region.

We checked whether the two peaks are real by splitting the data set in half. The double peak is visible in both data sets. The velocity difference between the two peaks is similar for Hα and [N II] (~ 210 km s^{-1}) and there are no bright OH lines that could cause the observed splitting. We therefore conclude that the lines are truely double peaked.

The double peaked area is centered slightly eastward of the photometric center. It does not coincide with the spider center. The brightest ACS clump is located north of the double peaked area, the overlap is $\lesssim 40\%$.

The fluxes in the receding and approaching lines are approximately the same for Hα (2.9 and 2.8×10^{17}erg s cm^{-2}), see Fig. 5.6. The [N II]/Hα ratio is slightly different: 0.54 and 0.38 for approaching and receding sides respectively.

The area over which the lines are double peaked is comparable to the seeing disk. In principle, a point source could be responsible for the line splitting. On the other hand, the double peak region almost coincides with the peak in the Hα flux. It may be possible that the S/N is too poor over most of the galaxy to detect line splitting.

We searched for velocity structure (velocity or velocity difference gradients) but could not find it. The small area and low S/N may prohibit the detection of small gradients.

The measured VF in Fig. 5.5 on page 112 shows the velocity measured after smoothing the spectra until a single gaussian can be fit to both peaks together. We checked whether this velocity best matches with the overall VF by replacing the measured values with the velocities from either the approaching or receding line and refitting the VF. This has very little effect on the overall best fit VF. The single fit leaves indeed the smallest residuals.

There are several possible explanations for this double peaked line region. A good explanation should be consistent with the properties described above.

First, a very strong velocity gradient near the center smeared by seeing might result in observing both the receding and approaching half in the same pixel. This could result in a double peaked line if there is for example a bright ring around the center

which increases the fluxes of the velocities of the ring. The velocity gradient $\Delta V \sin(i)$ as observed in the RC (with photometric center) is ~ 200km s^{-1} over $0\overset{''}{.}4$ (the seeing disk). This value is very similar to the velocity difference found between the receding and approaching side of the double peaked emission line. This is suggestive, but without knowledge of the flux distribution at smaller scales, no evidence. The velocity gradient of the RC with the spider center is slightly larger over the same distance: ~ 240km s^{-1}, but we do not observe a line splitting in that area. This could be due to the lower line fluxes in that area. An argument against this ring hypothesis is that the location of the double peaked area does not coincide with the photometric (or spider) center.

A second explanation could be a small disk in the center with different inclination and position angle. However, the double-peak area is slightly off the photometric center, and certainly off from the dynamical centre.

A third explanation is inflowing and/or outflowing material. The receding component is most offset from the general VF, which would imply infalling material. The similar fluxes would be a coincidence in this case. The SFR per unit area of this galaxy is much larger than the threshold ($0.1 M_\odot$ yr^{-1} kpc^{-2}) for a superwind as given by Heckman (2003). The velocity offsets are consistent with the superwind interpretation (Rupke et al. 2005), but the approaching component being less offset from the overall VF than the receding component contradicts this interpretation. Evidence for a superwind has been found for a lensed submillimeter galaxy at $z = 2.6$ by Nesvadba et al. (2007). Their Hα and [N II]$\lambda 6583$ lines show a blue wing with a relative offset of ~ 340 km s^{-1}. Also, their [N II]/Hα ratio, 0.83, indicates the presence of shocks in the outflowing gas. We searched for wings in the line profiles of MS1054 1383 but found none, which is however consistent with the poorer S/N of our data.

Finally, another explanation is a merger or two nuclei that are not resolved in the K band image, because they are close and/or because one is more luminous (or much more extincted) than the other. The distance (less than one seeing element) between the photometric and spider center is consistent with this interpretation. The clumps seen in the ACS image support this interpretation, although their location does not precisely coincide with the photometric or spider center. Also, the rest frame wavelength of the ACS image corresponds to $\sim 2300 \AA$, so the fluxes are very sensitive to obscuration by dust. The double peaked lines coming from one of the two nuclei can then be explained by a strong velocity gradient in the center and/or a small rotating disk in around the center of that nucleus. A merger interpretation would also be consistent with the tidal tail seen in J and NICMOS H band.

We conclude that the last explanation has the least problems, but supporting evidence is unfortunately not available.

5.6.1.2   *Comparison to other submillimeter sources*

MS1054 1383 is the nineth SCUBA submillimeter (SMM) source for which Hα integral field spectroscopy has been obtained (Nesvadba et al. 2007, Swinbank et al. 2005, 2006). Of the other 8 SMM galaxies, five show two or more components separated by 1-2$''$or $8 - 16$ kpc. Two are compact sources, and the morphology or the remaining source is unknown due to a not fully understood foreground lens (Swinbank et al. 2006). The

average velocity offset observed between dynamical subcomponents is ~ 180 km s^{-1}. MS1054 1383 is morphologically and dynamically different from these other SMM galaxies. It has an extended morphology without these galactic scale clumps (although there is the J band extension/background galaxy and the tidal tail). Its VF is consistent with a single large disk, but shows kinematic distortions in the center that may be evidence for multiple components in the center. In some cases, (part of) the dynamical differences may be attributed to seeing differences during the observations.

Bouché et al. (2007) compared their UV and optical selected samples with SINFONI observations with 13 bright submillimeter galaxies ($F(850\mu m) > 5mJy$) at $z \sim 2.5$ observed with the IRAM Plateau de Bure Interferometer. All but one of the submillimeter galaxies are compact with $R_d < 3$ kpc and their maximum rotation velocities as calculated from their line profiles vary between 150 and 550 km s^{-1}. Based on millimeter interferometry, they find that submillimeter galaxies are more compact and more dense than rest frame UV and rest frame optical selected galaxies at similar redshift. In contrast, we find that our submillimeter detected galaxy, MS1054 1383, that was observed with SINFONI as were the UV and optical selected galaxies of Bouché et al., has a similar scale length and density as the UV and optical selected galaxies. It would be very interesting to have Hα integral field spectroscopy of the submillimeter galaxies observed with IRAM, to see whether MS1054 1383 is a rare case, or whether the Hα structure of the submillimeter sources is very different from the CO structure.

5.6.2   MS1054 383

The VF, shown in Fig. 5.8 on page 113, was measured after rebinning to $0\rlap{.}''25$ scale to increase S/N in individual spectra. Still, the S/N at the outer edges of the Hα distribution is poor and these points should be interpreted with caution. The companion is shown in this figure as a single pixel, but its velocity was measured integrated over the whole clump (approximated with a $r = 0\rlap{.}''375$ (3 pixels) radius circle centered on the K band center of the clump). Its velocity relative to the K band center is -281 km s^{-1}. One notices that the VF is not as regular as that of HDF-S 257 (see PaperI). Moreover, the position angle of the major axis seems to be different from the position angle of the K band major axis.

We fitted tilted ring models to the VF following the methods described above. The position angle of the major axis was found to be slightly different ($\sim 20°$) from the position angle of the major axis of the Ks image. We were unable to constrain other parameters from the VF. The fact that we detect only the receding part of the VF leaves in particular the center of the galaxy poorly constrained. The best fit VF and its residuals are shown in Fig. 5.8 on page 113. The systematic residuals illustrate the complex kinematics of this galaxy.

The RC of the best fit model is shown in Fig. 5.7c. We find $V_{flat} \sim 180 \pm 20 \pm 50$ km s^{-1}. where the first error bar reflects the scatter that occurs when different parameters are chosen for the tilted ring model and the second errorbar reflects the choice of slightly different centers from the RC gradient. The RC appears to flatten at $r > 6$ kpc, but this flattening is uncertain due to the poor S/N in the outer parts.

We did not attempt to model the effect of the PSF on the RC observed because the

expected effect on V_{flat} of the PSF is much smaller than the uncertainties due to the fact that the approaching side of the VF is hardly covered and the complex kinematics of this galaxy.

5.6.3   MS1054 1719

MS1054 1719 is the only target that was not selected as a large disk galaxy for which we can derive a VF. It is a smooth VF extending over nearly $2''$ along the major axis which is significantly smaller than the Ks image, see Fig. 5.9 on page 114.

We fit tilted ring models to the VF following the method described above. We were able to determine the position angle of the major axis and the dynamical center from the VF alone. The best fit position angle is $\sim 5 - 10°$ offset from the PA found on the K image, but within the errorbars. We were also able to reproduce the center from the VF alone. The center found is 1 pixel west of the expected center from H band, but as this new center is consistent with the center of the Hα linemap, we suspect that there is a slight offset between the H band and SINFONI data and that the photometric and dynamical center are the same. The best fit model and its residuals are also shown in Fig. 5.9 on page 114.

The RC of the best fit model is shown in Fig. 5.7d. There is a tentative flattening at the largest radii, but this flattening is sensitive to the parameters of the fit and not significant. The maximum velocity (corrected for inclination) is very large: $V_{max} = 389 \pm 45$ km s^{-1}, where the error bars were determined from tilted ring models with slightly different parameters and taking into account $5°$ uncertainty in the inclination. As the Ks image extends to larger radii, both the already very large maximum velocity and the derived dynamical mass should be interpreted as lower limits. Similar maximum velocities are rarely observed for local galaxies.

We did not attempt to model the effects of the PSF on the VF observed because the RC does not flatten and the total extent of the RC is relatively small.

5.6.4   Summary

We detect VFs in 4 out of 7 galaxies with emission lines. A fifth galaxy shows a velocity gradient in a synthetic long slit spectrum, but with insufficient S/N to measure a RC. In one case, we were unable to detect tilts because of poor S/N and OH line contamination. In only one case, there was no evidence for velocity gradients at all.

The extent of the Hα emission was a limiting factor in our analysis of two targets, MS1054 383 and 1719. In the first case, a longer integration time is likely to reveal Hα emission at the approaching side, as it is detected in F814W (=rest frame UV). For MS1054 1719, increasing the integration time might not result in detecting Hα over a larger area, as the F814W flux is concentrated in the center.

Unlike the very regular VF of HDF-S 257, two of the VFs presented here show kinematic distortions. Two RCs (including that of HDF-S 257 described in PaperI) show convincing evidence for a flat RC. The others show hints for a turnover velocity. All galaxies are massive with V_{max} ranging from $200 - 400$ km s^{-1}.

Table 5.5 — Masses and mass ratio's. Masses are in units of $10^{10} M_\odot$. The $24\mu m$ fluxes are in μJy and the upperlimits are 3σ. The numbers in parentheses are the values after extinction correction.

FIELD	ID	F($24\mu m$)	M_{dyn}	M_*	M_{gas}	M_{gas}/M_*	M_*/M_{dyn}	M_{bar}/M_{dyn}
MS1054	1383	202	11	$37.7^{+6.0}_{-3.3}$	12 (35)	0.3 (0.9)	3.4	4.5 (6.6)
MS1054	1714	64	—	$9.0^{+1.1}_{-0.6}$	2.4 (5.2)	0.3 (0.6)	—	—
MS1054	1719	289	30	$33.9^{+2.5}_{-0.8}$	2.6 (6.9)	0.1 (0.2)	1.1	1.2 (1.4)
MS1054	383	54	8	$9.6^{+0.1}_{-2.4}$	3.2 (4.6)	0.3 (0.5)	1.2	1.6 (1.8)
HDF-S	302	< 12	—	$3.4^{+0.1}_{-0.4}$	—	—	—	—
MS1054	1459	107	—	$29.5^{+2.1}_{-0.6}$	3.1 (5.6)	0.1 (0.2)	—	—
HDF-S	257	< 15	14	$3.0^{+0.3}_{-0.1}$	5.3 (9.4)	1.8 (2.9)	0.2	0.6 (0.9)
HDF-S	267	18	—	$4.9^{+0.5}_{-0.9}$	—	—	—	—

5.7   Masses

We calculated dynamical masses for our galaxies using

$$M_{dyn} = \frac{v^2 r}{G}. \tag{5.1}$$

where we used the flat or maximum rotation curve velocity for v and the maximum radius of the RC for r. The dynamical masses are given in Table 5.5. The reader should bear in mind that some masses have large uncertainties due to the poor sampling of the VF (MS1054 383) or are lower limits due to the limited extent of the RC (MS1054 1719).

We determined the stellar masses from SED fitting using the method described in Wuyts et al. (2007). They used a Salpeter IMF which overpredicts the number of low mass stars. A 'diet Salpeter' IMF decreases the stellar masses by 30% (Bell & de Jong 2001). For comparison, we also list the stellar mass of the galaxies for which we could not detect a VF in Table 5.5.

Gas masses can be estimated using the global Schmidt law which relates the SFR and the surface density of the gas (Kennicutt 1998). This relation has significant scatter (± 0.3 dex) but is independent of IMF if one uses the $H\alpha$ luminosity to SFR conversion factor from the same paper. There is some evidence that the global Schmidt law also holds at high redshift (Bouché et al. 2007). We used the area over which we detect $H\alpha$ to calculate the gas mass (which is significantly smaller than the total extent of the galaxy for MS1054 383 and 1719). The gas masses are also in Table 5.5.

We note that stellar mass correlates with $24\mu m$ flux (see also Table 5.5). Also, the stellar mass found in these galaxies is comparable to or larger than the dynamical mass out to the last measured point on the RC. HDF-S 257 has an exceptionally large gas-to-stellar mass ratio compared to the other galaxies of the sample, consistent with it being the youngest galaxy of the sample (according to the SED fitting, see Table 5.4). The baryonic mass of HDF-S 257 is comparable to the dynamical mass. So, for none of the galaxies there is evidence for dark matter within the observed radii.

The stellar mass of MS1054 1383 is ~ 3.4 times larger than the dynamical mass, which is of course unphysical. Adding the gas mass makes the situation even worse:

$M_{baryon}/M_{dyn} \sim 4.5$. To bring the stellar and dynamical mass in agreement, the stellar mass must be decreased and/or the dynamical mass increased.

The stellar mass could be overestimated for two reasons: the SED fitting parameters (e.g. an IMF that overpredicts the number of low mass stars (other choices for IMF result in 30% to 50% lower stellar masses) or the stellar population synthesis models (choosing the Maraston 2005 models lowers the stellar masses by a factor 1.5 for galaxies at $z \sim 2$ (Wuyts et al. 2007))) or a significant fraction of the light emitted does not have a stellar origin. However, Toft et al. (2007) do not find evidence for an AGN (from X-ray flux, shape MIR continuum, SED, absence of blue point source). The [N II]/Hα ratio is consistent with the presence of a type II AGN.

To bring the stellar and baryonic mass in agreement, the rotation velocity should double. This is about the velocity of the approaching side of the galaxy when the VF is fitted with the photometric center (~ 400 km s^{-1}). If the inclination is overestimated, the rotation velocity is underestimated. To double the inclination corrected velocity, the inclination should be $\sim 25°$ which is unlikely. Also, a rotation velocity of 400 km s^{-1} is very rare among local galaxies which makes it unlikely that an underestimate of the rotation velocity is the only reason for the discrepancy between the stellar and dynamical mass.

More plausibly, the VF as measured by Hα does not well trace the gravitational potential. Colina et al. (2005) find for a small sample of 5 low redshift ULIRGS that the velocity amplitudes of the cold molecular gas are on average twice as large as the velocity amplitudes of ionized gas. In only one case the velocity amplitudes agree and this is the only galaxy in their sample with a VF consistent with an inclined rotating disk.

The stellar mass of MS1054 1719 is the stellar mass of the entire galaxy, while the gas and dynamical mass were calculated on the inner part where we detect Hα. We checked the Ks band isophotes and calculated that $\sim 15\%$ of the Ks flux comes from the outer parts where we do not detect Hα. Decreasing the stellar mass by 15% changes the stellar-to-dynamical mass ratio to 0.96 and the baryonic-to-dynamical mass ratio to 1.05.

The baryonic-to-dynamical mass ratio of MS1054 383 is also larger than 1. In this case, the dynamical mass estimate has large uncertainty because we have no information about the VF of the approaching side of the galaxy.

5.8   Specific angular momentum and spin parameter

We calculated the specific angular momentum for the galaxies in our sample with VFs using the same method as we did for HDF-S 257 (PaperI). We used the rest frame V band effective radii determined by Trujillo et al. (2006). We note that Trujillo et al. used a photometric redshift for MS1054 1719 that results effectively in a measurement of the rest frame B band effective radius given the spectroscopic redshift. We find that MS1054 383 and 1383 are consistent with the local relation between specific angular momentum and maximum rotation velocity (see Puech et al. 2007, Navarro & Steinmetz 2000), as was HDF-S 257 (PaperI). MS1054 1719 rotates about twice as fast as expected for its specific angular momentum.
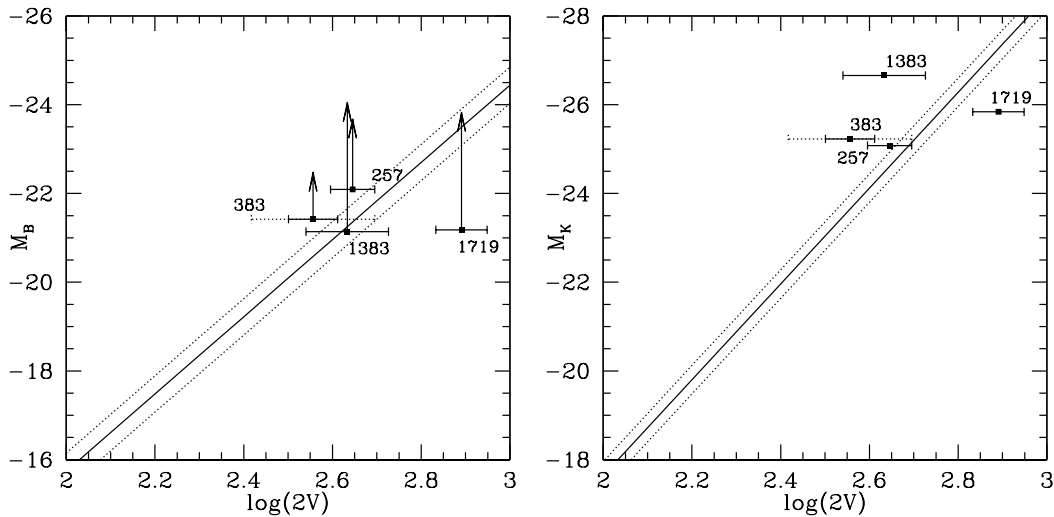
Figure 5.10 — The rest frame B and K band TFR. Local TFRs were taken from Verheijen (2001). For the B band points, the extinction correction (from Wuyts et al. 2007) is shown by the arrows. On the velocity axis is V_{flat}, or V_{max} if the RC did not flatten. The dotted velocity errorbar for MS1054 383 illustrates the uncertainty in velocity due to the uncertainty in the position of the center.

We also calculated the spin parameter λ following our approach in PaperI. We find that the spin parameters of MS1054 383 and 1383 are again consistent with those of local galaxies (as was HDF-S 257), but the spin parameter of MS1054 1719 is a order of magnitude smaller than the most probable value found by Tonini et al. (2006).

Contrary to the other three galaxies in our VF sample, MS1054 1719 is not a morphologically selected large disk. Its Sersic index is consistent with a disk galaxy (2.10, Trujillo et al. 2006), but its effective radius is smaller than those of the large disk galaxies and the center of the galaxy is bluer than the outer parts. Our results regarding the angular momentum of MS1054 1719 confirm that MS1054 1719 is morphologically and dynamically different from local disk galaxies.

5.9 Tully-Fisher relations

We will now investigate the TFR properties of our sample.

5.9.1 The rest frame B and K band TFR

The local B and K band TFR of Verheijen (2001) are shown in Fig. 5.10. We labeled our data points with their IDs for easy identification of individual sources and we added HDF-S 257 for easy comparison. For the B band TFR, we show the A_V corrections using the best fit A_V from SED fitting (Wuyts et al. 2007).

MS1054 1719 is fainter than expected for both the rest frame B and K TFR. After correcting for extinction, it is in agreement with the B band TFR. The other three galaxies are consistent with or brighter than the local B and K band TFR, with average offsets of 0.5 and 1.4 magnitudes respectively. After correcting for extinction, the average offset from the B band TFR is large: 2.3 mag.
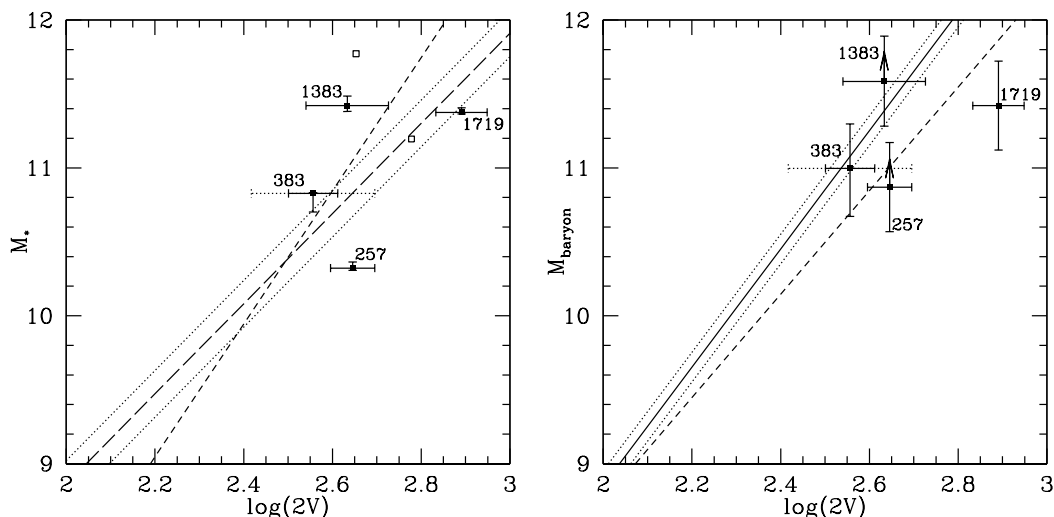
Figure 5.11 — Stellar and baryonic mass TFR. Local stellar mass TFRs were taken from Pizagno et al. (2005) and Bell & de Jong (2001) (long and short dashed line respectively). The local baryonic mass TFRs were taken from Verheijen (2001) and Bell & de Jong (2001) (full and short dashed line respectively). We corrected the stellar masses from Wuyts et al. (2007) for the different IMF used in the local comparison samples. The open symbols are the two $z \sim 2.2$ UV selected galaxies from Förster-Schreiber et al. (2006). The baryonic masses were calculated using the gas masses without correcting for extinction. The arrows in the baryonic mass TFR figure point to the location of baryonic masses with extinction corrected gas mass. We do not show the arrows for MS1054 383 and MS1054 1719 because the difference in position is smaller than the arrow.

5.9.2 The stellar and baryonic mass TFR

The relation between the stellar mass and rotation velocity, known as the stellar mass TFR, is shown in Fig. 5.11a. MS1054 1383 shows a large offset from the local relation, which is due to the unphysical stellar-to-dynamical mass ratio. MS1054 383 and 1719 are consistent with the local relation, while HDF-S 257 is lies significantly below the stellar mass TFR, consistent with its large gas content.

Förster-Schreiber et al. (2006) publish three RCs of $z \sim 2.2$ UV selected BM/BX galaxies with VFs consistent with rotating disks. Erb et al. (2006) give stellar masses for two of these sources, Q2343-BX389 and Q2343-BX610. The stellar mass estimates are similar to those of Wuyts et al. (2007). We plot these galaxies in Fig. 5.11a as well. One of them is even more offset from the local relation than MS1054 1383. Even with this additional data points, there is no clear stellar mass TFR at this redshift.

If we add the gas mass to the stellar mass, we get the baryonic mass TFR, shown in Fig. 5.11b. We assumed a factor 2 uncertainty in the gas mass. HDF-S 257 is consistent with the baryonic mass TFR due to its relatively large gas mass.

5.9.3 Comparison to other high-z samples

The most obvious comparison sample for our MIPS $24\mu m$ selected targets is our ISO selected sample at $z \sim 0.7$ (van Starkenburg et al. 2008b), as these samples were both selected using the same selection criterium (in their rest frames). Part of this sample was also observed with SINFONI, also targeting Hα and analysed using the same method.

Additional data came from the GIRAFFE IFU aiming at [O II]$\lambda3727$ and ISAAC in MR mode targeting Hα. Contrary to this sample, the $z = 0.7$ sample has a well defined rest frame K band and stellar mass TFR. Interestingly, HDF-S 257 is consistent with the stellar mass TFR of the ISO selected galaxies. Also, the apparent low K band luminosity of MS1054 1719 is consistent with the findings at $z \sim 0.7$ (see also Fig. 6b and 7 of van Starkenburg et al. 2008b).

Puech et al. (2008) present the rest frame K band for a sample of [O II] emitting galaxies at $z \sim 0.6$. They observed their sample with the multi-object integral field spectrograph of the VLT (FLAMES-GIRAFFE) which makes this a good comparison sample for our data. When they restrict their sample to rotating disks (see Flores et al. 2006 for their definition of a rotating disk), they find that the rest frame K band TFR has not evolved in scatter and possibly in slope, while the zero point has brightened by 0.66 ± 0.14 mag from $z \sim 0.6$ to the present (note: this is opposite to the trend we find). They interpret this shift as mostly luminosity evolution. Perturbed rotators and especially galaxies with complex kinematics can have large offsets from the TFR. We find for our large disk selected galaxies, including our best case HDF-S 257, the opposite trend. MS1054 1719 is consistent with the Puech et al. (2008) relation (see also Fig. 6b of van Starkenburg et al. 2008b).

Puech et al. (2008) also determine the offset from the local stellar mass TFR for their sample and find 0.36 dex smaller stellar masses, with similar scatter and slope as the local relation. This is consistent with our findings for our best case HDF-S 257.

Swinbank et al. (2006) show the rest frame B and I band TFR of their sample of six lensed $z \sim 1$ galaxies. They find 0.41 ± 0.34 mag of brightening in the rest frame B band and < 0.10 mag in rest frame I band from $z = 0$ to $z \sim 1$.

Bournaud et al. (2008) note that the derived rotation velocity of their $z = 1.6$ clump-cluster galaxy is smaller than expected from its stellar mass and the stellar mass TFR. Their hypothesis is that the clumps will evolve into the thick disk of a spiral galaxy, which does not rotate as fast as the thin disk. This is in agreement with other observations (Elmegreen & Elmegreen 2006, Bournaud et al. 2008 and references therein). However, we find for HDF-S 257 that it rotates much faster than expected from its stellar mass and the stellar mass TFR. Another difference is the fact that the VF of HDF-S 257 does not show disturbances related to the clumps. The number of galaxies with known VFs in both samples is currently too small to allow a more systematic comparison.

5.9.4 Discussion

Did we select suitable targets for TFR analysis? The general properties of the sample are good. Morphologically, three of four galaxies with measured VFs are large disk galaxies according to the criteria of Labbé et al. (2003b). The VFs of all four galaxies are consistent with rotating disks. There is strong evidence for a flattening RC in two cases, and weak evidence in two cases. The specific angular momentum and spin parameter of three galaxies are consistent with those of local galaxies. Broad line AGNs were found in none of the galaxies. There is evidence for type II AGN or shocks from the [N II]/Hα ratio in one case, while for two galaxies only lower limits to the [N II]/Hα ratios could be measured. In one case, there is strong evidence from [N II]/Hα for star

formation as the only ionizing source.

However, looking at individual properties of each galaxy, we find peculiarities for all of them. The VF of MS1054 1383 is generally consistent with a rotating disk interpretation, and so are its specific angular momentum and spin parameter. However, the VF shows distortions on small and large scales. The orientation of the VF is different from the orientation of the K band image. The double peaked area and difference between the photometric and spider center are further indications that MS1054 1383 is not a relaxed system, which was already suggested by the presence of the tidal tail in the imaging data. The stellar-to-dynamical mass ratio is much larger than unity, indicating that there is a serious problem with at least one of the mass estimates. We conclude that MS1054 1383 is not a suitable target for TFR analysis.

We were only able to derive the receding half of the VF of MS1054 383. This limits the evidence for a rotating disk interpretation. Also, the uncertainty in the dynamical center causes a large uncertainty in the derived rotation velocity. The specific angular momentum and spin parameter are consistent with those of local disk galaxies. The orientation of the VF appears to be slightly different from the orientation of the K band image. We conclude that MS1054 383 is potentially a good candidate for TFR analysis, but a longer integration time would be prefered.

The VF of MS1054 1719 is consistent with a very regular rotating disk interpretation. However, the limited extent of the RC means that the derived rotation velocity is a lower limit to the true rotation velocity. Contrary to the other galaxies of our sample, its specific angular momentum and spin parameter are different than expected from local galaxies. Also, its rotation velocity is very large. In the local universe, galaxies with similar rotation velocity are very rare. From the VF alone, this galaxy classifies as suitable for TFR analysis. We note that in other respects, this galaxy is different from local disk galaxies.

HDF-S 257 is dynamically very similar to local disk galaxies (PaperI). Its gas-to-stellar mass ratio is however much larger than observed for local galaxies. This high gas fraction does not make it unsuitable for TFR studies. Given the gas-to-stellar mass ratio, this is probably one of the youngest systems for which we can do TFR studies.

The sample of Puech et al. (2008) is sufficiently large to divide in subsamples of different dynamical classes. The interpretation of our TFR results is limited by the small sample of galaxies that all are peculiar in some way.

5.10 Conclusions

1. Galaxies selected by 24μ flux have large stellar masses and dynamical masses. Their rotation velocities range between 200 and 400 km s^{-1}. In only 1 case out of 6, we find no evidence for rotation, consistent with an inclination effect.
2. The morphologically selected large disk galaxies are dynamically also large disk galaxies.
3. Although the [N II]/Hα ratio indicates the presence of shocks or a type II AGN in $\sim 50\%$ of our targets, there is no evidence for broad line AGNs.
4. Within the observed radii (typically $\sim 1\overset{''}{.}2$ or $\sim 2r_e$), all galaxies are dominated by baryonic matter.

5. The extent of the Hα emission is a limiting factor of the VF analysis.
6. The specific angular momentum and spin parameter of morphologically selected large disks galaxies are similar to those of local spiral galaxies.
7. The $z \sim 2$ rest frame B and K band TFR are brighter than the local TFR by ~ 2.4 and 1.4 mag (after correcting for extinction).
8. Our $z \sim 2$ galaxies are consistent with the baryonic mass TFR.
9. The interpretation of these TFR results are limited by the small sample of galaxies that each are peculiar in some way.
10. Our best case for a rotating disk has a unusually high gas-to-stellar mass ratio compared to local galaxies and to other $z \sim 2$ large disk and $24\mu m$ selected galaxies.

Acknowledgements

References

Bell, E.F. & de Jong, R.S., 2001, ApJ 550 212
Bonnet, H. et al. 2004, The ESO Messenger 117, 17
Bouché, N. Cresci, G., Davies, R. et al. astro-ph 0706.2656
Bournaud, F., Elmegreen, B.G. & Elmegreen, D.M. 2007 ApJ 670 237
Bournaud, F., Daddi, E., Elmegreen, B.G. et al. 2008 A&A accepted, astro-ph 0803.3831
Brammer, G.B., van Dokkum, P. G. & Coppi, P. 2008 arXiv 0807.1533
Buchalter, A. Jimenez, R. & Kamionkowski, M. 2001 MNRAS 322 43
Colina, L., Arribas, S. & Monreal-Ibero, A. 2005 ApJ 621 725
Courteau, S., Dutton, A.A., van den Bosch, F.C. et al. 2007, ApJ 671 203
Egami, E., Rieke, G.H., Rigby, J.R. et al. 2006 in ASP Conf. Ser., The Spitzer Space Telescope, ed. L. Armus
Eisenhauer, F. et al. 2003, SPIE 4841, 1548
Elmegreen, B.G. & Elmegreen, D.M. 2006 ApJ 650 644
Elmegreen, B.G., Elmegreen, D.M. Vollbach, D.R., Foster, E.R. & Ferguson, T.E. 2005a ApJ 634 101
Elmegreen, D.M., Elmegreen, B.G, Rubin, D.S. & Schaffer, M.A. 2005b ApJ 631 85
Erb, D.K. Steidel, C.C., Shapley, A.E. et al. 2006 ApJ 646 107
Flores, H., Hammer, F., Puech, M., Amram, P. & Balkowski, C. 2006 A&A 455 107
Förster-Schreiber, N. M., Franx, M., Labbé, I. et al. 2006 AJ 131 1891
Förster-Schreiber, N. M., Genzel, R., Lehnert, M.D. et al. 2006 ApJ 645 1062
Franceschini, A., Berta. S, Rigopoulou, D. et al. 2003 A&A 403 501
Franx, M., Labbé, I., Rudnick, G. et al. 2003 ApJ 587 L79
Genzel, R., Tacconi, L.J., Eisenhauer, F. et al. 2006 Nature 442 786
Gordon, K.D., Rieke, G.H., Engelbracht, C.W. et al. 2005 PASP117 503
Heckman, T.M. 2003 Rev. Mex. AA Conf. Ser., 17 47
Kennicutt, R.C. 1998, ApJ 435 22
Knudsen, K.K., van der Werf, P., Franx, M. et al. 2005 ApJ 632 L9
Labbé, I., Franx, M., Rudnick, G. et al. 2003 AJ 125 1107
Labbé, I., Rudnick, G., Franx, M. et al. 2003 ApJ 591 L95
Labbé, I., Huang, J., Franx, M. et al. 2005 ApJ 624 81
Law, D.R., Steidel, C.C., Erb, D.K. et al. astro-ph 0707.3634
Maraston, C. 2005 MNRAS 362 799
Navarro, J.F. & Steinmetz, M. 2000 ApJ 538 477
Nesvadba, N.P.H., Lehnert, M.D., Eisenhauer, F. et al. 2006 ApJ 650 661

Nesvadba, N.P.H., Lehnert, M.D., Genzel, R. et al. 2007 ApJ 657 725

Nesvadba, N.P.H., Lehnert, M.D., Davies, R. I., Verma, A. & Eisenhauer, F. 2008 A&A 479 67

Pizagno, J., Prada, F., Weinberg, D.H. et al. 2005 ApJ 633 844

Portinari, L. & Sommer-Larsen, J. 2007, MNRAS 375 913

Puech, M., Hammer, F., Lehnert, M.D. & Flores, H. 2007 A&A 466 83

Puech, M., Flores, H, Hammer, F. et al. 2008 A&A arXiv:0803.3002

Rudnick, G., Franx, M., Rix, H-W. et al. 2001 AJ 22 2205

Rudnick, G., Rix, H-W., Franx, M. et al. 2003 ApJ 599 847

Rupke, D.S., Veilleux, S. & Sanders, D.B. 2005 ApJ 160 87

Shapiro, K.L., Genzel, Rl., Förster Schreiber, N.M. et al. 2008 ApJ in press arXiv:0802:0879

Steinmetz, M. & Navarro, J.F. 1999 ApJ 513 555

Swinbank, A.M., Smail, I., Bower, R.G. et al. 2005 MNRAS 359 401

Swinbank, A.M., Bower, R.G., Smith, G.P. et al. 2006 MNRAS 368 1631

Swinbank, A.M., Chapman, S.C., Smail, I. et al. 2006 MNRAS 371 465

Toft, S. van Dokkum, P., Franx, M. et al. 2007 ApJ 671 285

Tonini, C., Lapi, A., Shankar, F. & Salucci, P. 2006 ApJ 638 L13

Trujillo, I., Förster Schreiber, N.M., Rudnick, G. et al. 2006 ApJ 650 18

van der Hulst, J.M., Terlouw, J.P., Begeman, K., Zwitser, W. & Roelfsema, P.R. "The Groningen Image Processing System, GIPSY", in: Astronomical Data Analysis Software and Systems I, (eds. D. M. Worall, C. Biemesderfer and J. Barnes), ASP Conf. series no. 25, p. 131, 1992

van Dokkum, P.G., Franx. M., Förster-Schreiber, N.M. et al. 2004 ApJ 611 703

van Starkenburg, L., van der Werf, P.P., Yan, L. & Moorwood, A.F.M. 2006 A&A 450 25 (Chapter 2)

van Starkenburg, L., van der Werf, P.P., Franx. M et al. 2008a A&A 488 99 (PaperI) (Chapter 3)

van Starkenburg, L., et al. 2008b in prep. (Chapter 4)

Veilleux & Osterbrock 1987, ApJ 63 295

Verheijen, M. A. W., 2001, ApJ 563 694

Vogelaar, M.G.R. & Terlouw, J.P. "The Evolution of GIPSY, or the Survival of an Image Processing System", in: Astronomical Data Analysis Software and Systems X, (eds. F. R. Harnden, Jr., F. A. Primini & H. E. Payne), ASP Conf. series Vol. 238, p. 358, 2001

Wright, S.A., Larkin, J.E., Barczys, M. et al. 2007 ApJ 658 78

Wuyts, S., Labbé, I., Franx, M. et al. 2007 ApJ 655 51
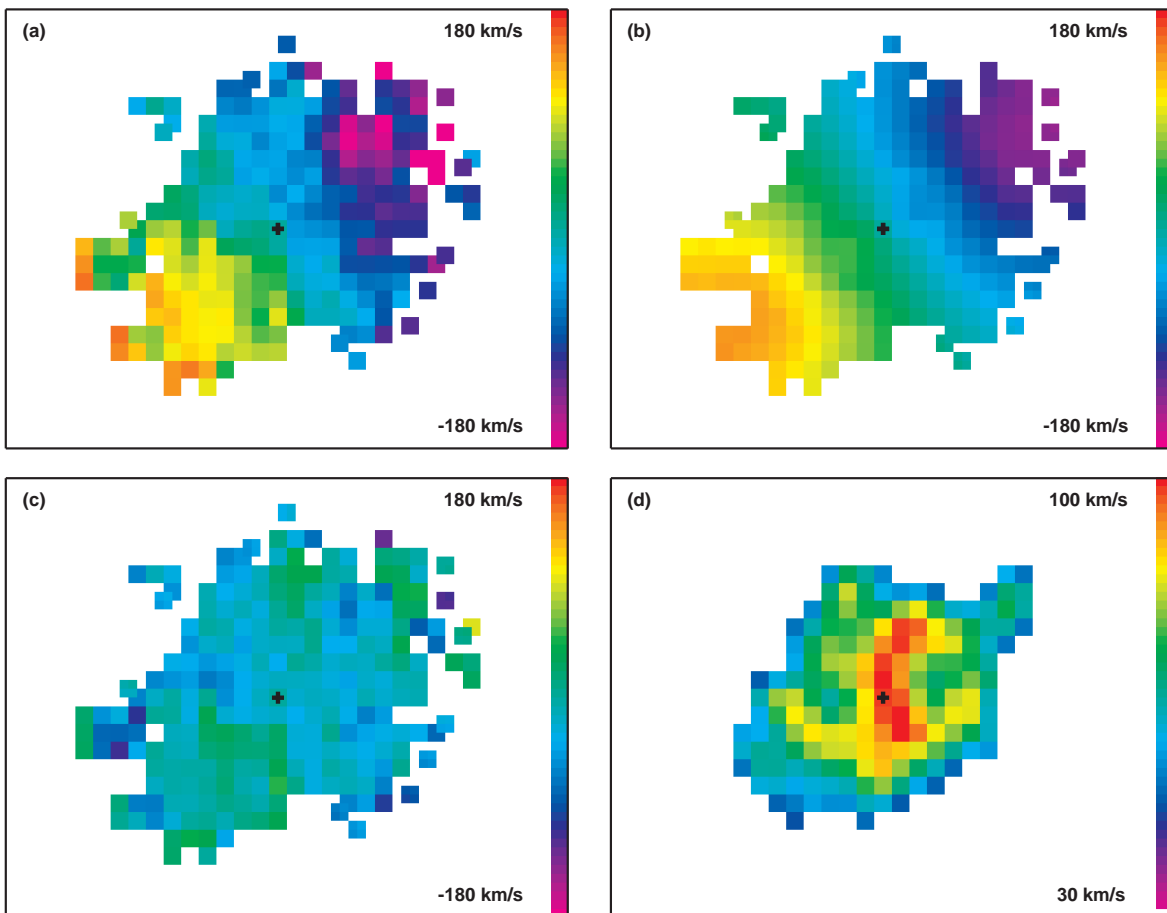
Wuyts, S., in prep.

Colour figures

Figure 3.6 — a. The observed velocity field (not corrected for inclination) for F257. Some points at the edges are the average of four pixels. b. Best fit model velocity field. c. Residuals from the fit. d. Velocity dispersion field. The extent is smaller than for the velocity field due to the lower S/N. Instrumental resolution is 32 km s^{-1}. Note that the velocity scale is different for this figure. The spatial scale and orientation is the same as in Fig. 3.1 and 3.5 and the cross point marks again the (dynamical and photometric) center.
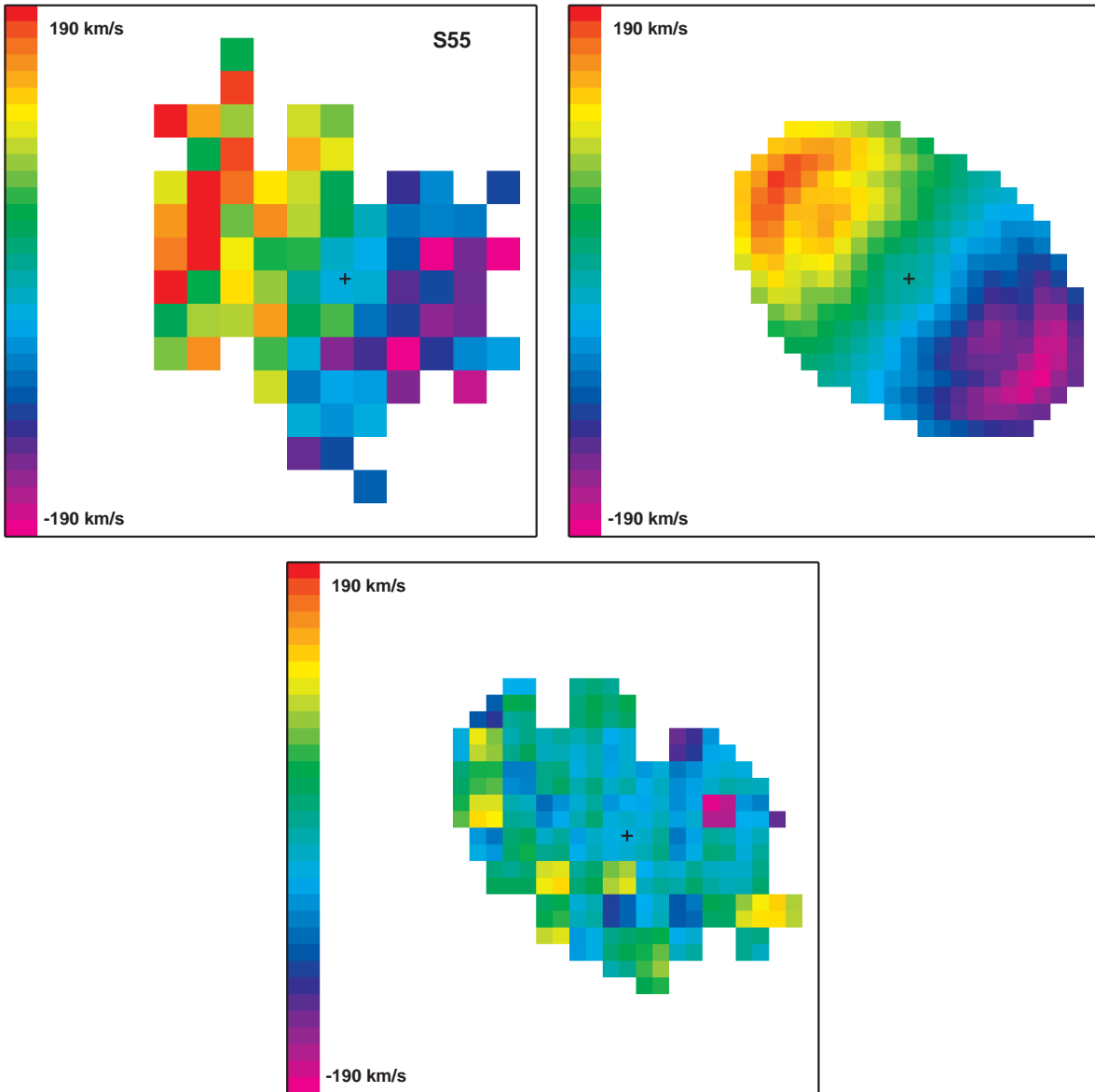
109

Figure 4.3 — The observed VF after binning to 0″.25 pixels (upper left panel), model VF (upper right panel) and the residuals from the model (bottom panel) for S55. The model VF extends to 1″.5 radius, the largest radius for which we could reliably fit the rotation velocity. The residuals are only shown for the pixels that are in the observed and model VF. Image size and orientation are the same as in Fig. 4.2a. The + point is the photometric center determined from the median collapsed SINFONI cube.
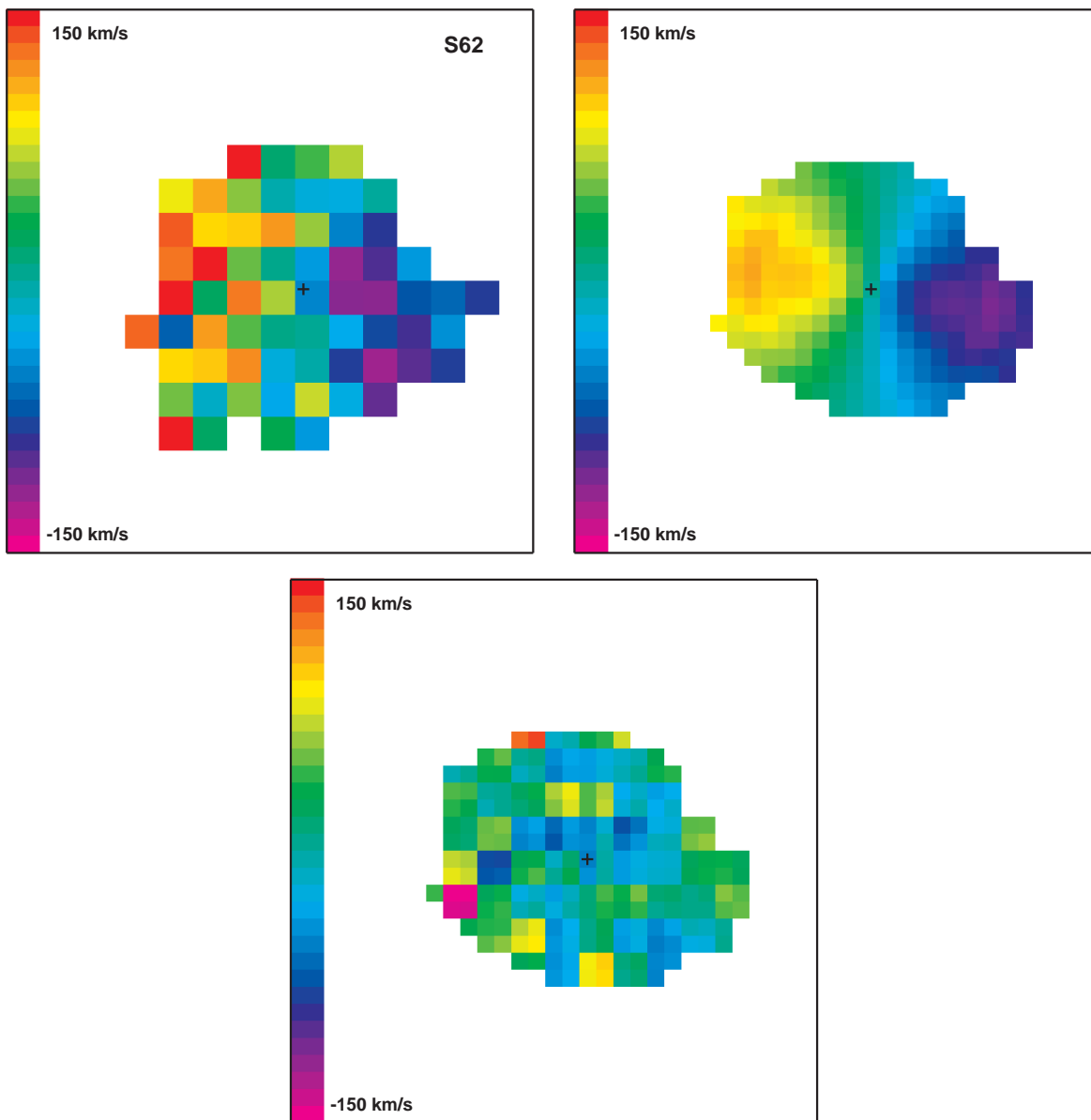
Figure 4.5 — The observed VF (upper left panel), model VF (upper right panel) and the residuals from the model (botton pabel) for S62. The model VF extends to 1."25 radius, the largest radius for which we could reliably fit the rotation velocity. The residuals are only shown for the pixels that are in the observed and model VF. Image size and orientation are the same as in Fig. 4.2b. The + point is the photometric center determined from the median collapsed SINFONI cube.
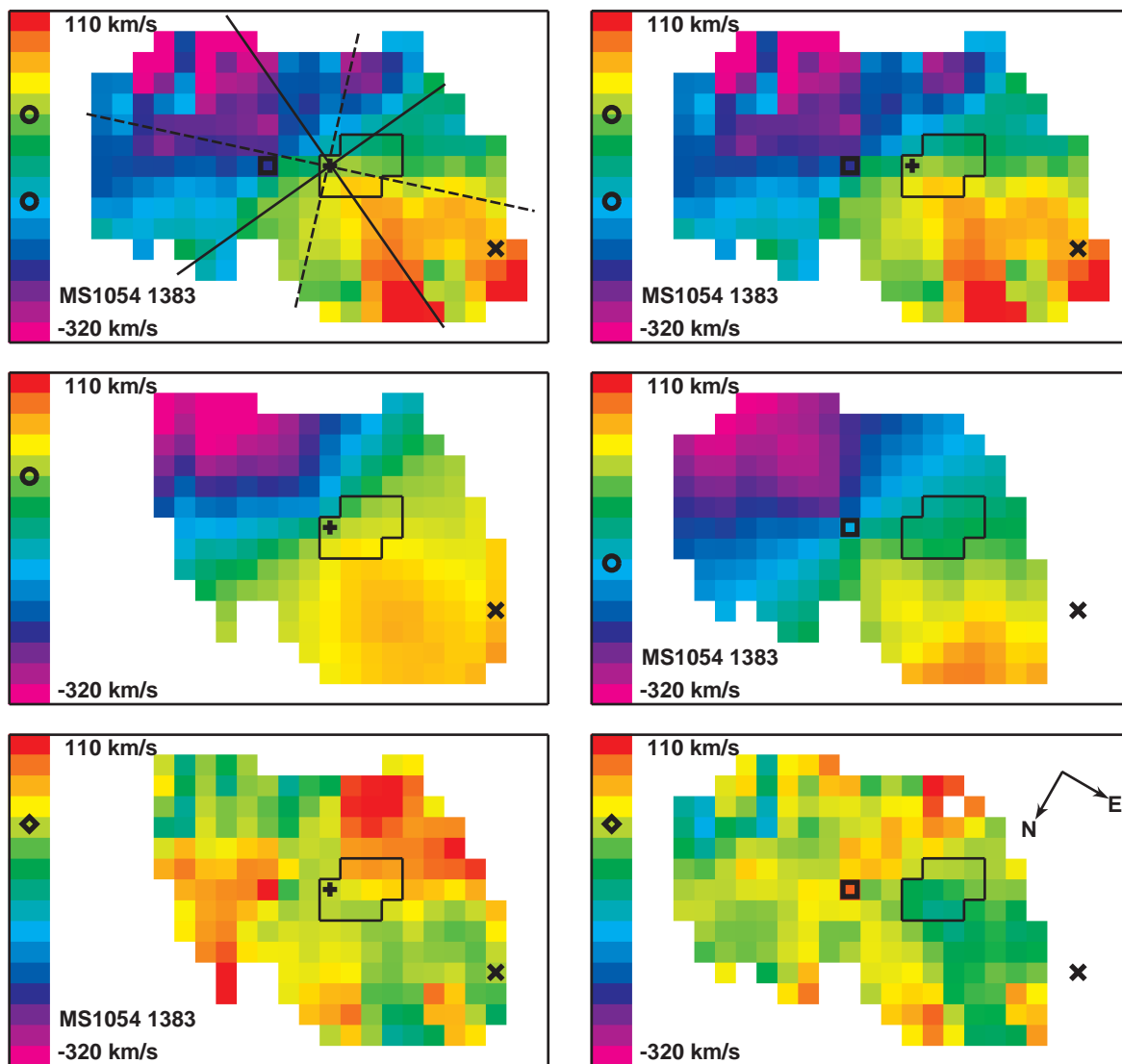
Figure 5.5 — From bottom to top: observed VF, model VF (for $r \leq 1''.25$ and showing only those pixels that are also in the observed VF) and the residuals from the model (for those pixels that are in both the observed VF and the model VF) of MS1054 1383. The left panels show the model using the photometric center, the right panels show the model with the spider centre. Image size and orientation are the same as in Fig. 5.1, except that two pixels on the left hand side have been added to show the velocity scale. The + point is again the photometric center. The best fit kinematic center is marked by the square. The best fit systemic velocity is marked with the circle. In the upper panels, the best fit systemic velocity of the photometric center and the spider center are marked. In the bottom panels, the diamond indicates where the velocity difference is zero. The X points marks the location of the J band extension. In the upper left panel, the model fit of the dynamical major and minor axis are shown as the full axes. The major and minor axis as expected from the Ks band photometry are shown as the dashed axes.
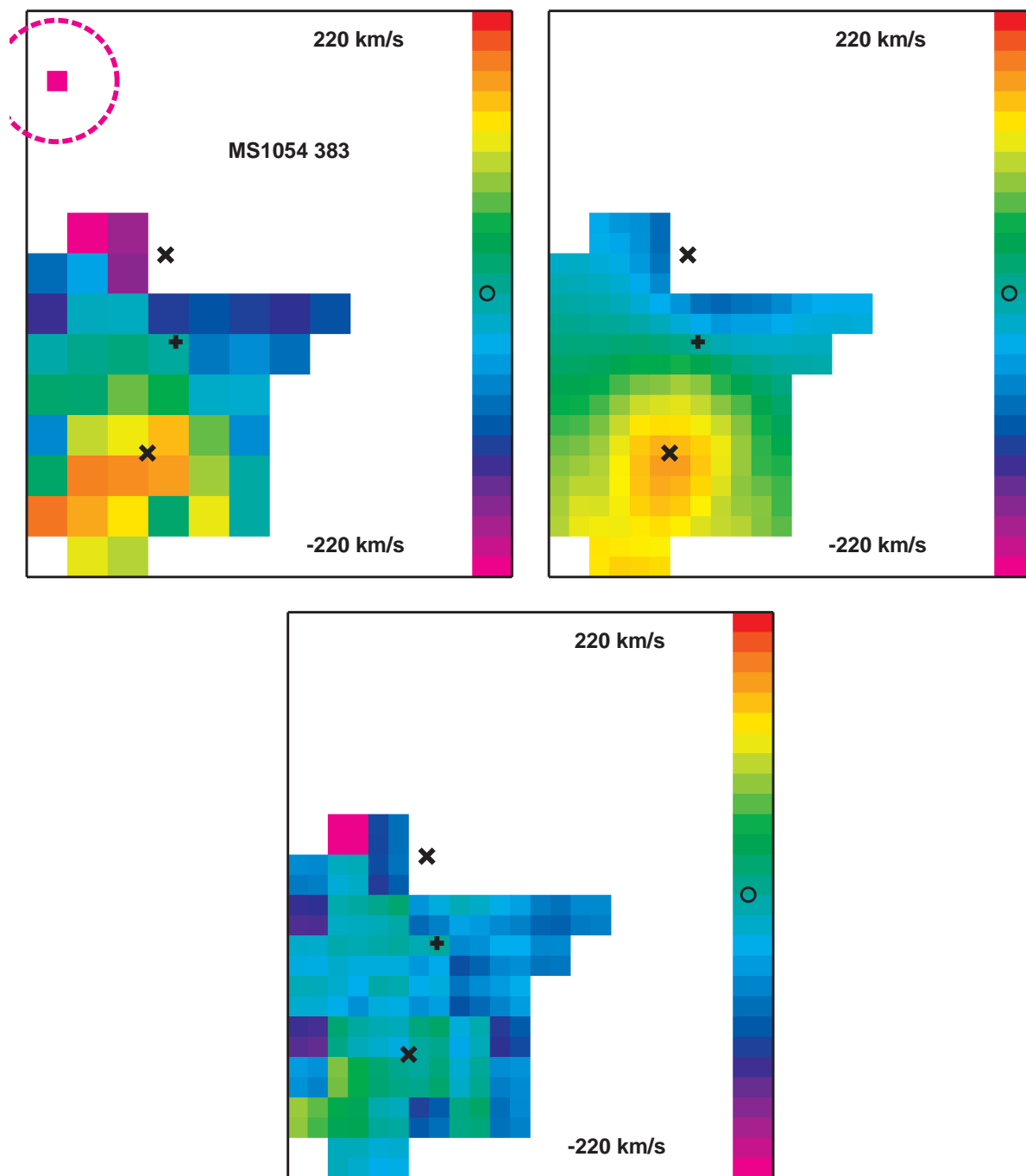
Figure 5.8 — The observed VF (upper left panel), model VF (for $r \leq 1\overset{''}{.}25$ and showing only those pixels that are also in the observed VF) (upper right panel) and the residuals from the model of MS1054 383 (bottom panel). Image size and orientation are the same as in Fig. 5.2. Symbols are as in Fig. 5.5 on the previous page. The dashes (magenta) circle indicates the area over which the velocity of the companion was measured.
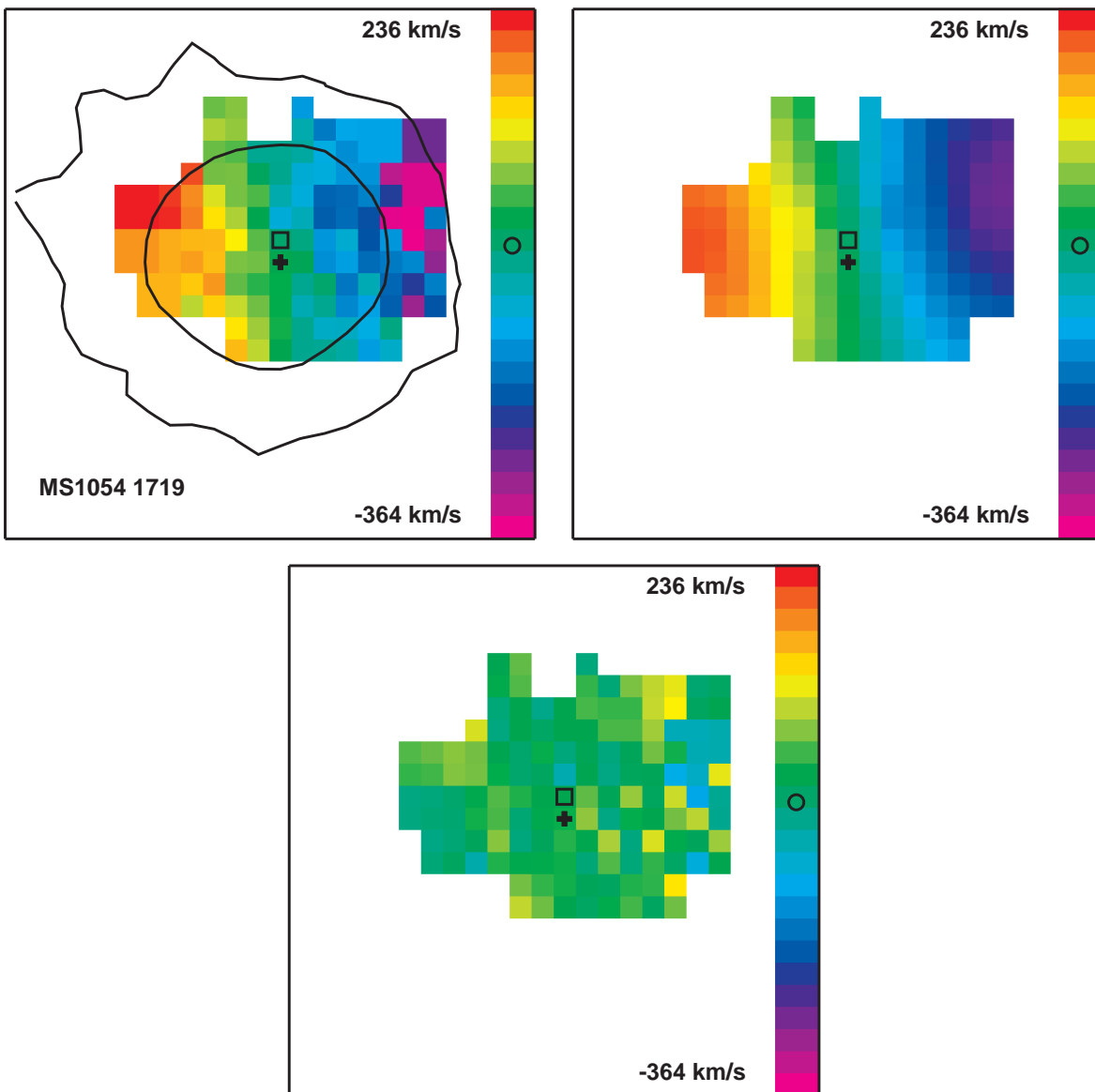
Figure 5.9 — The observed VF (upper left panel), model VF (for $r \leq 1''$ and showing only those pixels that are also in the observed VF) (upper right panel) and the residuals from the model (bottom panel) for MS1054 1719. Image size and orientation are the same as in Fig. 5.3. The symbols are as in Fig. 5.5 and 5.8 on the previous pages. Some points in the outer parts are the average of four pixels.

Nederlandse samenvatting

Spiraalstelsels

Het heelal wordt bevolkt door sterrenstelsels die elk uit miljarden sterren bestaan. Er zijn verschillende soorten sterrenstelsels. In het huidige heelal zien we vooral elliptische sterrenstelsels en spiraalstelsels. Elliptische sterrenstelsels hebben de vorm van een rugbybal of mandarijn en bestaan uit oude sterren. Spiraalstelsels bestaan uit een zogenaamde bulge van voornamelijk oude sterren in het centrum en daar omheen een dunne schijf van sterren en gas. In deze schijf worden nog steeds nieuwe sterren gevormd. Spiraalstelsels danken hun naam aan de spiraalarmen in de schijf. In Figuur 1 ziet men een voorbeeld van een spiraalstelsel. Het bekendste voorbeeld van een spiraalstelsel is onze Melkweg. Dit proefschrift gaat over spiraalstelsels.

Spiraalstelsels roteren, en wel allemaal op min of meer dezelfde manier. In de binnendelen draaien ze net zoals een CD in een CD-speler: elke ster in de schijf heeft dezelfde omlooptijd. Een ster die twee keer zo ver van het centrum ligt, heeft dus een twee keer zo grote snelheid. In de buitendelen van de schijf heeft elke ster echter dezelfde snelheid. Een ster die twee keer zo ver van het centrum ligt, doet dus dubbel zo lang over één omloop.

Spiraalstelsels draaien dan wel allemaal op ongeveer dezelfde manier, maar hun maximale snelheid varieert. Sommige hebben een maximum snelheid van minder dan 100 km s^{-1}, andere draaien sneller dan 400 km s^{-1}. De massa van spiraalstelsels bepaalt hun rotatiesnelheid. Dit kun je vergelijken met de valsnelheid van astronauten op de maan en op aarde. Astronauten op de maan dalen na een sprong langzamer dan op aarde, omdat de aarde zwaarder is dan de maan.

Rotatiekrommen en snelheidsvelden

Voor een CD geldt: alle punten op dezelfde afstand van het centrum hebben dezelfde snelheid. De rotatie-eigenschappen van een CD kunnen we dus samenvatten als een verband tussen afstand tot het centrum en snelheid. Voor spiraalstelsels geldt ook dat rotatiesnelheid alleen afhangt van afstand tot het centrum.

Het verband tussen de snelheid en afstand tot het centrum geven sterrenkundigen weer in een zogenaamde rotatiekromme. De rotatiekrommen van een CD en van een spiraalstelsel staan in Figuur 2. De rotatiekromme van een CD blijft constant stijgen. De rotatiekromme van een spiraalstelsel stijgt eerst op dezelfde manier als die van de CD, gaat dan minder snel stijgen en wordt uiteindelijk vlak. Tenminste, als de waarnemingen zich uitstrekken tot grote afstand van het centrum van het spiraalstelsel.

Aan de hemel staan geen rotatiekrommen. Met het menselijk oog kun je helemaal geen bewegingen in sterrenstelsels zien. Dit kan zelfs niet met de beste telescopen. De afstanden tot en binnen sterrenstelsels zijn zo enorm groot dat je individuele sterren
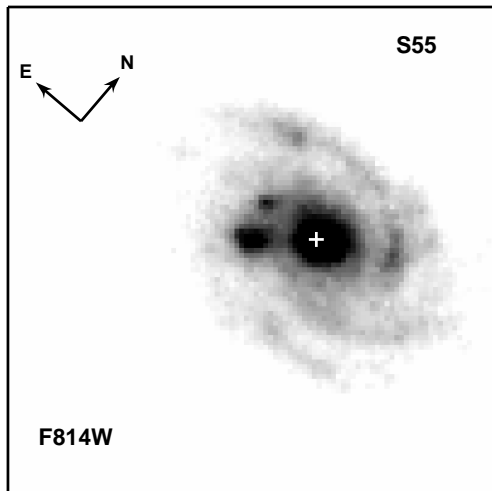
Figuur 1 — Een voorbeeld van een spiraalstelsel. Rond het centrum (aangegeven met een plusteken) is de heldere bulge zichtbaar. In de schijf zijn enkele spiraalarmen te zien. Op enkele plaatsen worden veel nieuwe sterren gevormd, dit zijn de kleine heldere gebieden verspreid over de schijf.

zich niet kunt zien verplaatsen (behalve in onze eigen Melkweg, en dan nog duurt het enkele jaren voordat de positie van sterren meetbaar veranderd is). De enige meetbare snelheid van sterren in een sterrenstelsel is de snelheid langs de gezichtslijn, dat wil zeggen: de snelheid waarmee sterren naar de waarnemer toe of van de waarnemer af bewegen. Hierbij maken we gebruik van het zogenaamde Doppler-effect: de frequentie van licht neemt toe naarmate de ster die het licht uitzond sneller naar de waarnemer toe beweegt en neemt af naarmate de ster sneller van de waarnemer af beweegt. Een vergelijkbaar effect treedt op bij geluid: het geluid van een naderende ambulance klinkt hoger dan het geluid van een zich verwijderende ambulance.

De gemeten snelheden op verschillende plaatsen van het sterrenstelsel vormen samen het waargenomen snelheidsveld. Een voorbeeld van zo'n snelheidsveld staat in Figuur 3, opnieuw voor een CD en voor een spiraalstelsel. In een snelheidsveld wordt de snelheid van elk punt weergegeven door middel van kleur: rood betekent dat het punt van de waarnemer af beweegt, groen betekent dat het punt ten opzichte van de waarnemer niet beweegt, en blauw betekent dat het punt naar de waarnemer toe beweegt.

Het waargenomen snelheidsveld is een projectie van de rotatiesnelheid op elke positie in de schijf. Door middel van een model worden de projectie-effecten opgeheven en de rotatiesnelheid op elke positie bepaald. Hieruit bepalen we dan de rotatiekromme.

De Tully-Fisher relatie

In 1977 ontdekten Tully en Fisher een nauw verband tussen de rotatiesnelheid van spiraalstelsels en hun helderheid (lichtkracht). Hoe sneller een stelsel roteert, hoe helderder het licht dat het uitstraalt. Dit verband staat nu bekend als de Tully-Fisher
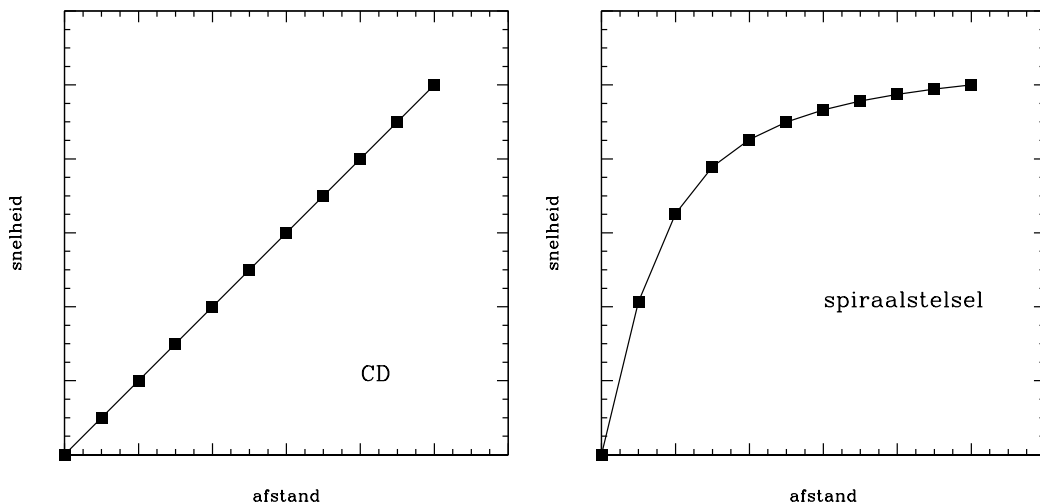
Figuur 2 — Rotatiekrommen van een CD (links) en van een spiraalstelsel (rechts).

relatie.

Daarop volgende studies vonden dat dit verband nog nauwer wordt wanneer men de spiraalstelsels bekijkt bij nabij-infrarode golflengtes (licht met een iets langere golflengte dan de kleur rood die het menselijk oog ziet). De lichtkracht bij nabij-infrarode golflengtes wordt namelijk minder beïnvloed door jonge, zeer heldere sterren en absorptie door stof.

Omdat licht wordt uitgezonden door sterren, verwacht je ook een verband tussen de hoeveelheid sterren in een spiraalstelsel (uitgedrukt in de totale massa van alle sterren samen) en de rotatiesnelheid. Deze relatie wordt de stellaire massa Tully-Fisher relatie genoemd. Deze relatie geeft aan hoe de verhouding tussen de totale massa (rotatiesnelheid!) en stellaire massa is, voor stelsels met verschillende totale massa.

De Tully-Fisher relatie is om verschillende redenen een zeer interessante relatie. In dit proefschrift gaat onze interesse uit naar de betekenis van de Tully-Fisher relatie voor het ontstaan en evolutie van sterrenstelsels. Modellen voor het ontstaan en evolutie van sterrenstelsels zijn er tot op heden niet in geslaagd om alle parameters van de Tully-Fisher relatie tegelijkertijd te verklaren.

Evolutie van spiraalstelsels

Licht reist met een enorme maar eindige snelheid door het heelal. Hoe verder een sterrenstelsel van ons verwijderd is, hoe langer het licht erover doet ons te bereiken. Door de uitdijing van het heelal ontvangen wij licht van een ver weg gelegen sterrenstelsel bij langere golflengtes ('rodere kleuren') dan het werd uitgezonden. Dit effect is groter naarmate het licht langer naar ons onderweg is geweest. Deze roodverschuiving is dus een maat voor de afstand van een sterrenstelsel. Hoe hoger de roodverschuiving, hoe langer het licht erover gedaan heeft ons te bereiken en hoe jonger het heelal was toen het licht werd uitgezonden dat wij nu zien. Door sterrenstelsels op verschillende roodverschuiving te bestuderen, kijken we terug in de tijd en kunnen we onderzoeken hoe de eigenschappen van sterrenstelsels, zoals de Tully-Fisher relatie, veranderen in
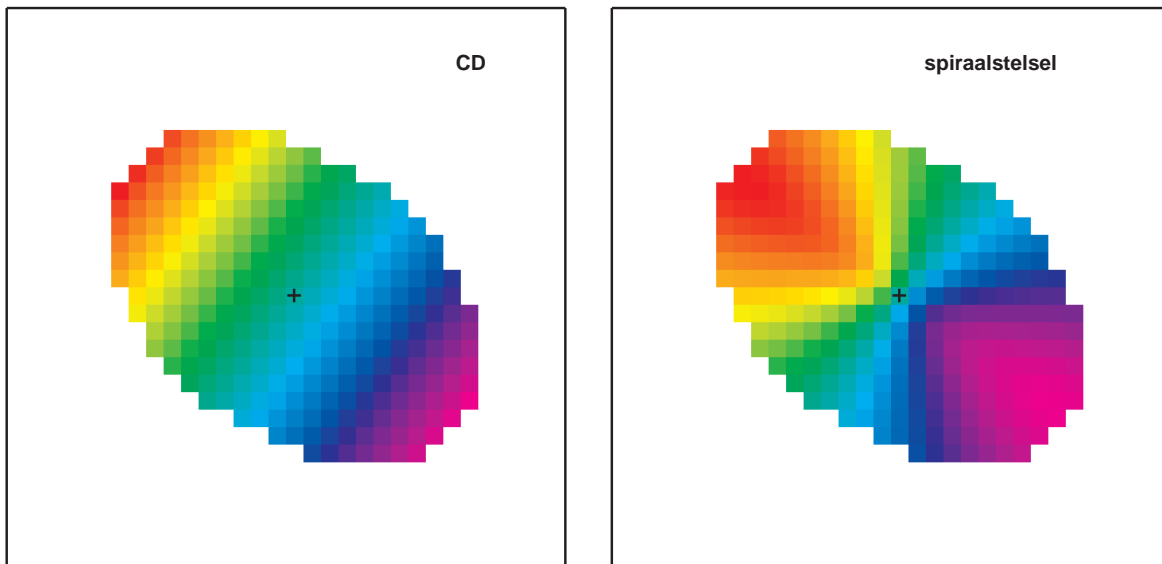
Figuur 3 — Snelheidsvelden van een CD (links) en van een spiraalstelsel (rechts). Hoe sneller een punt naar de waarnemer toe beweegt, hoe paarser de kleur. Hoe sneller een punt van de waarnemer af beweegt, hoe roder de kleur. We gebruiken deze kleuren om de verschillende snelheden voor het oog makkelijk zichtbaar te maken - ze hebben niets te maken met de werkelijke kleuren van het sterrenstelsel. De kruisjes geven het centrum van het sterrenstelsel aan.

de tijd.

Het meten van de Tully-Fisher relatie op hoge roodverschuiving is erg moeilijk. Door hun grote afstand zijn de sterrenstelsels zeer lichtzwak. Daardoor kunnen de snelheidsvelden alleen gemeten worden met de grootste telescopen en de modernste instrumenten. Zelfs dan heb je daar liefst twee tot zeven uur waarneemtijd per stelsel nodig! Ook is het pas sinds een paar jaar mogelijk om de helderheid bij nabij-infrarode golflengtes te bepalen voor grote aantallen sterrenstelsels op hoge roodverschuiving.

Het waarnemen van snelheidsvelden op hoge roodverschuiving vergt ook een andere techniek dan in het nabije heelal. Daar kunnen snelheidsvelden tot op grote afstand van het centrum van sterrenstelsels eenvoudig worden waargenomen door de snelheid van het gas te meten. Dit is (nog) niet mogelijk voor sterrenstelsels op hoge roodverschuiving. We moeten daarom gebruik maken van een andere methode, die de snelheid van het hete gas verhit door jonge sterren meet. Omdat de stellaire schijf minder groot is dan de gasschijf, kan met deze methode het snelheidsveld minder ver van het centrum gemeten worden. Hierdoor is het niet altijd mogelijk om het vlakke deel van de rotatiekromme te meten. Een ander probleem bij het waarnemen van snelheidsvelden op hoge roodverschuiving, is dat de schijnbare grootte van de sterrenstelsels aan de hemel erg klein is. Hierdoor is het aantal meetpunten veel kleiner dan in het nabije heelal en daalt de nauwkeurigheid waarmee je de rotatiekromme kunt bepalen.

Verschillende modellen voor evolutie van sterrenstelsels doen verschillende voorspellingen over de evolutie van de Tully-Fisher relatie. Evolutie in de nabij-infrarode

Tully-Fisher relatie vertelt je hoe de sterpopulaties van spiraalstelsels van verschillende massa evolueren. Evolutie in de stellaire massa Tully-Fisher relatie vertelt wanneer de sterren zijn gevormd in spiraalstelsels van verschillende totale massa.

Dit proefschrift

In dit proefschrift onderzoeken we de mogelijkheden voor het meten van Tully-Fisher relaties op hoge roodverschuiving. **Hoofdstuk 2** is daarvoor een eerste verkenning aan de hand van een aantal stelsels van het 'NICMOS grism sample' met roodverschuiving 0.8 tot 1.6 (7 tot 9 miljard jaar geleden). Dit zijn stelsels die gekenmerkt worden door relatief veel recente stervorming. De beschikbare gegevens over deze stelsels blijken te beperkt om een betrouwbare Tully-Fisher relatie te bepalen. We leren dat we voor het meten van Tully-Fisher relaties bij hoge roodverschuiving ons moeten richten op zware stelsels. Het meten van rotatiesnelheid met het licht van zeer jonge sterren heeft als nadeel dat dit alleen mogelijk is als het stelsel genoeg jonge sterren heeft. Te veel van deze sterren is echter ook niet goed: hun licht domineert dan de totale helderheid van het stelsel. Dit bemoeilijkt de vergelijking tussen stelsels met sterpopulaties van verschillende leeftijden.

In **Hoofdstuk 3** bestuderen we een sterrenstelsel op roodverschuiving 2.03 (dit licht is 10 miljard jaar naar ons onderweg geweest). Het uiterlijk en de grootte van dit stelsels lijken zeer op die van nabije spiraalstelsels. De leeftijd van de sterpopulatie van dit sterrenstelsel is echter geschat op ongeveer 160 miljoen jaar - voor sterrenstelsels is dit zeer jong. We hebben het snelheidsveld van dit sterrenstelsel waargenomen en hieruit de rotatiekromme afgeleid. Het snelheidsveld is zeer regelmatig en lijkt op die van nabije spiraalstelsels. Ook de rotatiekromme lijkt zeer op de rotatiekrommen van nabije spiraalstelsels: een snelle stijging in het binnenste deel en verder van het centrum vlak (zie Figuur 3.7 in Hoofdstuk 3). Dit stelsel is wellicht het beste voorbeeld van een roterend schijfstelsel dat bekend is op deze roodverschuiving. We hebben dit stelsel vergeleken met de nabij-infrarode Tully-Fisher relatie en de stellaire massa Tully-Fisher relatie. Vergeleken met sterrenstelsels met dezelfde rotatiesnelheid in het nabije heelal, heeft dit stelsel dezelfde helderheid bij nabij-infrarode golflengtes. De stellaire massa is in vergelijking iets kleiner, maar we kunnen het verschil niet nauwkeurig genoeg bepalen om dit met zekerheid te kunnen zeggen.

Vervolgens hebben we geprobeerd om de Tully-Fisher relatie te bepalen van zware sterrenstelsels op hoge roodverschuiving. We hebben gekozen voor zware stelsels vanwege de redenen beschreven in Hoofdstuk 2. Om geen waarneemtijd te verspillen moesten we vóórdat we gingen waarnemen een manier vinden om zware stelsels uit te kiezen. Uit eerder onderzoek was gebleken dat stelsels op roodverschuiving ~ 0.7 (6 miljard jaar geleden) die helder infrarood licht (golflengte 15 micrometer) uitzenden zware stelsels zijn. Uiterlijk lijken deze stelsels ook op nabije spiraalstelsels. Sommige vertonen ook spiraalstructuur. Eén van de stelsels is het stelsel afgebeeld in Figuur 1. We hebben drie van deze sterrenstelsels waargenomen en de resultaten van dit werk staan beschreven in **Hoofdstuk 4**.

De waarnemingen waren succesvol voor twee van de drie stelsels. De stelsels blijken inderdaad met hoge snelheid te roteren. Twee andere groepen onderzoekers heb-

ben ook van dit soort stelsels waargenomen. Voor het bepalen van de Tully-Fisher relatie van heldere 15 micrometer stelsels op roodverschuiving ~ 0.7 hebben we de resultaten van hun waarnemingen ook gebruikt. Het blijkt dat zowel de nabij-infrarode als de stellaire massa Tully-Fisher relatie 6 miljard jaar geleden inderdaad al bestonden, zoals we ook verwachtten op grond van andere onderzoeken. Vergeleken met de nabije nabij-infrarode Tully-Fisher relatie zijn deze stelsels iets minder helder bij dezelfde rotatiesnelheid, maar het verschil is niet significant. De stellaire massa Tully-Fisher relatie bestudeerden we met twee verschillende meetmethoden voor de stellaire massa. Voor beide methodes vinden we inderdaad een stellaire massa Tully-Fisher relatie. Vergeleken met spiraalstelsels in het nabije heelal hebben de 15 micrometer stelsels een kleinere stellaire massa bij dezelfde rotatiesnelheid. Echter, hoe groot het verschil is hangt af van de manier waarop de stellaire massa is bepaald. We vermoeden dat dit komt omdat het ene model meer ruimte laat voor een populatie van oude sterren, die weinig licht uitstralen maar wel een grote bijdrage doen aan de totale stellaire massa. We zullen dus meer inzicht moeten krijgen in de beste manier voor het bepalen van de stellaire massa's om precies te kunnen vaststellen hoeveel de stellaire massa Tully-Fisher evolueert. De verkregen Tully-Fisher relatie laat zien dat onze selectiemethode geschikt is voor dit type onderzoek.

Tenslotte richten we ons in **Hoofdstuk 5** op zware sterrenstelsels op roodverschuiving 2 (10 miljard jaar geleden). We selecteren nu stelsels die helder zijn bij licht met een golflengte van 24 micrometer. Dit komt neer op hetzelfde selectiecriterium als voor de sterrenstelsels van Hoofdstuk 4. Daarnaast hebben we nog enkele stelsels waargenomen die voldoen aan hetzelfde selectiecriterium als het stelsel van Hoofdstuk 3. In totaal hebben we acht stelsels kunnen waarnemen. Voor drie daarvan (plus het stelsel van Hoofdstuk 3) hebben we snelheidsvelden kunnen bepalen. Daarnaast hebben we nog gegevens van twee (op andere wijze geselecteerde) stelsels gebruikt die op dezelfde roodverschuiving staan en door andere onderzoekers zijn waargenomen.

In tegenstelling tot roodverschuiving 0.7, vinden we voor roodverschuiving 2 ook snelheidsvelden die erop wijzen dat de sterren zich niet in cirkelbanen om het centrum bewegen. Voor twee stelsels kunnen we het snelheidsveld voor een gedeelte van het stelsel niet bepalen omdat in die gedeeltes te weinig nieuwe sterren worden gevormd. We vinden ook geen duidelijke Tully-Fisher relaties. Dit laatste kan komen door de afwijkende snelheidsvelden en door het kleine aantal waargenomen stelsels. Het lijkt er dus op dat de Tully-Fisher relatie op roodverschuiving 2 nog niet bestaat, maar om daar zekerheid over te krijgen zijn goede waarnemingen van meer stelsels nodig.

Curriculum vitae

Volgens mijn moeder waren mijn eerste twee zinnetjes "Isse dat?" en "ikke zelluf doen". Gelukkig beschikte ze over engelengeduld. En gelukkig was ik haar eerste kind. Ze heeft jaren gedacht dat ze een normaal kind had gekregen, ook toen ik haar begon te wijzen op opmerkelijke fysische verschijnselen: "Weet je wat ik zo raar vind? Gek hè?! Ik heb zulke kleine ogen, maar ik kan zó véél zien!"

Op vijftienjarige leeftijd nam ik de touwtjes om verder te leren zelf in handen en vroeg de decaan van mijn middelbare school of ik examen mocht doen in tien vakken, en wel op mijn manier: voor elk vak de helft van de lesuren, en de rest zou ik zelf thuis doen. Ik kreeg toestemming en ruim twee jaar later slaagde ik met succes. Maar belangrijker was dat ik had geleerd om op tijd om hulp te vragen en dat ik eindelijk eens heel hard had kunnen werken. Dit gaf me energie en ruimte voor andere dingen.

Na de middelbare school ging ik in Leiden studeren, het eerste jaar natuurkunde, daarna sterrenkunde. Na drie jaar begon ik aan mijn klein onderzoek over fotometrische roodverschuivingen onder begeleiding van Dr. Paul van der Werf. Mijn groot onderzoek, onder begeleiding van Prof. Dr. Marijn Franx, ging over zwakke gravitationele lensing tussen sterrenstelsels. Na zes jaar studeerde ik in 2002 cum laude af.

Achter dit prachtige resultaat schuilt nog een ander verhaal. Na eerst getobd te hebben met de gevolgen van een verkeersongeval, werd ik in mijn vierde studiejaar ernstig ziek. Uiteindelijk stelde ik zelf de juiste diagnose, en vond ik zelf de juiste medicijnen in de juiste dosis. Naar aanleiding van deze eigen zoektocht naar overleven en kwaliteit van leven was ik mede-initiatiefnemer van belangengroep Hypo maar niet Happy voor mensen met hypothyreoïdie.

Na mijn afstuderen begon ik aan mijn promotieonderzoek, opnieuw onder begeleiding van Dr. Paul van der Werf. Ik bezocht conferenties in binnen- en buitenland, en reisde twee keer naar Chili om waarnemingen te doen met SINFONI op de Very Large Telescope op Cerro Paranal. Ik waande me daar een Mars-reiziger, zo ver het oog reikt stenen, stenen en stenen.

Naast mijn werk op de Sterrewacht bleef ik actief als bestuurslid met portefeuille wetenschappelijk onderzoek en belangenbehartiging van inmiddels belangenvereniging Hypo maar niet Happy voor mensen met hypothyreoïdie. Mijn werkzaamheden waren zeer divers, zo bezocht ik symposia, was ik lid van Commissie Richtlijnontwikkeling Samenwerkende Schildklierpatiëntenorganisaties en schreef ik veel voorlichtingsmateriaal.

Kort na mijn tweede reis naar Chili raakte ik zwanger en op 1 februari 2007 werd Karmijn geboren. Anderhalf jaar en twee weken later voltooi ik mijn 'tweede kindje', dit proefschrift.

Per oktober 2008 begin ik bij Achmea Zorg als informatieanalist.

Nawoord

Aanvankelijk als student, daarna als aio heb ik negen jaar met veel plezier op de Sterrewacht gewerkt. Plezier in je werk ontstaat voor een belangrijk deel door je collega's. Ook voor praktische zaken rond het maken van een proefschrift vervullen zij een prominente rol. In het bijzonder ben ik dank verschuldigd aan Stijn, Dominic, Arjen, Pedro en Davor.

Een functionerende computer is onmisbaar voor dit werk, en ik ben David, Erik, Aart en Tycho zeer dankbaar voor hun hulp, inzet en geduld. Ook de dames van het secretariaat wil ik bedanken voor een praktische raad en daad, en Jeanne ook voor het zelfgebreide vestje.

Daarnaast wil ik alle vrijwilligers en bestuursleden van HmnH bedanken voor hun betrokkenheid, inzet en chocolaatjes bij vergaderingen. Het werk voor HmnH vormde een geweldig tegenwicht voor mijn werkzaamheden op de Sterrewacht. Ik mis jullie!

Mijn leven, welzijn en kind dank ik aan alle mensen die de moeite namen om hun verhaal en hun kennis te delen op internet. Dit proefschrift is tot stand gekomen dankzij 0.04 gram liothyronine. Ik hoop er nog zeker 0.25 gram aan toe te voegen.

Jolijn, bedankt voor het maken van het prachtige omslag!

Ik besloot dat ik alles kon - ik ben het niet vergeten, Arjen! Ik geloof dat ik weer dringend toe ben aan witte chocola met noten...

Tien, dank voor de verfrissende perspectieven vanuit Wageningen. We hebben ons meer dan eens verbaasd over de merkwaardige parallellen in onze levens. Ik hoop dat Die Ene er snel aan toegevoegd wordt!

Als werkende ouder is het heerlijk als de deur door je kind achter je dicht gesméten wordt omdat Oma er is. Mam, en pap, heel erg bedankt voor jullie goede zorgen voor ons allemaal.

Paul, K+K voor jou. Je was het op één na beste besluit van mijn leven. Karmijn, jij was het beste!